MONTAN
UNIVERSITÄT
LEOBEN

Chair of Design of Steels

Doctoral Thesis

Resistance Spot Welding of Third Generation Advanced High Strength Steels

Dipl.-Ing. Manfred Stadler, BSc

June 2021

MONTANUNIVERSITÄT LEOBEN
www.unileoben.ac.at

AFFIDAVIT

I declare on oath that I wrote this thesis independently, did not use other than the specified sources and aids, and did not otherwise use any unauthorized aids.

I declare that I have read, understood, and complied with the guidelines of the senate of the Montanuniversität Leoben for "Good Scientific Practice".

Furthermore, I declare that the electronic and printed version of the submitted thesis are identical, both, formally and with regard to content.

Date 01.06.2021

Signature Author
Manfred Stadler

Danksagung

An dieser Stelle möchte ich mich bei allen bedanken, die mich während der letzten drei Jahre begleitet haben!

In erster Linie möchte ich mich natürlich bei Herrn Prof. Dr. Ronald Schnitzer bedanken, der mir die Verfassung dieser Dissertation ermöglicht hat und fachlich wie auch menschlich ein toller Chef war. Mein Dank gilt auch Frau Dr. Christina Hofer, die mich während der Dissertation hervorragend betreute und mir mit Rat und Tat zur Seite stand.

Bedanken möchte ich mich ebenfalls bei den Mitarbeitern von voestalpine Stahl Linz besonders bei Sabine Ritsche, Martin Gruber, Katharina Steineder, Franz Perndorfer und Robert Sierlinger für die tolle und unkomplizierte Zusammenarbeit. Es war mir stets eine Freude euch in Linz besuchen zu dürfen und ich hoffe, dass sich unsere Wege eines Tages noch einmal kreuzen!

Meinen langjährigen Freunden vom SSSST: Ante, Bobo, Dorno, Dumi, Geri, Grüni, Hittn und Stöze danke ich für die oft mühsamen, aber trotzdem sehr sauberen zweiten Dienstage des Monats.

Meinen Büroboyz Jan Platl, Michael Göbl, Johann Kappacher und Max Siller gilt mein ganz besonderer Dank! Wir waren die letzten drei Jahre mehr als nur Bürokollegen und ich danke euch von ganzem Herzen für eure Freundschaft. Ein solches Arbeitsklima kann man sich nur wünschen und ich hoffe wirklich, dass wir uns nicht aus den Augen verlieren!

Meiner Freundin Sylvia danke ich für ihre tolle Unterstützung in den letzten eineinhalb Jahren. Du hast mich nach Rückschlägen stets wieder aufgemuntert und ich bin wirklich unendlich glücklich, dich in meinem Leben zu haben.

Wie schon bei der Masterarbeit gilt der größte Dank erneut meiner Mutter. Ohne dein Vertrauen und deine moralische wie auch großzügige finanzielle Unterstützung hätte ich weder den Weg eines technischen Studiums noch den des Doktorats eingeschlagen! Tausend Dank dafür!!!

Table of contents

Part A

List of abbrevations……………………………………………………………………………………………I

Abstract……..III

Kurzfassung…………………………………………………………………………………………………….IV

1. Introduction……………………………………………………………………………………………………1

2. State of the art………………………………………………………………………………………………..3

2.1. Advanced high strength steels (AHSS) for automotive applications………………………….3

2.2. Third generation advanced high strength steels…………………………………………………..4

2.2.1. TRIP-aided bainitic ferrite (TBF) steels……………………………………………………5

2.2.2. Medium-Mn steels…………………………………………………………………………………6

2.3. Resistance spot welding (RSW)……………………………………………………………………….7

2.3.1. Process and physical background……………………………………………………………7

2.3.2. Welding parameters……………………………………………………………………………….8

2.3.3. Mechanical testing: the cross-tension strength (CTS) test…………………………..9

2.4. Resistance spot welding of AHSS: challenges and solutions…………………………………11

2.4.1. The fusion zone (FZ)……………………………………………………………………………..11

2.4.2. The heat-affected zone (HAZ)………………………………………………………………..12

2.4.3. In-process heat treatments……………………………………………………………………..13

2.5. Relation of the current thesis to the state of the art………………………………………………16

3. Summary of publications……………………………………………………………………………………….17

3.1. Appended Papers……………………………………………………………………………………………….17

3.2. Conference contributions……………………………………………………………………………………..18

3.3. Supervised theses………………………………………………………………………………………………18

3.4. Summary of published contents………………………………………………………………………...18

3.4.1. Aim and scope of the investigations………………………………………………………18

3.4.2. Influence of a temper pulse on the microstructure of the FZ and HAZ……….19

3.4.3. Correlation between the microstructure and mechanical properties of temper pulse and recrystallization pulse welds…………………………………………………22

3.4.4. Influence of the cooling time between the first pulse and the recrystallization pulse………………………………………………………………………………….25

3.4.5. Microstructure and local mechanical properties of the HAZ of the medium-Mn steel……………………………………………………………………………………….28

4. Outlook and open questions……………………………………………………………………………….34

5. Novel features………………………………………………………………………………………………….36

6. References……………………………………………………………………………………………………….37

Part B

Paper I M. Stadler, M. Gruber, R. Schnitzer, C. Hofer

Microstructural characterization of a double pulse resistance spot welded 1200 MPa TBF steel

Welding in the World 64 (2020) 335-343

Paper II M. Stadler, R. Schnitzer, M. Gruber, C. Hofer

Improving the mechanical performance of a resistance spot welded 1200 MPa TBF steel

International Journal of Materials Research 112 (2021) 262-270

Paper III M. Stadler, R. Schnitzer, M. Gruber, K. Steineder, C. Hofer

Influence of the cooling time on the microstructural evolution and mechanical performance of a double pulse resistance spot welded medium-Mn steel

Metals 11 (2021) 270

Paper IV M. Stadler, R. Schnitzer, M. Gruber, K. Steineder, C. Hofer

Microstructure and local mechanical properties of the heat-affected zone of a resistance spot welded medium-Mn steel

Materials 14 (2021) 3362

Part A

List of abbrevations

AHSS	Advanced high strength steels
BM	Base material
BSE	Backscattered electrons
Ceq	Carbon equivalent number
CGHAZ	Coarse grained heat-affected zone
CI	Confidence Index
CTS	Cross-tension strength
DP	Dual phase
EBSD	Electron backscatter diffraction
EDX	Energy dispersive X-ray diffraction
EPMA	Electron probe microanalyzer
FE	Finite element
FGHAZ	Fine grained heat-affected zone
FZ	Fusion zone
HAZ	Heat-affected zone
ICHAZ	Intercritical heat-affected zone
IF	Interfacial failure
IPF	Inverse pole figure
LOM	Light optical microscopy
M_f	Martensite finish
M_s	Martensite start
PAGs	Prior austenite grains
PF	Pullout failure
PHS	Press hardening steels

PIF	Partial interfacial failure
Q&P	Quenching & Partitioning
SCHAZ	Subcritical heat-affected zone
SE	Secondary electrons
SEM	Scanning electron microscopy
TBF	TRIP-aided bainitic ferrite
TE	Total elongation
TRIP	Transformation-induced plasticity
TS	Tensile strength
TSS	Tensile shear strength
TWIP	Twinning-induced plasticity
UTS	Ultimate tensile strength
UCHAZ	Upper critical heat-affected zone
YS	Yield strength

Abstract

Third generation advanced high strength steels (AHSS), such as transformation-induced plasticity (TRIP)-aided bainitic ferrite (TBF) and medium-Mn steels, combine high strength with good formability and are therefore promising candidates for the use for automotive applications. However, due to their relatively high alloying content and the rapid cooling during resistance spot welding, which is the predominant joining technology for automotive steel sheets, they tend to form hard and brittle joints and their weldability is therefore restricted.

The present work aims to enable basic knowledge concerning the microstructural evolution during resistance spot welding of third generation AHSS in order to subsequently improve their mechanical performance by means of a targeted modification of the microstructure. For the TBF steel, large-scale hardness mappings revealed a pronounced hardening and thus embrittlement of the fusion zone (FZ), which was counteracted with a temper pulse. Microstructural characterizations by means of light optical microscopy and scanning electron microscopy (SEM) illustrated that the temper pulse must be adjusted precisely to the first pulse in order to get acceptable results. In a second approach, the cast-like structure of the outer FZ was modified by a recrystallization pulse in order to obtain more globularly shaped prior austenite grains with a high crack deflection capability, which were characterized using electron backscatter diffraction (EBSD). With both concepts a significant improvement of the mechanical performance could be achieved.

The inferior mechanical properties of medium-Mn steel welds were mainly attributed to the presence of severe manganese segregations in the outer FZ, as detected by energy-dispersive X-ray spectroscopy (EDX). The segregations were homogenized by means of a recrystallization pulse, which led to an improved mechanical performance of the welds. An approach to estimate suitable cooling times between the two pulses based on the electrical resistance curve was suggested in order to facilitate the implementation of double pulsing in production. The detailed characterization of the heat-affected zone (HAZ) by means of EBSD, SEM, EDX and magnetic saturation measurement showed that the stability of the austenite strongly depends on the temperature, resulting in highly position-dependent mechanical properties of the HAZ. These findings serve as basis for future efforts to precisely adjust the microstructure of the HAZ in order to improve the mechanical performance of the entire weld.

Kurzfassung

„Advanced High Strength Steels“ (AHSS) der dritten Generation, wie „Transformation-Induced Plasticity (TRIP)-aided Bainitic Ferrite“ (TBF) und „Medium-Mn“ Stähle, kombinieren hohe Festigkeit mit guter Umformbarkeit und sind daher vielversprechende Kandidaten für den Einsatz in automobilen Anwendungen. Aufgrund ihres relativ hohen Legierungsgehalts und der raschen Abkühlung beim Widerstandspunktschweißen, welches das dominierende Blechfügeverfahren darstellt, neigen diese Stähle allerdings zur Bildung harter und somit spröder Schweißverbindungen, weswegen ihre Schweißbarkeit eingeschränkt ist.

Diese Arbeit soll ein grundlegendes Verständnis bezüglich der Mikrostrukturentwicklung während des Widerstandspunktschweißens von AHSS der dritten Generation aufbauen, um die mechanischen Eigenschaften anschließend mittels gezielter Gefügebeeinflussung verbessern zu können. Durch großflächige Härtemappings wurde beim TBF Stahl eine ausgeprägte Aufhärtung und somit Versprödung der Fügezone (FZ) festgestellt, welcher mit Hilfe eines Anlassimpulses entgegengewirkt wurde. Die Gefügeuntersuchungen mittels Lichtmikroskopie und Rasterelektronenmikroskopie (REM) zeigten, dass der Anlassimpuls exakt auf den ersten Impuls abgestimmt werden muss. In einem weiteren Ansatz wurde das gussähnliche Gefüge der äußeren FZ durch einen Rekristallisationsimpuls modifiziert, um globulare Körner mit hohem Rissablenkungsvermögen zu erzeugen, welche mittels „Electron Backscatter Diffraction“ (EBSD) charakterisiert wurden. Mit beiden Konzepten konnten die mechanischen Eigenschaften deutlich verbessert werden.

Bei Medium-Mn Stählen wurden starke Manganseigerungen in der äußeren FZ mittels energiedispersiver Röntgenspektroskopie (EDX) nachgewiesen, welche durch einen Rekristallisationsimpuls hin zu verbesserten mechanischen Eigenschaften aufgelöst wurden. Die präsentierte Interpretation der aufgezeichneten Widerstandskurven soll hierbei die angestrebte Implementierung des Rekristallisationsimpulsverfahrens in die Fertigung unterstützen. Die detaillierte Charakterisierung der Wärmeeinflusszone (WEZ) mittels EBSD, REM, EDX und magnetischer Austenitmessung zeigte, dass die Stabilität des Austenits stark von der Temperatur abhängt, was zu ortsabhängigen mechanischen Eigenschaften der WEZ führt. Diese Erkenntnisse dienen als Basis für zukünftige Bemühungen die Mikrostruktur der WEZ gezielt einzustellen um die mechanischen Eigenschaften der gesamten Schweißung zu verbessern.

1. Introduction

The commitment of the European Commission to the green new deal and the related goal of making Europe climate neutral in 2050 is also increasing the demands on the automotive industry regarding the reduction of fuel consumption and exhaust emissions [1,2]. Regardless of which concept of drive will prevail, lightweight construction using innovative materials will play a decisive role in achieving these goals [3]. Due to their unmatched combination of high strength and good formability, advanced high strength steels (AHSS) are widely used for safety-relevant components in the body-in-white of modern cars [4]. The focus of today's steel industry lies on the development and establishment of the third generation of these high-performance materials, which combines high strength with superior elongation, due to a certain amount of metastable austenite in the microstructure, which enables the so-called transformation-induced plasticity (TRIP) effect [5]. The third generation of AHSS consists of the quenching and partitioning (Q&P) [6] and TRIP-aided bainitic ferrite (TBF) steels [7], with a martensitic or bainitic matrix, respectively, as well as the medium-Mn steels [8] with a ferritic matrix.

Regardless of superior mechanical properties, workability is a key factor regarding the establishment of a material for automotive applications. Despite the continuous development of novel joining methods, resistance spot welding (RSW) is still the dominant joining technology for sheet steels, due to its short cycle times, its low costs and its suitability for automation [9]. However, the relatively high content of alloying elements in third generation AHSS in combination with the fast cooling rates during RSW of several thousand K/s leads to a very hard and brittle martensitic fusion zone (FZ) with poor mechanical properties. Therefore, the resistance spot weldability of third generation AHSS is restricted [10].

Since the exact mechanisms leading to the inferior mechanical properties are not fully understood yet and still controversially discussed, the aim of this thesis was to investigate the resistance spot weldability of third generation AHSS, on the example of a TBF and a novel medium-Mn steel, with respect to the microstructural evolution and its influence on the mechanical properties. For this purpose, the microstructure of the FZ and heat-affected zone (HAZ) was characterized using various methods such as light optical microscopy (LOM), scanning electron microscopy (SEM), electron backscatter diffraction (EBSD), energy dispersive X-ray spectroscopy (EDX) and hardness mappings in order to correlate the presence of certain microstructural features with the mechanical properties determined by cross-tension strength (CTS) tests. The unfavorable microstructural constituents were modified by performing different in-process heat treatments achieved by a second pulse, whereby the heat input during the second pulse was visualized via the recorded resistance curves, which is intended to enable future targeted process control. In addition to the characterization of the HAZ of the medium-Mn steel with regard to the microstructure and the local mechanical properties, a thermal simulator was used to create samples whose microstructure resembled the microstructure of the various positions in the HAZ. The austenite content was determined magnetically and the mechanical properties were evaluated by tensile testing on these heat treated samples. These results are intended to support targeted HAZ designing in the future.

The following pages give an overview of the steel grades and methods used as well as the state of the art of RSW of third generation AHSS, which is followed by a summary of the most important findings from the four publications given in Part B. Part A concludes with an outlook and an assessment of the contributions presented in this thesis to the field of research.

2. State of the art

2.1. Advanced high strength steels (AHSS) for automotive applications

Steels which combine a tensile strength above 600 MPa with adequate formability and therefore meet the requirements of the modern automotive industry with regards to lightweight construction are generally defined as AHSS [5]. Diagrams that depict the ultimate tensile strength (UTS) and total elongation (TE), as illustrated in Figure 1, are commonly used to compare the various automotive steels to each other [5]. As AHSS are located in the right third of Figure 1, these steels are particularly suitable for the use in safety-relevant components, which require high strength. The development of the first generation of AHSS goes back to the 1990s. This generation mainly consists of TRIP and dual phase (DP) steels, but also fully martensitic press-hardening steels (PHS) with a tensile strength of up to 2000 MPa belong to it. In the early 2000s, the development of so-called twinning-induced plasticity (TWIP) steels was pushed forward, which are referred to as the second generation of AHSS and are characterized by a combination of high strength and outstanding formability that has never been achieved until today [11]. However, due to their high costs, challenges regarding manufacturing and their susceptibility to hydrogen embrittlement, these steels have never been able to establish themselves for commercial applications. With the development of the third generation AHSS, an attempt was made to approach the superior mechanical properties of TWIP steels at significantly lower costs due to the reduction of alloying elements. Therefore, today's automotive industry aims to replace the existing AHSS grades with these novel grades that offer significantly higher strength at comparable formability, a trend the European steel industry is following [5,12,13]. Only the PHS cannot be replaced by third generation AHSS due to their unmatched ultrahigh strength at very low deformation, which ensures their usage in crash-relevant components such as the B-pillar [14].

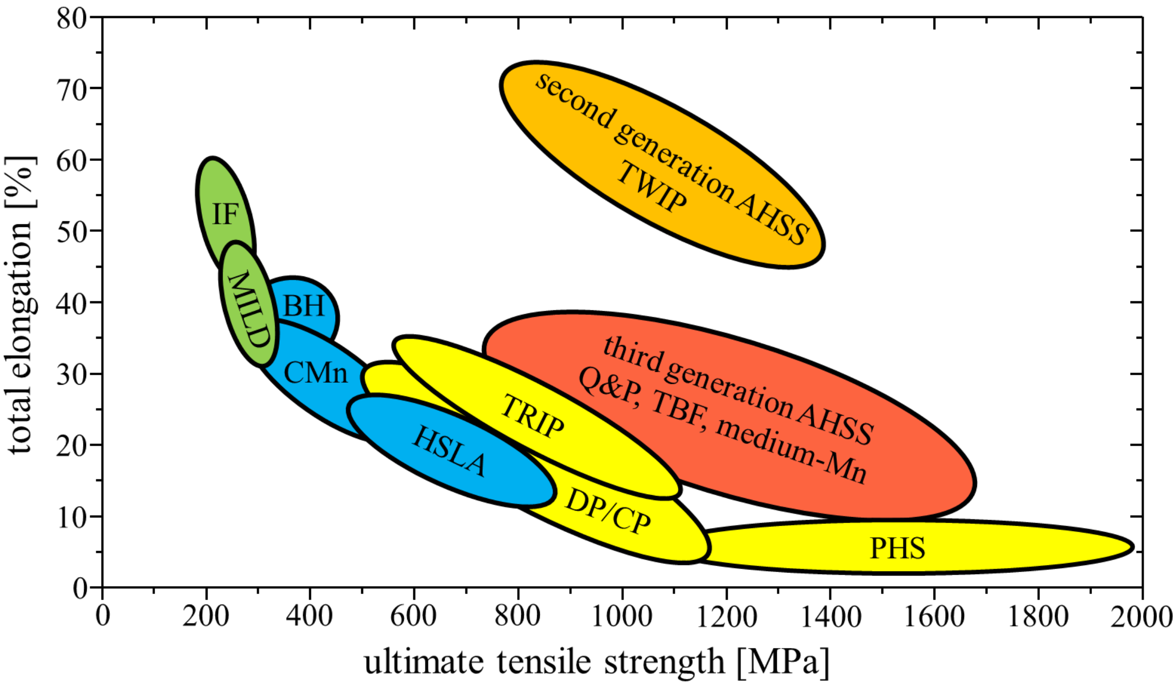

Figure 1*: Comparison of various steels for automotive applications concerning their ultimate tensile strength (UTS) and total elongation (TE). The interstitial free (IF) and mild steels belong to the lower strength steels (green). Bake-hardening (BH), carbon-manganese (CMn) und high-strength low-alloy (HSLA) steels belong to the conventional high strength steels (blue). The transformation-induced plasticity (TRIP), dual phase (DP), complex phase (CP) and press-hardening steels (PHS) represent the first generation of AHSS (yellow). The second generation of AHSS consists of the austenitic twinning-induced plasticity (TWIP) steels (orange). The third generation AHSS, which are shown in red, are trying to close the gap between the first and second generation of AHSS (adapted from [5]).*

2.2. Third generation advanced high strength steels

The third generation AHSS, consisting of Q&P steels, TBF steels and medium-Mn steels, are characterized by excellent formability due to their high austenite content, which enables the so-called TRIP effect. First described in the 1960s by Zackey et al. [15], the TRIP phenomenon is based on the strain-induced transformation of metastable austenite into martensite. This results in a significant increase of the local dislocation density, which inhibits further strain localization and therefore necking in this region [16]. With continued loading, the mechanism repeats in the adjacent regions, which leads to a significant increase in uniform elongation [17]. The austenite is stabilized by means of a heat treatment resulting in a redistribution of carbon in the case of Q&P [18] and TBF steels [19], as opposed to medium-Mn steels, where the stabilization of the austenite is mainly achieved by manganese enrichment [20]. In this thesis, the weldability of TBF and medium-Mn steels is investigated and therefore their manufacturing route, microstructure and mechanical properties are described in the following sections.

2.2.1. TRIP-aided bainitic ferrite (TBF) steels

The development of TBF steels goes back to the idea of developing a material with a considerable proportion of metastable austenite to enable the TRIP effect, that contains no ferrite and exhibits a bainitic instead of martensitic matrix in order to reduce the differences in hardness between the phases, which avoids stress-induced cracking [5]. This microstructure is adjusted by a heat treatment, which is schematically illustrated in Figure 2a. A complete austenitization of the initial material is carried out, followed by rapid cooling and isothermal annealing between the bainite start and the martensite start (M_s)-temperature, which is generally referred to as “austempering”. The formation of bainitic ferrite and carbon enrichment of the austenite takes place simultaneously during the isothermal step. The carbon enriched austenite remains mainly stable during the final cooling step, although, depending on the parameters, a certain amount is often undesirably transformed to martensite [21,22]. The resulting multiphase microstructure of the TBF steel is shown in Figure 2b. It consists of bainitic ferrite, retained austenite and small proportions of martensite. The martensite is commonly located next to stable austenite and forms so-called M/A-islands, which are a mixture of martensite and austenite [19,23]. The quantity, stability and shape of the austenite is determined by the annealing conditions and influences the mechanical properties of the TBF steel to a large extent [7,21,24–27]. Consequently, carbon is the most important alloying element, as it stabilizes the austenite most effectively. To enable this stabilization, silicon is also added, since it has almost no solubility in cementite and thus prevents carbide precipitation. Manganese, as an effective austenite stabilizer and solid solution hardener, is also alloyed [19,21,22,25,28]. TBF steels have a typical chemical composition of about 0.2 C/1.5 Si/2.5 Mn (wt%) and reach an UTS of up to 1200 MPa at a high total elongation [5].

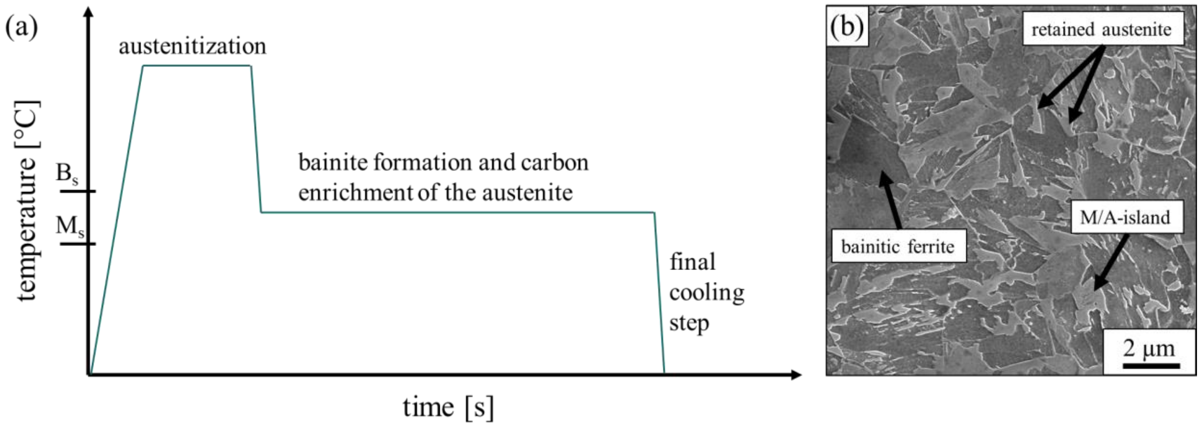

Figure 2: a) Schematic illustration of the heat treatment of TBF steels and b) SEM image of the microstructure of a TBF steel after the final cooling step.

2.2.2. Medium-Mn steels

In 1972, Miller [29] already developed an ultrafine-grained steel by annealing a work-hardened 0.1 C/5 Mn steel in the lower intercritical range, which not only exhibited high strength but also a total elongation of approximately 30 % due to the presence of metastable retained austenite. The foundation stone for today's medium-Mn steels was laid. Nevertheless, it took more than 30 years until Merwin [8] revived this concept and adapted it for a batch annealing route and thus initiated intensive research on this field, which is still ongoing today. Just like the other third generation AHSS grades, medium-Mn steels make use of the TRIP effect. However, the austenite is not stabilized by carbon but mainly by manganese, which is why a manganese content of 4-10 % is generally required and the carbon content can be reduced significantly [5,8,17,30,31]. For the so-called two-step concept, which was applied to the medium-Mn steel investigated in this work and is illustrated in Figure 3a, the cold rolled material is fully austenitized and quenched to martensite first. The manganese enrichment of the austenite takes place during the subsequent intercritical annealing. The microstructure after the final cooling consists of a ferritic matrix with an austenite phase fraction of up to 30 % depending on the annealing conditions. The stability of the retained austenite, which depends not only on its manganese content but also on its grain size, morphology and the surrounding matrix, essentially determines the mechanical properties [17,32–36]. The heat treatment leads to predominantly lath-like austenite due to the initial needle-shaped martensitic microstructure, as shown in Figure 3b. This lath-like austenite is reported to be more stable than globularly shaped austenite generated by the competing one-step heat treatment concept, where the cold rolled material is directly intercritically annealed [20]. However, certain amounts of globular austenite are also present after the two-step heat treatment.

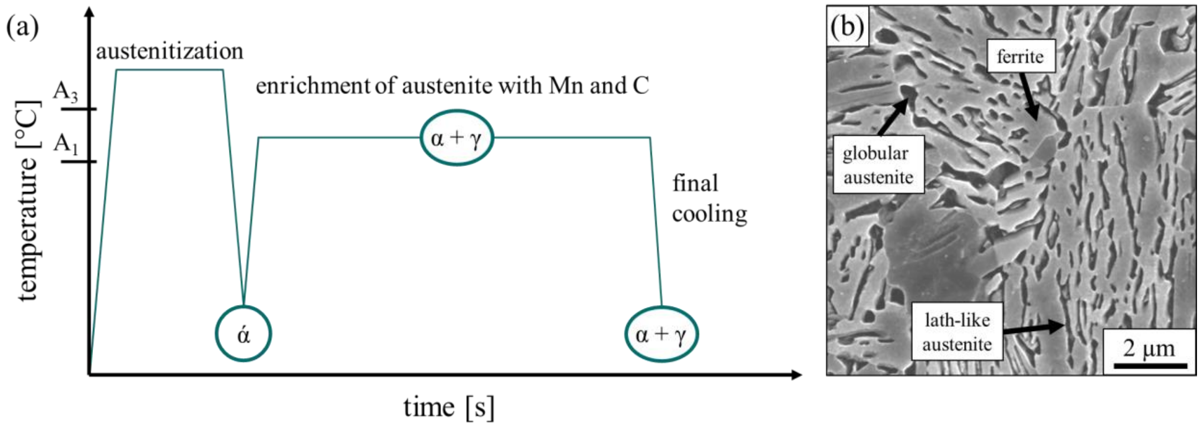

***Figure 3**: a) Schematic illustration of the two-step heat treatment of medium-Mn steels and b) SEM image of the microstructure of a medium-Mn steel after the final cooling step.*

2.3. Resistance spot welding (RSW)

2.3.1. Process and physical background

Weldability is one of the key factors regarding the use of materials for automotive applications. A high operation speed and the suitability for automation at low costs make RSW the dominant technology for sheet metal joining in the automotive industry. The body-in-white of modern cars consists of thousands of spot welds. RSW is based on the principle that heat is generated by the resistance of a material to the electrical current flow, which is known as the Joule´s law

$$\frac{Q_{\mathrm{w}}}{R(T)} = \underbrace{I^2 * t}_{const}$$

where Q_w is the generated heat in joules, I is the applied current in ampere, R(T) is the temperature-dependent and therefore dynamic resistance in ohm and t is the time in seconds. Steels are particularly well suited for RSW due to their high electrical resistance compared to other automotive materials like aluminum [9,10,37–39].

The RSW setup is schematically shown in Figure 4a. The required electrical current is supplied via two water-cooled copper-based electrodes. They also provide the clamping force to fix the sheets and to bring the surfaces in contact. The total resistance is composed of the resistance of the copper electrodes (R_1 & R_7), the resistance between the electrode and the sheets (R_2 & R_6), the resistance of the sheets being welded (R_3 & R_5) and the resistance at the interface of the sheets (R_4). Since R_4 is usually the highest resistance, heat is predominantly generated at the interface between the sheets, and thus the formation of the FZ [9,10,40]. The evolution of the FZ, also called the weld nugget, can be illustrated by the curve of the electrical resistance illustrated in Figure 4b. The first peak represents the contact resistance at the interface of the sheets. It breaks down within milliseconds to a minimum, which is referred to as the α-trough. Due to the increase of the temperature also the resistance increases with time, while local melting facilitates the current flow and thus reduces the resistance. This interplay reaches its equilibrium at the so-called β-peak. At this point, the temperature stabilizes and the nugget growth starts to dominate, which causes the resistance to decrease till the current is switched off. The water cooled electrodes represent strong heat sinks, which cause extremely high cooling rates of several thousand K/s during the subsequent holding step. Once the electrodes are released, the welding process is finished [41–44].

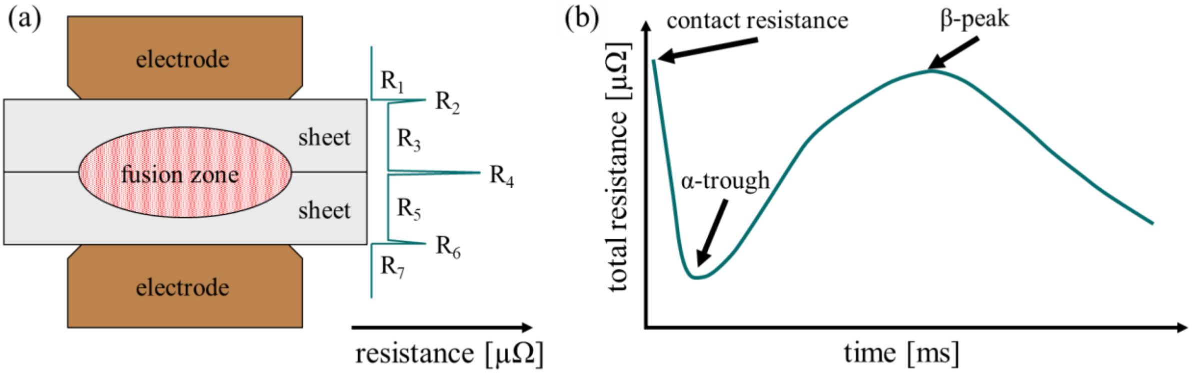

***Figure 4**: a) Schematic illustration of the RSW process (adapted from [10]) b) schematic illustration of the electrical resistance curve during welding (adapted from [41]).*

2.3.2. Welding parameters

The shape and size of the weld nugget are decisive in terms of the performance of the automotive components. A small nugget offers only a small load-bearing area, which usually results in a low strength of the joint. However, the size of the weld nugget cannot be enlarged beyond a certain dimension, due to the occurrence of expulsion at excessively high heat inputs, which affects the joint quality and reproducibility in a negative way [9]. Besides the electrode pressure, the welding time and the current are the most important parameters to be adjusted. With regard to processing, it is common to specify welding ranges for the different materials depending on the sheet thickness and possible coatings. For this purpose, the current is increased step by step and the resulting weld nugget, which has been cracked with a chisel, is surveyed. The current which produces a nugget with a predefined minimum diameter, for example $4 \times \sqrt{t}$, where t is the sheet thickness, as recommended by the American Welding Society [45], is specified as the lower limit (I_{min}). The highest current, at which no expulsion occurs, is referred to as the upper limit (I_{max}), as schematically shown in Figure 5. The determination of the current range at different welding times results in lobe curves, which specify the welding range for acceptable welds in production [10,40,46].

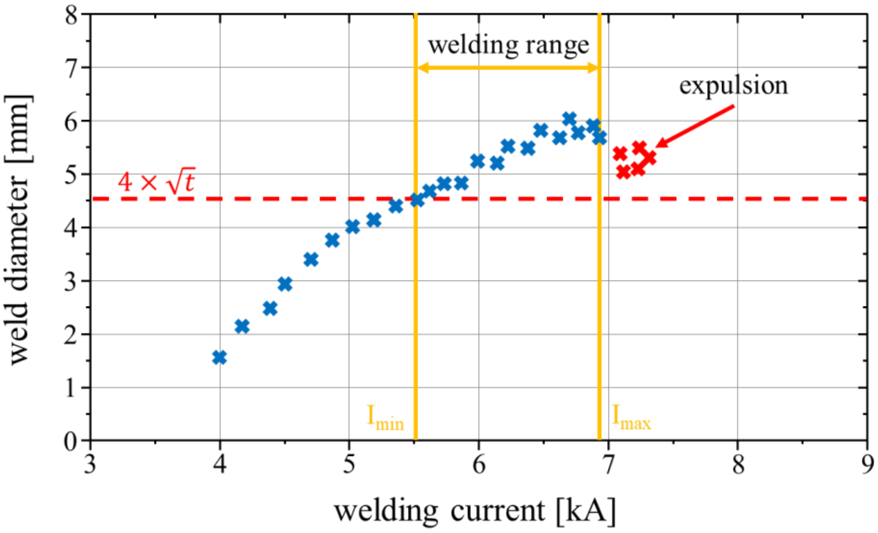

***Figure 5**: Schematic illustration of the determination of the welding current range at a constant welding time.*

2.3.3. Mechanical testing: the cross-tension strength (CTS) test

In addition to a large welding range and the insusceptibility to defects such as shrinkage voids, the results of mechanical testing is also important in order to assess the weldability of materials and their suitability for automotive applications. Along with the tensile-shear strength (TSS) test and various technological test methods, the CTS test, whose setup is schematically shown in Figure 6a, has established itself for comparing the mechanical properties of spot welds [10]. The bearable load quantified via the maximum force F_{max} under the given loading condition and also the failure energy, which is given by the area under the load-displacement curve and correlates with the crash behavior, as illustrated in Figure 6b, are characteristic values obtained [9]. Moreover, the failure mode offers an evaluation of the weld quality [9,39,47–49]. There are basically three different failure modes to be distinguished from each other. The most favored failure mode is the pullout failure (PF) mode, where the crack propagates through the HAZ or even the base material (BM) rather than through the FZ, as schematically illustrated in Figure 6c. Joints that fail via this mode usually bear high loads and show high energy absorption capability, which ensures good crash behavior [9,49]. In contrast, if the crack propagates through the FZ, it is called interfacial failure (IF) mode, as schematically illustrated in Figure 6d. This mode is reported to lead to a significant deterioration of the crashworthiness due to little plastic deformation and is therefore unwanted [50,51]. A mixture of these modes is called partial interfacial failure (PIF) mode. The pullout ratio, which is the areal fraction of the pulled-out plug to the former FZ, represents a possibility to quantify the failure mode. Besides the fracture toughness of the FZ and the shear strength of the HAZ [49], which are defined by their microstructure and will be discussed later, also the size of the FZ is reported to be decisive regarding the failure mode. The smaller the FZ, the higher the tendency to fail via an unwanted IF failure mode [49,52–55].

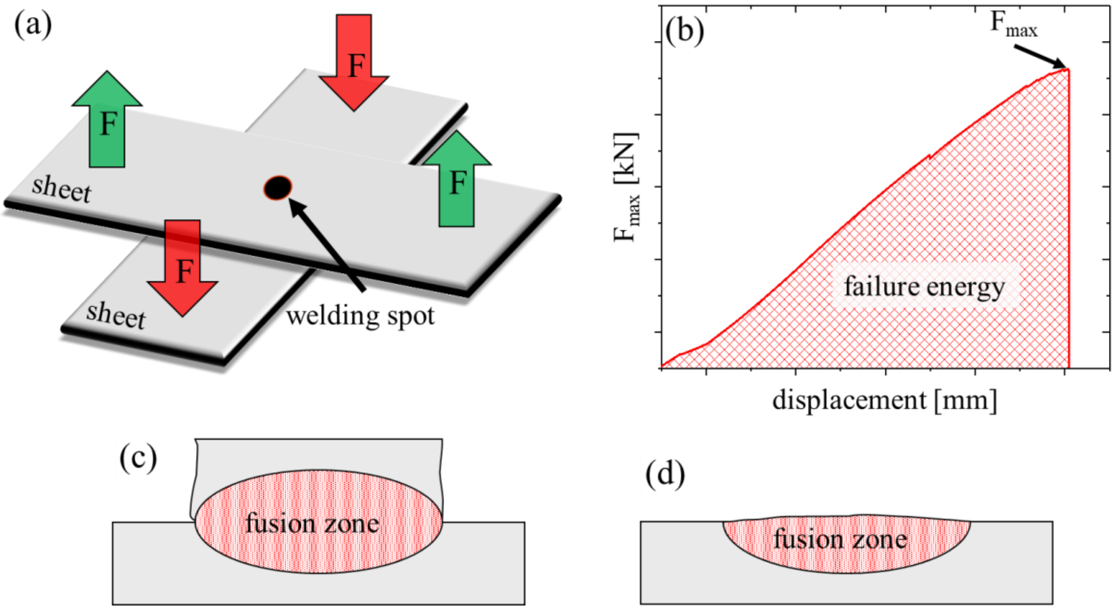

***Figure 6**: a) Schematic illustration of the CTS test setup, b) schematic load-displacement curve obtained and spot welds failed via the c) PF mode and via the d) IF mode*.

2.4. Resistance spot welding of AHSS: challenges and solutions

2.4.1. The fusion zone (FZ)

When discussing the weldability of AHSS, two different aspects have to be distinguished from each other. On the one hand, the high content of alloying elements compared to conventional automotive steels results in a high electrical resistance and therefore in a good weldability of uncoated AHSS sheets even at moderate current levels. On the other hand, also the mechanical performance of the joints, which mainly depends on the microstructure of the FZ and HAZ, has to be taken into account in assessing the weldability of AHSS and evaluating their suitability for automotive applications [56].

Due to the extremely high cooling rates of several thousand K/s during RSW, low alloyed steels tend to form a martensitic FZ. Its hardness increases with increasing carbon equivalent number (Ceq), which is primarily determined by the carbon content, but also strongly increases with other alloying elements such as manganese and silicon [39,57–61]. It is well documented that a pronounced hardening of the FZ reduces the toughness of the joint, which promotes the unwanted IF mode [55,62–64]. Since manganese and silicon play a decisive role in the alloying concept of third generation AHSS, the hardening is particularly pronounced for these steel grades [9,10] and they consequently tend to fail via the unwanted IF mode. If failing via the PF mode, F_{max} mainly correlates with the fracture toughness of the FZ, which is usually very low in the case of hard martensite [48,53]. A high hardness of the FZ may also lead to an increased susceptibility to hydrogen cracking after RSW, as frequently observed for arc welded steels [10]. Furthermore, alloying elements like silicon and manganese, as well as phosphorus, tend to segregate at grain boundaries and weaken them, which promotes intercrystalline fracture [65,66]. AHSS are also more susceptible to expulsion, which narrows the welding range [10] and increases the risk of void formation [49,59].

2.4.2. The heat-affected zone (HAZ)

In addition to the FZ, where the temperature rises above the melting point of the material, heat conduction always creates a surrounding HAZ, which has a strong influence on the mechanical performance of AHSS spot welds [9,59,67–70]. The precisely adjusted microstructure of the BM is completely rebuilt in the HAZ and can be subdivided in the following zones, as illustrated in Figure 7 [9,68,71,72]: Adjacent to the FZ, the temperature rises to just below the melting point during welding, resulting in austenitization at high temperatures with pronounced grain growth. The subsequent rapid cooling leads to a coarse-grained martensitic microstructure after welding, which is why this zone is referred to as the coarse-grained heat-affected zone (CGHAZ). This zone tends to exhibit brittle behavior due to a high hardness, coarsened microstructure and possible segregation of alloying elements. If the crack propagates through this zone, which is the case for the PF mode, the mechanical properties of the welds are mainly determined by its microstructure [67,70,73,74]. With increasing distance to the FZ, the temperature continuously decreases, which inhibits grain growth during the austenitization and leads to a finer martensite after quenching in the so-called fine-grained heat-affected zone (FGHAZ) for most AHSS [68,71,72]. Therefore, both strength and ductility are significantly improved in the FGHAZ compared to the CGHAZ [68]. In the case of medium-Mn steels, however, the temperature is not high enough to homogenize the manganese enrichments needed to stabilize the austenite, which is why a high fraction of austenite remains stable in the FGHAZ [69,75]. The retained austenite is mainly responsible for the improved ductility of this zone compared to the CGHAZ [69]. CGHAZ and FGHAZ are both part of the upper critical heat-affected zone (UCHAZ), where the peak temperature generally rises above A_3. The temperature in the intercritical heat-affected zone (ICHAZ) is between A_1 and A_3 and leads to the formation of a ferritic and austenitic microstructure during the welding process for most AHSS [9,72,68]. During cooling, the austenite transforms into martensite and the final microstructure therefore resembles a dual phase steel. The strength of this zone is significantly lower compared to the UCHAZ, at a higher total elongation [68]. The zone where the temperature is below A_1 and therefore no phase transformation takes place is called the subcritical heat-affected zone (SCHAZ). If the BM of a steel contains martensite or bainite, this zone undergoes tempering and is therefore significantly softer than the BM [9,71]. The degree of softening, which mainly depends on temperature but also on the welding time, is very pronounced in the case of fully martensitic PHS [71,72,76], but also the tempering of the martensitic phase components in DP steels is well documented [77–80]. This softened zone acts as a preferential location for necking, which may lead to premature failure [50,72,81–83].

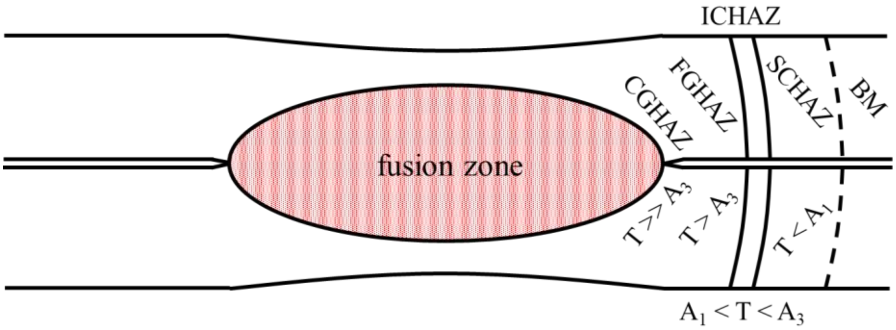

***Figure 7**: Illustration of the subdivided HAZ from the inside out: coarse-grained heat-affected zone (CGHAZ), fine-grained heat-affected zone (FGHAZ), intercritical heat-affected zone (ICHAZ), subcritical heat-affected zone (SCHAZ) and the base material (BM) with the associated temperature ranges.*

2.4.3. In-process heat treatments

As mentioned above, a major issue regarding the weldability of AHSS is the excessive hardening of the FZ and the associated embrittlement. In order to increase the toughness, an in-process tempering heat treatment can be carried out by means of a second pulse, which is hereinafter referred to as the temper pulse concept and schematically illustrated in Figure 8a. The first pulse is followed by a cooling step, which aims to cool down the FZ below the martensite finish (M_f)-temperature. During the low current second pulse, the FZ is reheated and tempered, which is associated with a reduction in hardness and an increase in toughness [9]. The heat input during the second pulse, which is determined by the pulse time and current, must be adjusted precisely to achieve the desired tempering. If the heat input is too low, the FZ is insufficiently softened and if the input is too high, the FZ re-austenitizes and transforms again to hard martensite during the final quenching [84]. Furthermore, temper embrittlement phenomenon can occur in a certain temperature range [85]. This approach was already applied at the beginning of the 21st century for TRIP steels [84,86] and has experienced a renaissance in recent years due to the development of new AHSS and their problems regarding the hardening of the FZ.

Investigations on a high strength automotive steel showed that the failure mode during the peel test of temper pulse welded samples was significantly enhanced, but there was no significant improvement of the failure mode or maximum load during the TSS test [87]. In contrast, the mechanical properties of a martensitic stainless steel improved for both the TSS and CTS test by applying temper pulsing with suitable parameters [85]. Among modern AHSS, improved mechanical properties due to a temper pulse have already been documented for TRIP [88] and DP steels [89,90], and recently published papers even adapted this approach to a medium-Mn steel [91,92]. However, the temper pulse concept has not yet been able to establish itself in practice. This may be related to the complex determination of suitable parameters and the fact that the process time increases significantly due to the long cooling time, which deteriorates the economic efficiency. Nevertheless, it is very promising for improving the mechanical properties of third generation AHSS welds and since the underlying mechanisms are not fully understood yet [9], research in this field is necessary.

Another way to improve the mechanical properties of resistance spot welded AHSS by means of an in-process heat treatment lies in the recrystallization pulse concept. Here, the FZ cools down to just below the melting temperature after the first pulse and the outer FZ recrystallizes during the second pulse. As can be seen in Figure 8b, this method is characterized by a high current second pulse and a short cooling time, which results in a significantly increased economic efficiency compared to the temper pulse concept. The mechanical properties of modern DP and TRIP steels have significantly been improved with this approach [93,94]. However, investigations on a DP1000 steel illustrated the sensible response of the material to different welding parameters [74,95]. If the first pulse was welded with I_{max} for example, a subsequent second pulse of the same current led to a significant improvement of the mechanical properties. This was mainly attributed to the recrystallization of the outer FZ and the associated relief of residual stresses, as well as the increased number of high angle grain boundaries in the CGHAZ, which are believed to promote crack deflection. Additionally, it was assumed that the severe softening of the SCHAZ reduces the stress concentration at the outer

FZ and thus supports the failure outside the FZ [74]. In contrast, although the second pulse successfully recrystallized the outer FZ of joints welded at I_{min}, the mechanical properties deteriorated due to the reduction of compressive residual stresses and the lower fraction of high angle grain boundaries [95]. This approach is considered to be capable to overcome the poor weldability of third generation AHSS in the future, which is why intensive research is currently being carried out in this field [66,96–98].

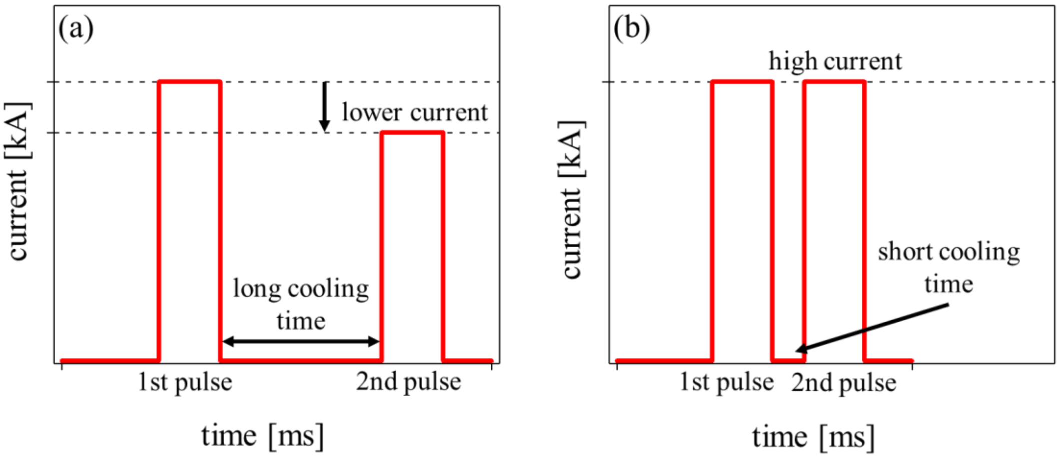

***Figure 8**: a) Illustration of the welding sequence of the a) temper pulse concept and the b) recrystallization pulse concept.*

The poor mechanical properties of Q&P steel welds were mainly attributed to phosphorus segregations at the grain boundaries of the outer FZ after a conventional single pulse. It was shown that they were more evenly distributed by a recrystallization pulse, preventing brittle fracture during the CTS test [97,98]. In other publications, it was assumed that the refinement of the martensitic blocks and packets, the globularization of the prior austenite grains (PAGs) and the homogenization of manganese segregations are responsible for improved properties due to double pulsing [66,96]. Due to their increased manganese content, manganese segregations play an even greater role in the FZ of medium-Mn steels. A post-weld heat treatment is also reported to improve the mechanical properties of these steels by lowering the segregations [92]. In contrast, the research by Park et al. [69] concluded that the inferior performance of medium-Mn steel welds during the CTS test is related to the embrittlement of the UCHAZ due to a high Ceq. This embrittlement was counteracted in subsequent work by means of a paint baking heat treatment [73]. Another work of this group focused on the effects of a second pulse on the microstructure of the CGHAZ by simulating the temperature cycle during RSW with a thermomechanical simulator, which can be seen as a first step towards targeted HAZ design [70]. In this context, a significant increase in toughness was observed by tempering effects.

2.5. Relation of the current thesis to the state of the art

Despite intensive research in recent years, the exact mechanisms leading to the poor mechanical performance of AHSS spot welds are still controversially discussed. Some blame segregations in the outer FZ, others the shape of the PAGs, distribution of the high angle grain boundaries, the residual stresses or the pronounced hardening of the FZ and still others account the embrittlement of the UCHAZ responsible for the unfavorable mechanical properties. Therefore, the present work aims to shed light on the not fully understood microstructure-property relationship of third generation AHSS steel welds. This is carried out on the example of a TBF and a medium-Mn steel, which represent the state of the art developments of automotive steels. In addition to microstructural characterizations of the FZ, one focus of this work lies on the microstructural changes of the HAZ, which are assumed to have a significant influence on the mechanical performance of third generation AHSS welds. In this regard, an approach is introduced that allows the investigation of the microstructure and local mechanical properties of the HAZ in a small step size, which is intended to be the basis for future targeted HAZ designing, without relying on elaborate finite element (FE) simulations. Based on this knowledge, it was possible to specifically modify the unfavorable microstructural features by double pulsing to significantly improve the mechanical performance of the welds. In order to overcome the trial and error approach of parameter selection, the temperature and thus microstructure development was visualized with the help of recorded electrical resistance curves, which allowed targeted process control.

The ultimate goal of this work is to expand the knowledge in the field of resistance spot welding of third generation AHSS in order to support their desired establishment for automotive applications.

3. Summary of publications

3.1. Appended Papers

The appended papers can be found in part B of this thesis.

Paper I

M. Stadler, M. Gruber, R. Schnitzer, C. Hofer

Microstructural characterization of a double pulse resistance spot welded 1200 MPa TBF steel

Welding in the World 64 (2020) 335-343

Paper II

M. Stadler, R. Schnitzer, M. Gruber, C. Hofer

Improving the mechanical performance of a resistance spot welded 1200 MPa TBF steel

International Journal of Materials Research 112 (2021) 262-270

Paper III

M. Stadler, R. Schnitzer, M. Gruber, K. Steineder, C. Hofer

Influence of the cooling time on the microstructural evolution and mechanical performance of a double pulse resistance spot welded medium-Mn steel

Metals 11 (2021) 270

Paper IV

M. Stadler, R. Schnitzer, M. Gruber, K. Steineder, C. Hofer

Microstructure and local mechanical properties of the heat-affected zone of a resistance spot welded medium-Mn steel

Materials 14 (2021) 3362

Contributions of the author: The author of this thesis is responsible for planning, conception and writing of all papers. The material was supplied by voestalpine Stahl Linz GmbH, where also the resistance spot welds were produced and all mechanical tests were performed. Additionally, the samples investigated in **Paper IV** were heat treated by means of a self-made thermal simulator at voestalpine Stahl Linz GmbH. All microstructural investigations were carried out at Montanuniversität Leoben by the author himself or under the author's supervision. The parameters for the welding experiments were conceptualized by the author and he is responsible for the interpretation of all results. Ronald Schnitzer, Martin Gruber, Katharina Steineder and Christina Hofer are gratefully acknowledged for their contribution to the papers.

3.2. Conference contributions

Stadler M., Gruber M., Schnitzer R., Hofer C. (2019) Microstructural characterization of a double pulse resistance spot welded 1200 MPa TBF steel, Oral presentation, 72nd IIW Annual Assembly and International Conference 2019, 7-12 July, Bratislava, Slovakia

3.3. Supervised theses

Karner M. (2020) Verbesserung mechanischer Eigenschaften eines widerstandspunktgeschweißten pressgehärteten Stahls durch das Doppelimpulsverfahren. Bachelor Thesis, Montanuniversität Leoben.

3.4. Summary of published contents

3.4.1. Aim and scope of the investigations

One aim of the current thesis was to obtain a deeper understanding of the microstructural evolution of a 1200 MPa TBF steel with a chemical composition of 0.2 C/1.5 Si/2.5 Mn (wt%) during RSW and to derive the reasons for the, in part, inferior mechanical performance of the welds. The microstructural characterization was mainly based on hardness mappings as well as LOM and SEM investigations, using different etchants such as Nital and picric acid to visualize the microstructural constituents. In addition, EBSD was used to determine the orientation of the martensite and to visualize the cast-like structure and the shape and orientation of the PAGs. Based on these findings, it was attempted to modify the microstructure by double pulsing in order to create welds with superior mechanical properties determined by CTS tests. To achieve this, it was necessary to constantly adjust the parameters and simultaneously investigate the microstructural response of the material in order to fundamentally understand how different microstructural features define the mechanical properties of the welds. The results of the investigations on this TBF steel were published in **Paper I** and **Paper II**.

Subsequently, it was attempted to transfer the knowledge gained to a medium-Mn steel with a minimum tensile strength of 780 MPa and a nominal chemical composition of 0.1 C/6.4 Mn/0.6 Si (wt%), which showed similar deficiencies during CTS tests. The concept of an in-process heat treatment by means of a second pulse was adapted to this third generation AHSS grade as well, in order to modify the microstructure towards enhanced mechanical properties. The results of these investigations were published in **Paper III**. Since this steel grade is still under development, there are hardly any experimental data, which is why a detailed characterization of the FZ and HAZ was carried out. In this context, a thermal simulator was used to investigate the microstructure and determine the local mechanical properties of various positions of the HAZ, which was published in **Paper IV**.

To sum up, the following main questions were intended to be answered by this thesis:

- Which methods are suitable to characterize the FZ and HAZ?
- Which microstructural features lead to the inferior mechanical performance of third generation AHSS?
- How can these features be modified towards improved mechanical properties?
- Which double pulsing parameters lead to the best mechanical performance of the welds with the highest possible economic efficiency and how can the heat input be controlled.

The following pages summarize the findings published in the papers appended in part B that address the issues described above.

3.4.2. Influence of a temper pulse on the microstructure of the FZ and HAZ

At first, a basic understanding of the microstructure of the FZ and HAZ during RSW of a TBF steel needed to be established in order to deduce the reasons for the inferior mechanical performance of the joints and to evaluate potential remedial measures. The results published in **Paper II** show that the inferior mechanical properties of single pulse welded joints can mainly be attributed to a combination of the high hardness and the cast-like structure of the outer FZ. The hardening was attempted to be counteracted by means of a second pulse, which was intended to temper and therefore soften the brittle martensitic FZ. However, in order to successfully apply the temper pulse concept to the TBF steel, the underlying mechanisms regarding the heat generation and the microstructural evolution in the FZ and HAZ during the second pulse had to be investigated. The related results published in **Paper I** illustrate that the two pulses must be adjusted very precisely to each other in order to achieve satisfactory results. A temper pulse of 4.5 kA after a cooling time of 1000 ms for examples results in both a re-hardening of the very inner FZ and a pronounced softening of the HAZ if the first pulse is welded with I_{min} (5.5 kA), as illustrated by the hardness mapping in Figure 9a.

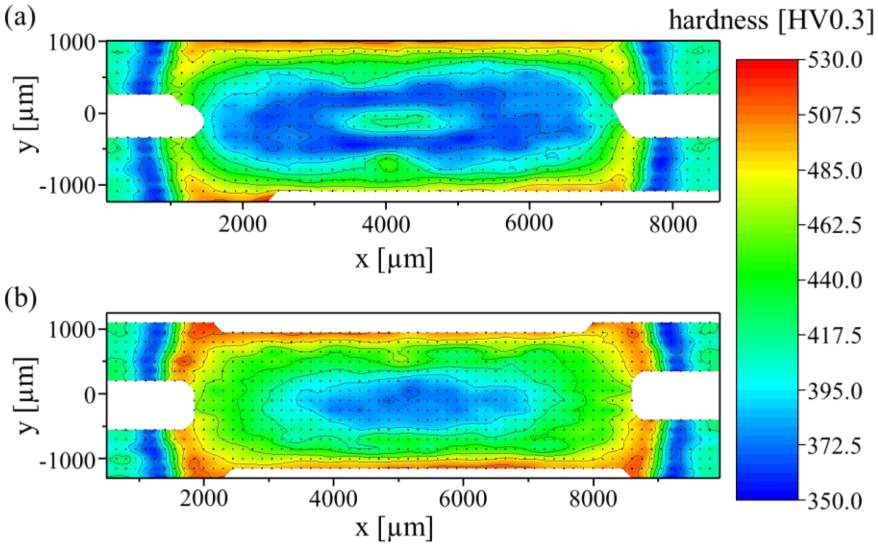

***Figure 9**: Hardness mappings of TBF welds heat treated with a temper pulse of 4.5 kA subsequently to a first pulse welded with a) I_{min} (5.5 kA) and b) I_{max} (6.8 kA) (adapted from **Paper I**).*

As shown by the SEM images in Figure 10a, the harder inner FZ consists of a dual phase microstructure of ferrite and martensite, indicating that the temperature during the second pulse was between A_1 and A_3 and thus was too high for the aimed tempering. In contrast, the temperature in the outer FZ was just below A_3 and the martensite is therefore strongly tempered, as shown in Figure 10b. Undesirably, the HAZ is tempered as well, which is visualized by the hardness mapping in Figure 9a. The pronounced tempering of the HAZ can also be derived from the SEM image of the ICHAZ in Figure 10c. Due to the elevated temperature during the second pulse, the martensite in the ICHAZ is tempered. The results of **Paper I** also illustrate that, besides the visualization of the solidification structure, picric acid etching is a capable method to estimate the degree of tempering in the UCHAZ. If the martensitic UCHAZ is strongly tempered, as was the case for the specimen welded with I_{min} for the first pulse, phosphorus migrates to the PAG boundaries and is preferentially attacked by the etchant. Besides the degree of tempering, also the size and shape of the PAGs in the

UCHAZ can therefore be estimated by means of picric acid etching without requiring extensive EBSD measurements, as shown in Figure 10d.

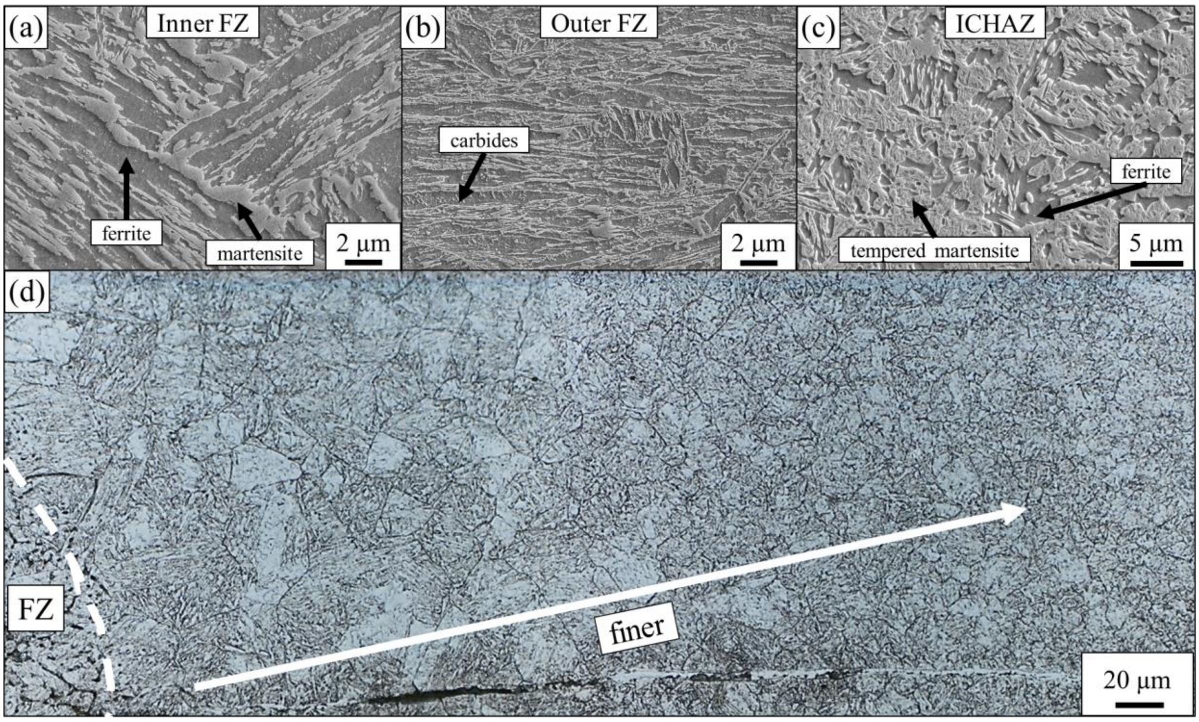

***Figure 10**: SEM images of the a) inner FZ, b) outer FZ and c) ICHAZ of the TBF steel welded with a temper pulse subsequently to the first pulse welded with I_{min}. d) LOM image of the UCHAZ of the same sample with the PAGs being revealed by picric acid etching (adapted from **Paper I**).*

In contrast, a temper pulse of 4.5 kA subsequent to a first pulse welded with I_{max} (6.8 kA) results in a softened FZ, whose hardness increases from the inside out, and a still hard and therefore strong HAZ, as shown in Figure 9b. During the second pulse, the temperature of the FZ did not exceed A_1 at any time, resulting in tempered martensite in the inner FZ, as shown in Figure 11a. The lower heat input during the second pulse is also illustrated by the untempered martensite in the ICHAZ, as shown in Figure 11b.

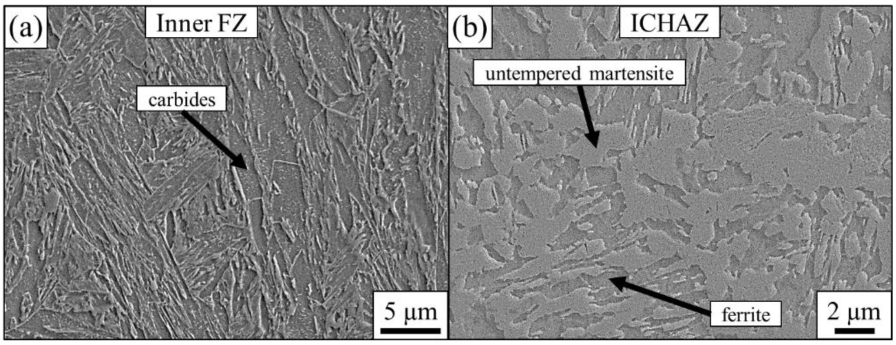

***Figure 11**: SEM images of the a) inner FZ and the b) ICHAZ of the TBF steel welded with a temper pulse subsequently to the first pulse welded with I_{max} (adapted from **Paper I**).*

On the one hand, the microstructural features discussed in **Paper I** are attributed to the fact that a lower energy input during the first pulse leads to a smaller electrode indentation compared to the joint welded with I_{max} at the first pulse. This results in a slower cooling of the FZ between the two pulses and the temperature at the beginning of the second pulse is consequently higher. According to Joules law of $Q_w = I^2 \times R(T) \times t$, the given temper pulse leads to a higher energy input and to an elevated temperature during the second pulse. On the other hand, the FZ is significantly smaller if welded with I_{min} at the first pulse. This results in a higher ratio of the passing current to the size of the FZ during the second pulse and therefore more heat is generated. To sum up, the findings of **Paper I** demonstrate how the microstructural evolution during RSW is affected by a temper pulse and that the second pulse must be precisely adjusted to the first pulse in order to achieve acceptable results.

3.4.3. Correlation between the microstructure and mechanical properties of temper pulse and recrystallization pulse welds

Based on the knowledge gained from the results published in **Paper I**, various concepts of targeted modification of the microstructure of the TBF steel welds towards enhanced mechanical properties, namely the concepts of an extended single pulse, a temper pulse and a recrystallization pulse, were compared and the results were published in **Paper II.** The various welding parameters can be found in the experimental section of **Paper II**. It is shown that the simple extension of the welding time does not lead to an assumed enlargement of the FZ and therefore no significant improvement of F_{max} during the CTS test can be achieved by this approach, as illustrated in Figure 12.

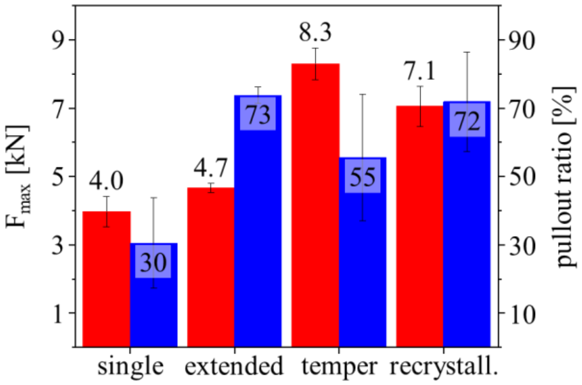

Figure 12*: Average maximum force (red bars) and pullout ratio (blue bars) obtained by CTS tests for the various welding concepts for the TBF steel (n = 10) (adapted from* ***Paper II****).*

In contrast, by applying a second low current temper pulse after a long cooling time, F_{max} is significantly increased, as shown in Figure 12. Although the size of the FZ does not change, F_{max} is more than doubled, which is attributed to the softening of the FZ and the associated improvement in toughness. The hardness profile shown in Figure 13b, with a softened and therefore tough FZ and a still hard and therefore strong HAZ, compared to the single pulse in Figure 13a, turned out to be ideal in terms of the mechanical performance, as can be seen in Figure 12.

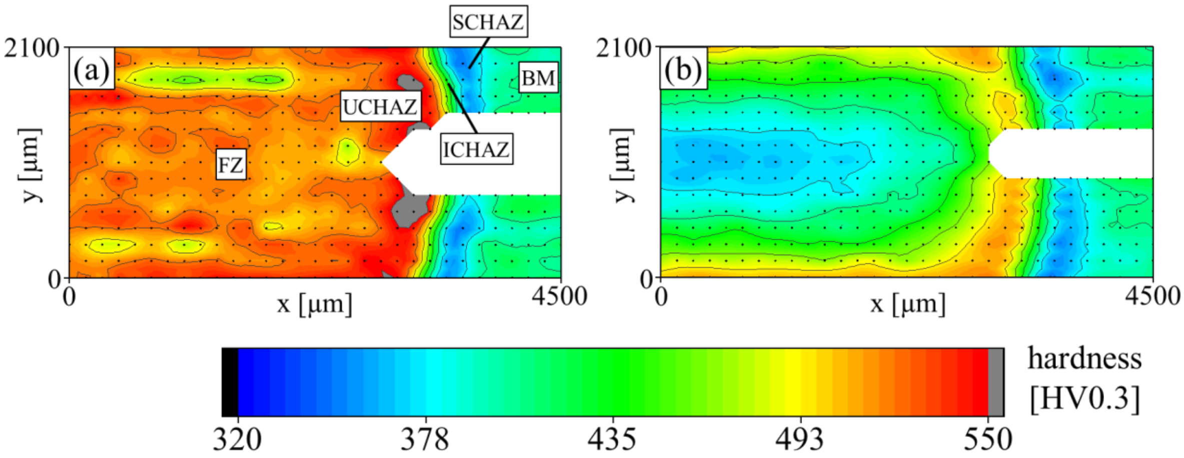

Figure 13*: Hardness mapping of the a) single pulse TBF weld and the b) ideal temper pulse weld (adapted from* ***Paper II****)*

An increase of F_{max} is also achieved by applying a high current recrystallization pulse after a short cooling time. As the name suggests, the aim of this concept is to recrystallize the outer

FZ and thus modify the cast-like structure. The recrystallization was visualized by means of the shape of the PAGs reconstructed with the ARPGE software package [99] from the inverse pole figure (IPF) maps obtained by EBSD data. As shown by the bold black lines in Figure 14a, the PAGs in the outer FZ of the single pulse weld are elongated and oriented alongside the maximum heat dissipation, corresponding to a cast-like structure, which offers low toughness. Due to the recrystallization pulse, a globularization of the grains could be achieved, as illustrate in Figure 14b, which leads to an improved crack deflection capacity and thus to a significantly higher strength of the welds, as proven by Figure 12.

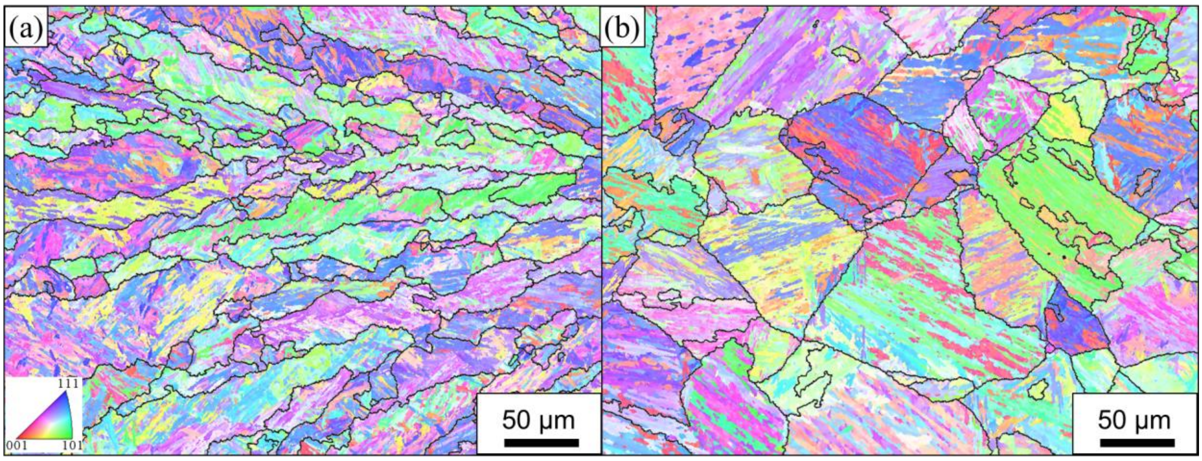

Figure 14*: IPF maps with the reconstructed PAGs highlighted with bold black lines of the outer FZ of the a) conventional single pulse and b) recrystallization pulse TBF weld (adapted from* ***Paper II****).*

Besides the reconstruction of the PAGs, the EBSD data were also utilized to analyze the misorientation distribution of the grain boundaries in the martensitic microstructure. As shown in Figures 15b-d, the higher energy input of all presented concepts leads to an increased fraction of high angle grain boundaries close to 60 °, compared to the single pulse weld in Figure 15a. As discussed in more detail in **Paper II**, these high angle grain boundaries are more capable of deflecting a crack towards the HAZ, which results in a large pullout ratio for all three approaches, as shown in Figure 12.

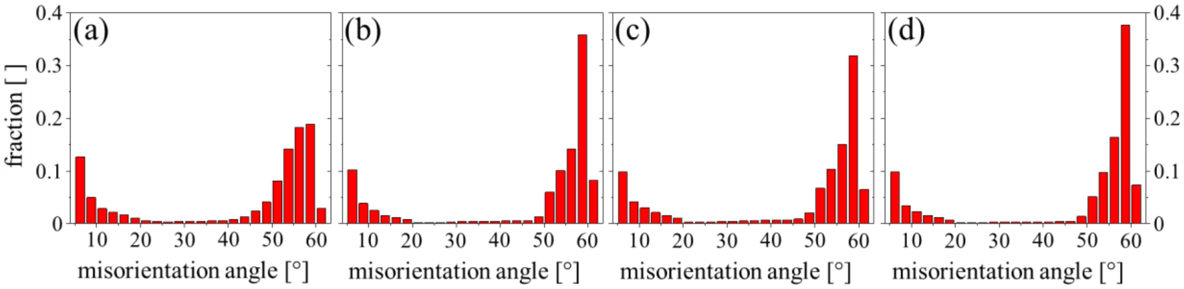

***Figure 15**: The distribution of the misorientation angles in the outer FZ of the a) conventional single pulse, b) extended single pulse, c) temper pulse and d) recrystallization pulse TBF weld (**Paper II**).*

The results of **Paper II** demonstrate that the elimination of just one of the detrimental factors, namely the pronounced hardening or the cast-like structure of the outer FZ, is already enough to significantly improve the mechanical performance of a resistance spot welded 1200 MPa TBF steel. However, due to the shorter cooling time between the pulses and the associated improved economic efficiency compared to the temper pulse concept, the recrystallization pulse concept is more promising to be implemented into the body-in-white production. Therefore, the subsequent focus regarding the improvement of the weldability of the medium-Mn steel was laid on this approach.

3.4.4. Influence of the cooling time between the first pulse and the recrystallization pulse

The content published in **Paper III** deals with the effects of the recrystallization pulse on the microstructure and properties of medium-Mn steel welds, with particular emphasis on the role of the cooling time between the pulses. As demonstrated by the results of the CTS tests in Figure 16, the cooling time influences the mechanical performance of the welds significantly. By applying a recrystallization pulse after a very short cooling time of 20 or 50 ms, F_{max} can roughly be doubled compared to the single pulse weld. With extended cooling times, F_{max} decreases again, which illustrates the narrow process window for successful double pulsing. In contrast to the TBF steel, however, the failure mode quantified by the pullout ratio improves just slightly due to double pulsing and does not correlate with the cooling time. The underlying reasons are not fully understood yet.

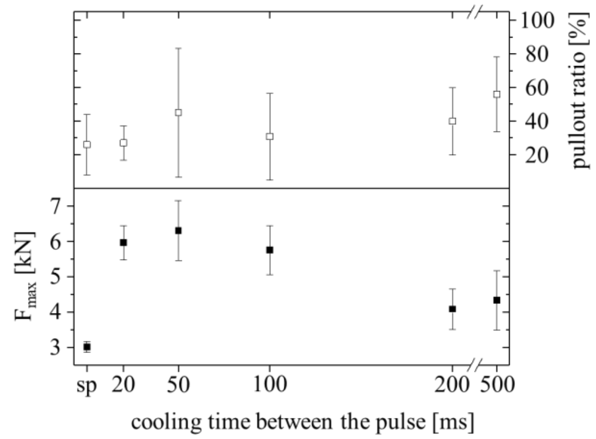

***Figure 16**: Average maximum force F_{max} and pullout ratio obtained from CTS tests (n = 5) of recrystallization pulse medium-Mn welds with different cooling times, compared to the single pulse weld (sp) (**Paper III**).*

In order to understand the influence of the cooling time on the heat generation and consequently the microstructural evolution during the second pulse, dynamic resistance curves were calculated via the voltage measured at the electrodes and the applied current. As can be seen in Figure 17a, the resistance during the first pulse has a course typical for AHSS, as already described in Figure 4, and ends at about 115 µΩ. Since the nugget has always the same size after the first pulse, the resistance at the beginning of the second pulse only depends on the temperature of the FZ and is therefore an indication of the cooling between the pulses. As can be seen in Figures 17b-f, it continuously decreases with increasing cooling times. Since the energy input during the second pulse is a function of the temperature dependent electrical resistance, this results in a reduced energy input by the given second pulse after longer cooling times, which is also illustrated by the decreasing area under the resistance curves from Figure 17b to Figure 17f. Based on the results of the CTS tests, a moderate resistance drop from 115 µΩ to 90 µΩ, as shown in Figure 17c, during the cooling time between the pulses is ideal. In contrast, if the resistance drop is too pronounced, such as from 115 µΩ to 40 µΩ, as shown in Figure 17e, the second pulse does not generate sufficient heat to achieve the desired in-process heat treatment of the FZ.

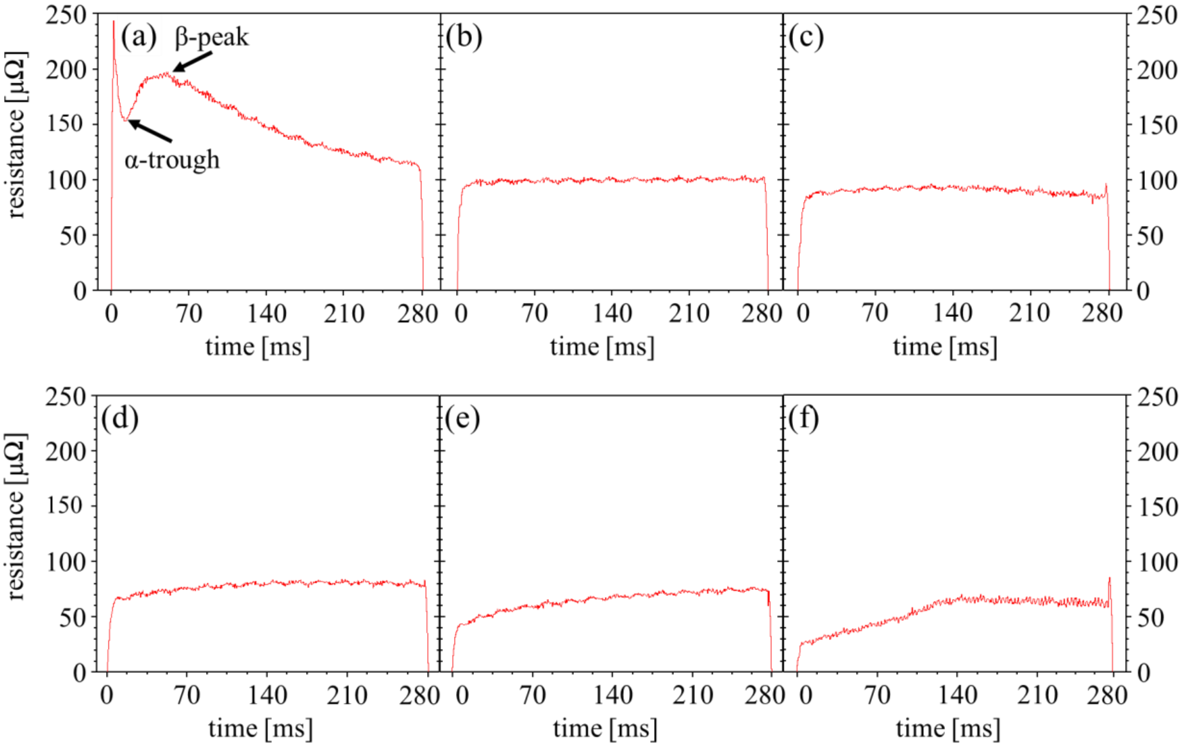

***Figure 17**: Dynamic resistance curves of the medium-Mn (a) single pulse and the second pulse after increasing cooling times of b) 20 ms, c) 50 ms, d) 100 ms, e) 200 ms and f) 500 ms (**Paper III**).*

On the one hand, an insufficient heat generation during the second pulse leads to the fact that the outer FZ does not recrystallize, which was visualized by means of the still elongated shape of the PAGs in **Paper III**. On the other hand, as illustrated by the EDX mapping in Figure 18a, the medium-Mn steel tends to form honeycomb-like manganese segregations in the outer FZ during solidification, which act as local brittle points and consequently contribute to the poor mechanical performance of the single pulse weld. If the temperature during the second pulse is high enough, as after a cooling time of 50 ms, manganese can diffuse and the segregations dissolve to a large extent, as illustrated in Figure 18b. In contrast, after a cooling time of 200 ms, the temperature during the second pulse is too low to enable excessive manganese diffusion and the segregations are still present, as shown in Figure 18c.

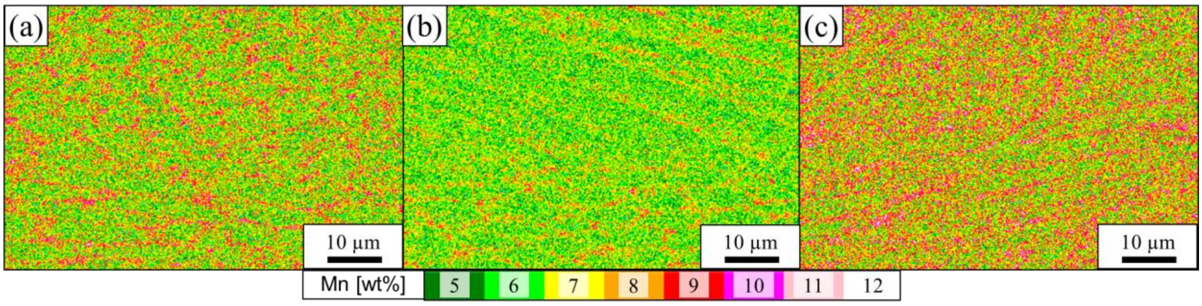

***Figure 18**: EDX mappings taken at the edge of the FZ of the medium-Mn a) single pulse weld and the double pulse welds with a cooling time of b) 50 ms and c) 200 ms (**Paper III**).*

Based on the findings published in **Paper III**, the influence of the cooling time between two pulses of the same current was also investigated for the TBF steel for different sheet thicknesses. From Figure 19 it can be concluded that the cooling time generally must be increased with increasing sheet thickness from 20 ms for a thickness of 1.00 mm, as shown in Figure 19a, to 100 ms for a thickness of 1.34 mm, as shown Figure 19b, and to 200 ms for a thickness of 1.6 mm, as shown in Figure 19c, in order to increase F_{max} significantly. This is due to the slower cooling of the FZ with increasing sheet thickness because of the greater distance to the water-cooled electrodes. Similar to the medium-Mn steel, the failure mode does not depend on the cooling time. Thinner sheets generally offer a higher pullout ratio.

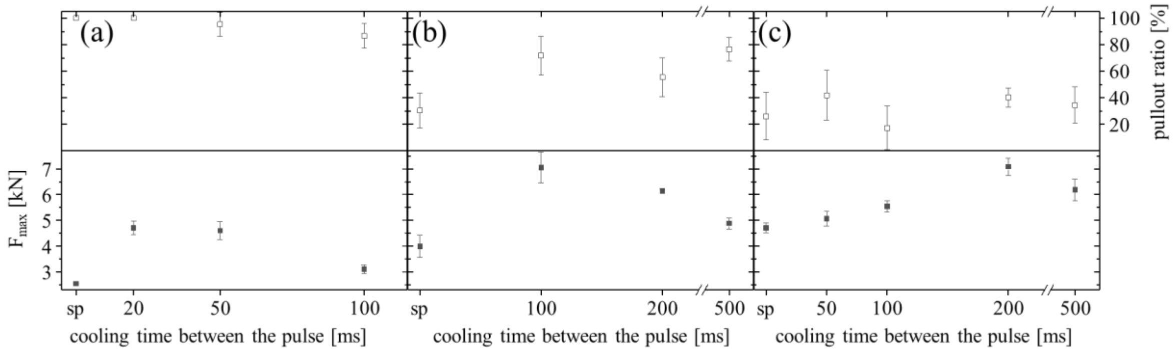

***Figure 19**: Results of CTS tests for recrystallization pulse welds as a function of the cooling time between the pulses for TBF sheets with a thickness of a) 1.00 mm, b) 1.34 mm and c) 1.60 mm.*

3.4.5. Microstructure and local mechanical properties of the HAZ of the medium-Mn steel

The results of **Paper III** demonstrate how certain microstructural features in the FZ correlate with the inferior mechanical properties of medium-Mn steel welds and how these can be modified towards an improved mechanical performance. However, during the welding process, not only the FZ but also the HAZ undergoes significant microstructural changes, which effect the mechanical performance of the welds. The EDX results in **Paper III** already suggested that the diffusivity of the substitutionally dissolved manganese strongly depends on the prevailing temperature. It was consequently assumed that the austenite stability varies strongly over the HAZ, which may result in highly position-dependent mechanical properties. Therefore, in **Paper IV**, the entire HAZ of the single pulse welded medium-Mn steel was investigated with regard to its microstructure and the local mechanical properties as a function of the distance to the FZ. The knowledge gained is intended to serve as basis for future targeted HAZ design in order to improve the mechanical properties of the welds, for example by post-weld heat treatments. In contrast to existing studies, which simulated the thermal cycle during RSW by means of a FE software, namely SORPAS by SWANTEC, the approach presented in **Paper IV** allows the reconstruction of the temperature profile in a very small step size without relying on FE-simulations. To accomplish this, sheets were rapidly heated with a rate of up to 1300 K/s to various peak temperatures ranging from 500 °C to 1300 °C in steps of 50 °C and subsequently quenched using a water spray in order to physically simulate the temperature profile in the HAZ during RSW. The mechanical properties were determined by tensile tests and the austenite fraction was measured magnetically on these physically simulated HAZ samples. Finally, the various physically simulated HAZ samples were assigned to their positions in the HAZ by comparing their microstructure characterized with EBSD, SEM and EDX measurements, as well as their hardness. The methodology of the microstructural characterizations carried out in **Paper IV** is described below on the example of the BM.

As can be seen in the uncleaned EBSD phase map in Figure 20a, the austenite (face centered cubic, fcc) is finely dispersed in the ferritic (body centered cubic, bcc) matrix of the medium-Mn BM and therefore a very small step size of 25 nm was chosen for the scans. The data points with a confidence index (CI) below 0.1 are shown in black and were disregarded. They represent either grain boundaries or austenite that is too fine to be reliably indexed. Therefore, the quantification by EBSD leads to a systematic underestimation of the austenite content, which is why this method was only used for the qualitative comparison of the microstructures and the exact quantified austenite fraction was determined magnetically on the physically simulated HAZ samples. In order to retrieve the austenitic regions for the determination of the manganese content with EDX, its higher packing density compared to ferrite and the resulting brighter appearance in the backscattered electron (BSE) contrast was utilized. As shown in Figure 20b, the large globularly shaped austenitic regions (spots 1-4) have a significantly higher manganese content compared to the small lath-like austenite at spot 5. This is because the relatively large EDX spot always excites a certain amount of the surrounding ferrite as well, which is depleted in manganese. In the secondary electron (SE) contrast SEM image of the corresponding Nital etched cross section in Figure 20c, it is shown that the austenitic areas were attacked more severely by the etchant due to the higher content of the less noble manganese. However, the areas where EDX was conducted were protected by carbon contaminations during the EDX measurements.

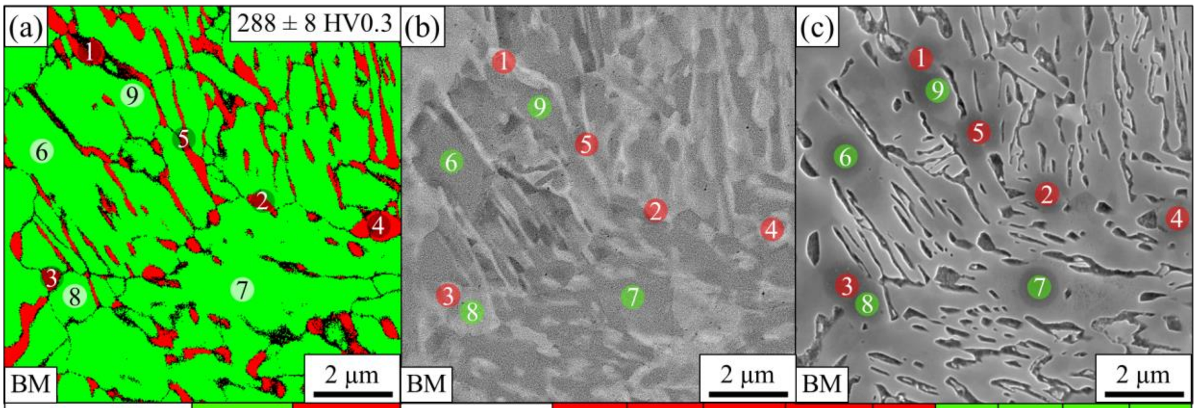

phase	bcc	fcc	spot	1	2	3	4	5	6	7	8	9
total fraction	0.800	0.116	Mn [wt%]	11.5	11.8	12.5	13.4	9.7	6.1	6.5	5.5	5.1

***Figure 20**: Methodology of the microstructural investigations in **Paper IV** on the example of the medium-Mn BM. a) EBSD phase map, b) corresponding BSE image and c) corresponding SE image after Nital etching. The numbered circles indicate the points where the manganese content was determined with EDX (**Paper IV**).*

Using the methodology described above, the microstructure of the entire HAZ (Positions 1-8) and the physically simulated HAZ samples were characterized in **Paper IV**. The qualitative comparison of the microstructures in combination with detailed hardness measurements allowed the reconstruction of the temperature profile of the HAZ during RSW, as shown in Figure 21.

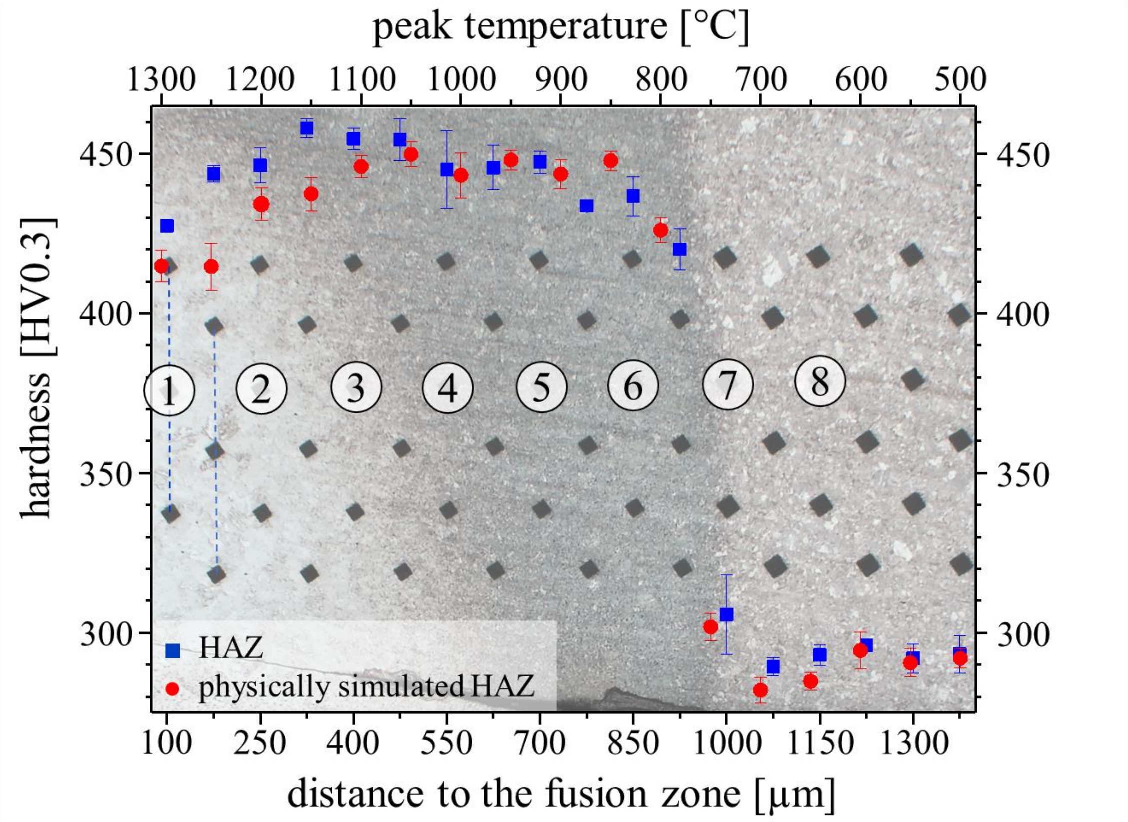

***Figure 21**: Assignment of the peak temperature of the physically simulated samples to the HAZ, which is shown in the background, by means of the EBSD phase maps and the hardness profiles. The blue squares represent the hardness of the HAZ as a function of the distance to the FZ (lower axis). The red circles represent the hardness of the physically simulated HAZ as a function of the peak temperature (upper axis) (**Paper IV**).*

After determination of the temperature profile, the austenite content and local mechanical properties were determined for the physically simulated HAZ samples, as illustrated in Figure 22. Peak temperatures above 1150 °C, which prevail just before position 3, lead to an almost fully martensitic microstructure due to the enabled manganese diffusion, as proven by SEM images, EBSD and EDX measurements in **Paper IV**. Because of grain refinement, the yield strength (YS) and the tensile strength (TS) increase continuously with decreasing peak temperature, while the total elongation (A_{15}) remains relatively constant. Below a peak temperature of 1100 °C, which is associated with the change of the microstructure near position 3, the temperature is no longer high enough to completely homogenize the manganese enrichment and the austenite content increases almost linearly with decreasing temperature, which results in a continuous increase of the total elongation. YS and TS decrease continuously and are defined by the interplay of the strength increasing mechanism of grain refinement and the strength reducing effect of the declining martensite phase fraction. The change of the microstructure near position 7 represents the extremely narrow ICHAZ, which sees a peak temperature of approximately 750 °C during RSW and whose microstructure consists of ferrite, austenite and a small fraction of martensite. Lower temperatures have no significant influence on the microstructure and mechanical properties.

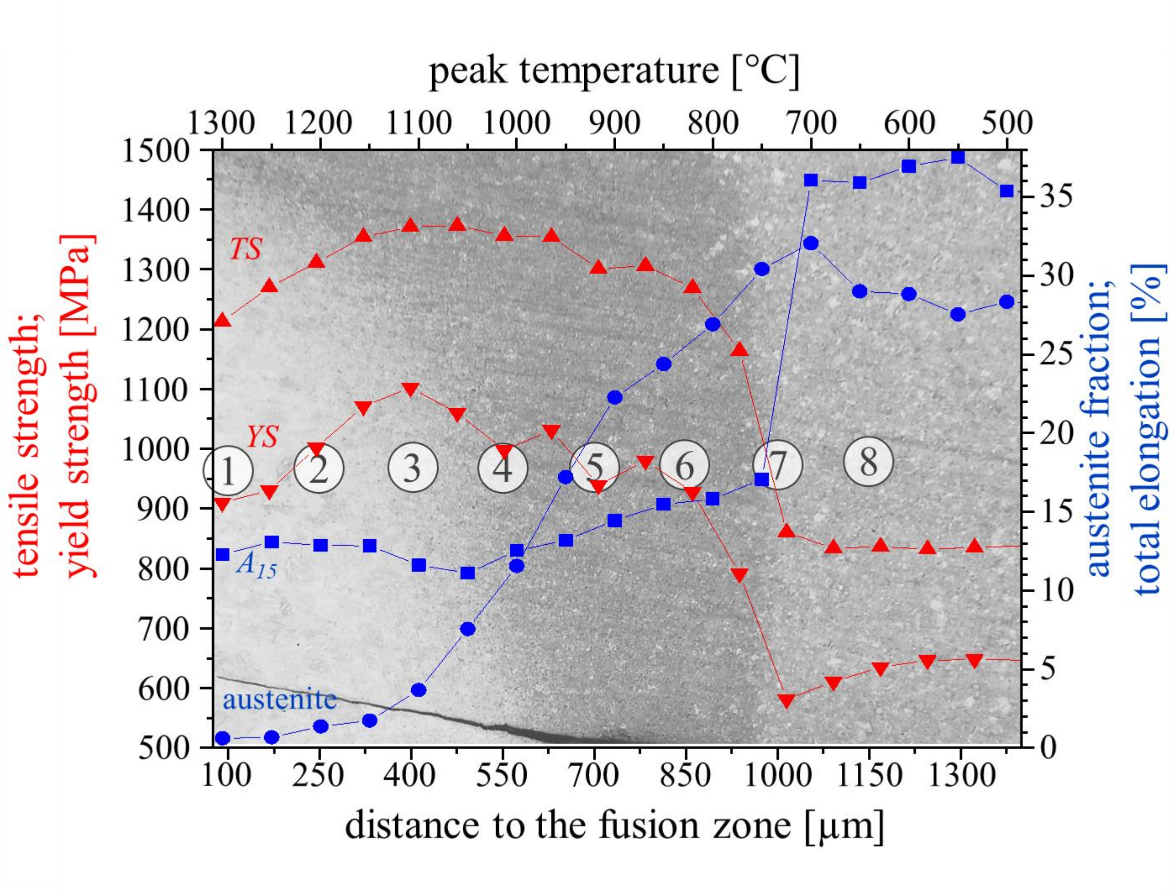

***Figure 22**: Austenite fraction (blue dots), tensile strength TS (upwards directed red triangle), yield strength YS (downwards directed red triangle) and total elongation A_{15} (blue squares) of the physically simulated HAZ. The microstructure of the HAZ after Nital etching is shown in the background (**Paper IV**).*

From the results of **Paper IV**, it can be concluded that the austenite in medium-Mn steels has a higher thermal stability compared to other third generation AHSS, which rely on the stabilization of the austenite by carbon. Its stability strongly depends on the temperature and consequently the microstructure and local mechanical properties of the HAZ change significantly with increasing distance to the FZ. This illustrates the importance of the investigations with a small step size. The presented approach allows the reconstruction of the temperature profile in the HAZ and the results are intended to support future targeted HAZ design.

4. Outlook and open questions

In the present thesis, the spot weldability of third generation AHSS was investigated on the example of a TBF and a medium-Mn steel. The characterization of the FZ and HAZ gave a deep insight into the material response to the extremely high heating and cooling rates during the RSW process. Additionally, correlations between the presence of certain microstructural features and the mechanical performance have been established. Based on these findings, it was possible to modify the microstructure and enable improved mechanical properties by means of in-process heat treatments via double pulsing. However, there are still some related topics that are worth investigating and have not been addressed so far.

First of all, the influence of phosphorus segregations in the outer FZ should be investigated in more detail. In the literature, the improved mechanical properties due to double pulsing are partly attributed to the dissolution of grain boundary segregations [97,98], which was demonstrated by electron probe microanalyzer (EPMA) measurements. For this reason, the outer FZ of the TBF steel was also examined by EPMA measurements in the course of this work, but without detecting phosphorus segregations in significant quantities. On the one hand, this may be due to the extremely low level of phosphorus in the TBF steel. On the other hand, these segregations may be too small to be detected by the conventional EPMA system used. For this purpose, high-resolution atom probe tomography investigations at the grain boundaries of the outer FZ would be useful to clarify whether or not phosphorus segregates there.

The reasons why the failure mode of medium-Mn steel spot welds is not significantly improved by double pulsing and why it does not correlate with the cooling time would be worth investigating. In this context, detailed EBSD measurements regarding the distribution of the high angle grain boundaries similar to the TBF steel are promising.

It would also be interesting to observe the crack propagation during the CTS test to clarify where crack deflection actually takes place and which microstructural features promote rapid crack propagation. The foundation for this project has already been laid. In cooperation with the University of Sydney, a devise for in-situ tensile testing in the SEM was developed, which, in combination with repeated EBSD scans, allows the observation of crack initiation and propagation. This approach enables valuable insights into the damage evolution and can support the improvement of the failure mode.

The principle of using resistance curves to set the ideal cooling time for double pulsing is very promising regarding future process control in production and therefore needs to be pursued on various steels with varying sheet thicknesses and coatings.

Likewise, the concept of physically simulating the different regions of the HAZ should be pursued further. The knowledge gained could be used as a basis to modify not only the microstructure of the FZ but also of the HAZ by means of double pulsing in order to improve the mechanical performance of third generation AHSS.

In summary, as shown in this thesis, the poor mechanical properties of third generation can be counteracted by innovative in-process heat treatments that modify the unfavorable microstructural components. Due to its short cooling time, especially the recrystallization pulse concept has the potential to be implemented for the RSW of third generation AHSS.

5. Novel features

This work contains some novel findings that are believed to make a significant contribution to the field of research. The most important findings are listed below:

- It is shown that, in addition to the well documented visualization of the solidification structure of the FZ, picric acid is suitable for investigating the UCHAZ of double pulse welds in terms of the degree of tempering and, especially, regarding the size and shape of the PAGs. This simple etching method could therefore replace time-consuming EBSD measurements.
- Both the softening of the FZ as well as the modification of the cast-like structure in the outer FZ are capable of significantly improving the mechanical performance of TBF steel spot welds. With the temper pulse concept, it is possible to more than double F_{max} during the CTS test, but with the drawback of a much longer process time. By means of the recrystallization pulse concept, F_{max} is also almost doubled, but at much shorter process times. This approach is therefore highly recommended to be implement into the production line. However, as the sheet thickness increases also the cooling time between the pulses must be extended.
- In medium-Mn steels, manganese segregations in the outer FZ are mainly responsible for the inferior mechanical properties of the welds. These can also be tackled by means of a recrystallization pulse, whereby a doubling of F_{max} is achieved after short cooling times.
- The established correlation between the increased fraction of high angle grain boundaries near 60 ° after higher heat inputs, which promote crack deflection and consequently lead to an enhanced failure mode, is noteworthy.
- The interpretation of the resistance curves allows the assessment of the heat input during the second pulse, which can serve as basis for future process control.
- The thermal stability of the austenite of a medium-Mn steel and the resulting local mechanical properties of the HAZ were determined in dependence of the distance to the FZ. These results, and especially the presented approach using a thermal simulator to replicate the microstructure of the HAZ, are intended to serve as a foundation for future targeted HAZ design.

6. References

[1] J. Bloomfield, F. Steward, The politics of the green new deal, The Political Quarterly 91 (2020) 770–779.

[2] T. Haas, H. Sander, Decarbonizing transport in the European Union: Emission performance standards and the perspectives for a European green deal, Sustainability 12 (2020) 8381.

[3] K. Kawajiri, M. Kobayashi, K. Sakamoto, Lightweight materials equal lightweight greenhouse gas emissions?: a historical analysis of greenhouse gases of vehicle material substitution, Journal of Cleaner Production 253 (2020) 119805.

[4] O. Bouaziz, H. Zurob, M. Huang, Driving force and logic of development of advanced high strength steels for automotive applications, steel research international 84 (2013) 937-947.

[5] N. Fonstein, Advanced high strength sheet steels: physical metallurgy, design, processing and properties, Springer International Publishing, New York, 2015.

[6] J. Speer, D.K. Matlock, B.C. De Cooman, J.G. Schroth, Carbon partitioning into austenite after martensite transformation, Acta Materialia 51 (2003) 2611–2622.

[7] K.I. Sugimoto, T. Iida, J. Sakaguchi, T. Kashima, Retained austenite characteristics and tensile properties in a TRIP type bainitic sheet steel, ISIJ International 40 (2000) 902–908.

[8] M.J. Merwin, Low-carbon manganese TRIP steels, Materials Science Forum 539-543 (2007) 4327–4332.

[9] M. Pouranvari, S.P.H. Marashi, Critical review of automotive steels spot welding: process, structure and properties, Science and Technology of Welding and Joining 18 (2013) 361–403.

[10] M. Kimchi, D.H. Phillips, Resistance spot welding: fundamentals and applications for the automotive industry, Synthesis Lectures on Mechanical Engineering 1 (2017) i-115.

[11] B.C. De Cooman, Y. Estrin, S.K. Kim, Twinning-induced plasticity (TWIP) steels, Acta Materialia 142 (2018) 283–362.

[12] Steels for cold stamping – Fortiform®, https://automotive.arcelormittal.com/products/flat/third_gen_AHSS/fortiform, May 2021.

[13] ahss high-ductility, https://www.voestalpine.com/stahl/Marken/ahss-high-ductility, May 2021.

[14] H. Karbasian, A.E. Tekkaya, A review on hot stamping, Journal of Materials Processing Technology 210 (2010) 2103–2118.

[15] V.F. Zackay, E.R. Parker, D. Fahr, R. Busch, The enhancement of ductility in high-strength steels, ASM Trans Quart 60 (1967) 252–259.

[16] P. Jacques, Q. Furnémont, A. Mertens, F. Delannay, On the sources of work hardening in multiphase steels assisted by transformation-induced plasticity, Philosophical Magazine A 81 (2001) 1789–1812.

[17] M. Soleimani, A. Kalhor, H. Mirzadeh, Transformation-induced plasticity (TRIP) in advanced steels: A review, Materials Science and Engineering: A 795 (2020) 140023.

[18] S. Ebner, C. Suppan, R. Schnitzer, C. Hofer, Microstructure and mechanical properties of a low C steel subjected to bainitic or quenching and partitioning heat treatments, Materials Science and Engineering: A 735 (2018) 1–9.

[19] C. Hofer, H. Leitner, F. Winkelhofer, H. Clemens, S. Primig, Structural characterization of carbide-free bainite in a Fe–0.2C–1.5Si–2.5Mn steel, Materials Characterization 102 (2015) 85–91.

[20] K. Steineder, D. Krizan, R. Schneider, C. Béal, C. Sommitsch, On the microstructural characteristics influencing the yielding behavior of ultra-fine grained medium-Mn steels, Acta Materialia 139 (2017) 39–50.

[21] K.I. Sugimoto, T. Hojo, J. Kobayashi, Critical assessment 29: TRIP-aided bainitic ferrite steels, Materials Science and Technology 33 (2017) 2005–2009.

[22] B.C. De Cooman, Structure–properties relationship in TRIP steels containing carbide-free bainite, Current Opinion in Solid State and Materials Science 8 (2004) 285–303.

[23] C. Hofer, V. Bliznuk, A. Verdiere, R. Petrov, F. Winkelhofer, H. Clemens et al., High-resolution characterization of the martensite-austenite constituent in a carbide-free bainitic steel, Materials Characterization 144 (2018) 182–190.

[24] C. Hofer, S. Primig, H. Clemens, F. Winkelhofer, R. Schnitzer, Influence of heat treatment on microstructure stability and mechanical properties of a carbide-free bainitic steel, Advanced Engineering Materials 19 (2017) 1600658.

[25] C. Hofer, F. Winkelhofer, H. Clemens, S. Primig, Morphology change of retained austenite during austempering of carbide-free bainitic steel, Materials Science and Engineering: A 664 (2016) 236–246.

[26] F.G. Caballero, C. Garcia-Mateo, J. Chao, M.J. Santofimia, C. Capdevila, C.G. de Andres, Effects of morphology and stability of retained austenite on the ductility of TRIP-aided bainitic steels, ISIJ International 48 (2008) 1256–1262.

[27] K.I. Sugimoto, Usui, N., Kobayashi, M., S.I. Hashimoto, Effects of volume fraction and stability of retained austenite on ductility of TRIP-aided dual-phase steels, ISIJ International 32 (1992) 1311–1318.

[28] K. Sung-Joon, C.G. Lee, I. Choi, S. Lee, Effects of heat treatment and alloying elements on the microstructures and mechanical properties of 0.15 Wt Pct C transmation-induced plasticity-aided cold-rolled steel sheets, Metallurgical and Materials Transactions A 32 (2001) 505–514.

[29] R.L. Miller, Ultrafine-grained microstructures and mechanical properties of alloy steels, Metallurgical Transactions B 3 (1972) 905–912.

[30] H. Aydin, E. Essadiqi, I.-H. Jung, S. Yue, Development of 3rd generation AHSS with medium Mn content alloying compositions, Materials Science and Engineering: A 564 (2013) 501–508.

[31] Y.-K. Lee, J. Han, Current opinion in medium manganese steel, Materials Science and Technology 31 (2015) 843–856.

[32] S. Lee, S.-J. Lee, S. Santhosh Kumar, K. Lee, B.C. De Cooman, Localized deformation in multiphase, ultra-fine-grained 6 pct Mn transformation-induced plasticity steel, Metallurgical and Materials Transactions A 42 (2011) 3638–3651.

[33] S. Lee, B.C. De Cooman, On the selection of the optimal intercritical annealing temperature for medium Mn TRIP steel, Metallurgical and Materials Transactions A 44 (2013) 5018–5024.

[34] J. Hu, L.-X. Du, W. Xu, J.-H. Zhai, Y. Dong, Y.-J. Liu et al., Ensuring combination of strength, ductility and toughness in medium-manganese steel through optimization of nano-scale metastable austenite, Materials Characterization 136 (2018) 20–28.

[35] J. Han, Y.-K. Lee, The effects of the heating rate on the reverse transformation mechanism and the phase stability of reverted austenite in medium Mn steels, Acta Materialia 67 (2014) 354–361.

[36] Z.H. Cai, H. Ding, R.D.K. Misra, Z.Y. Ying, Austenite stability and deformation behavior in a cold-rolled transformation-induced plasticity steel with medium manganese content, Acta Materialia 84 (2015) 229–236.

[37] A.M. Al-Mukhtar, Review of resistance spot welding sheets: processes and failure mode, Advanced Engineering Forum 17 (2016) 31–57.

[38] S.M. Manladan, I. Abdullahi, M.F. Hamza, A review on the application of resistance spot welding of automotive sheets, Journal of Engineering and Technology 10 (2015) 20–37.

[39] N.J. Den Uijl, S. Smith, Resistance spot welding of advanced high strength steels for the automotive industry, in Proc. 4th International Seminar on Advances in Resistance Welding, Wels, Austria (2006) 30-60.

[40] N.T. Williams, J.D. Parker, Review of resistance spot welding of steel sheets Part 1 Modelling and control of weld nugget formation, International Materials Reviews 49 (2004) 45–75.

[41] D.W. Dickinson, J.E. Franklin, A. Stanya, Characterization of spot welding behavior by dynamic electrical parameter monitoring, Welding Journal 59 (1980) 170–176.

[42] X. Han, C. DiGiovanni, J. McDermid, E. Biro, N.Y. Zhou, Effect of internal oxidation on the weldability of CMnSi steels, Welding in the World 63 (2019) 1633–1639.

[43] S.-F. Ling, L.-X. Wan, Y.-R. Wong, D.-N. Li, Input electrical impedance as quality monitoring signature for characterizing resistance spot welding, NDT & E International 43 (2010) 200–205.

[44] Y. Luo, W. Rui, X. Xie, Y. Zhu, Study on the nugget growth in single-phase AC resistance spot welding based on the calculation of dynamic resistance, Journal of Materials Processing Technology 229 (2016) 492–500.

[45] American Welding Society, Recommended practices for test methods for evaluating the resistance spot welding behavior of automotive sheet steel materials (2002)

[46] E.W. Kim, T.W. Eagar, Parametric analysis of resistance spot welding lobe curve, SAE transactions (1988) 107–118.

[47] Y.J. Chao, Failure mode of spot weld: interfacial versus pullout, Science and Technology of Welding and Joining 8 (2003) 133–137.

[48] M. Pouranvari, Susceptibility to interfacial failure mode in similar and dissimilar resistance spot welds of DP600 dual phase steel and low carbon steel during cross-tension and tensile-shear loading conditions, Materials Science and Engineering: A 546 (2012) 129–138.

[49] M. Pouranvari, S.P.H. Marashi, Failure mode transition in AHSS resistance spot welds. Part I. Controlling factors, Materials Science and Engineering: A 528 (2011) 8337–8343.

[50] M.I. Khan, M.L. Kuntz, Y. Zhou, Effects of weld microstructure on static and impact performance of resistance spot welded joints in advanced high strength steels, Science and Technology of Welding and Joining 13 (2008) 294–304.

[51] H. Zhang, X. Qiu, F. Xing, J. Bai, J. Chen, Failure analysis of dissimilar thickness resistance spot welded joints in dual-phase steels during tensile shear test, Materials & Design 55 (2014) 366–372.

[52] X. Sun, E.V. Stephens, M.A. Khaleel, Effects of fusion zone size and failure mode on peak load and energy absorption of advanced high-strength steel spot welds, Welding Journal-New York 86 (2007) 18.

[53] S. Dancette, D. Fabrègue, V. Massardier, J. Merlin, T. Dupuy, M. Bouzekri, Experimental and modeling investigation of the failure resistance of advanced high strength steels spot welds, Engineering Fracture Mechanics 78 (2011) 2259–2272.

[54] M. Pouranvari, H.R. Asgari, S.M. Mosavizadch, P.H. Marashi, M. Goodarzi, Effect of weld nugget size on overload failure mode of resistance spot welds, Science and Technology of Welding and Joining 12 (2013) 217–225.

[55] M. Pouranvari, S.P.H. Marashi, D.S. Safanama, Failure mode transition in AHSS resistance spot welds. Part II: experimental investigation and model validation, Materials Science and Engineering: A 528 (2011) 8344–8352.

[56] N.J. Den Uijl, Resistance spot welding of advanced high strength steels, Dissertation, Technische Universiteit Delft, 2015.

[57] N.J. Den Uijl, H. Nishibata, S. Smith, T. Okada, T. van der Veldt, M. Uchihara et al., Prediction of post weld hardness of advanced high strength steels for automotive application using a dedicated carbon equivalent number, Welding in the World 52 (2008) 18–29.

[58] L.E. Svensson, Prediction of hardness of spot welds in steels, Welding in the World 48 (2004) 31–35.

[59] C. Ma, D.L. Chen, S.D. Bhole, G. Boudreau, A. Lee, E. Biro, Microstructure and fracture characteristics of spot-welded DP600 steel, Materials Science and Engineering: A 485 (2008) 334–346.

[60] S.S. Nayak, V.H. Baltazar Hernandez, Y. Okita, Y. Zhou, Microstructure–hardness relationship in the fusion zone of TRIP steel welds, Materials Science and Engineering: A 551 (2012) 73–81.

[61] V.H. Vargas, I. Mejía, V.H. Baltazar Hernandez, C. Maldonado, Characterization of resistance spot welded transformation induced plasticity (TRIP) steels with different silicon and carbon contents, Journal of Manufacturing Processes 32 (2018) 307–317.

[62] M. Pouranvari, Failure mode transition in similar and dissimilar resistance spot welds of HSLA and low carbon steels, Canadian Metallurgical Quarterly 51 (2012) 67–74.

[63] M. Pouranvari, S.P.H. Marashi, Key factors influencing mechanical performance of dual phase steel resistance spot welds, Science and Technology of Welding and Joining 15 (2013) 149–155.

[64] M. Pouranvari, S.P.H. Marashi, Failure mode transition in AISI 304 resistance spot welds, Welding Journal 91 (2012) 303–309.

[65] M. Amirthalingam, E.M. van der Aa, C. Kwakernaak, M.J.M. Hermans, I.M. Richardson, Elemental segregation during resistance spot welding of boron containing advanced high strength steels, Welding in the World 59 (2015) 743–755.

[66] P. Eftekharimilani, E.M. van der Aa, M.J.M. Hermans, I.M. Richardson, The microstructural evolution and elemental distribution of a 3rd generation 1 GPa advanced high strength steel during double pulse resistance spot welding, Welding in the World 61 (2017) 691–701.

[67] S. Dancette, V. Massardier-Jourdan, D. Fabrègue, J. Merlin, T. Dupuy, M. Bouzekri, HAZ microstructures and local mechanical properties of high strength steels resistance spot welds, ISIJ International 51 (2011) 99–107.

[68] H. Rezayat, H. Ghassemi-Armaki, S.P. Bhat, S. Sriram, S.S. Babu, Constitutive properties and plastic instabilities in the heat-affected zones of advanced high-strength steel spot welds, Journal of Materials Science 54 (2019) 5825–5843.

[69] G. Park, K. Kim, S. Uhm, C. Lee, A comparison of cross-tension properties and fracture behavior between similar and dissimilar resistance spot-weldments in medium-Mn TRIP steel, Materials Science and Engineering: A 752 (2019) 206–216.

[70] G. Park, S. Uhm, C. Lee, Effects of in-situ post-weld heat treatment on the microstructure and mechanical properties of the coarse-grained heat-affected zone in a resistance spot weld in medium Mn TRIP steel, Materials Science and Engineering: A 788 (2020) 139477.

[71] M. Pouranvari, S. Sobhani, F. Goodarzi, Resistance spot welding of MS1200 martensitic advanced high strength steel: microstructure-properties relationship, Journal of Manufacturing Processes 31 (2018) 867–874.

[72] M. Tamizi, M. Pouranvari, M. Movahedi, Welding metallurgy of martensitic advanced high strength steels during resistance spot welding, Science and Technology of Welding and Joining 22 (2017) 327–335.

[73] G. Park, K. Kim, S. Uhm, C. Lee, Remarkable improvement in resistance spot weldability of medium-Mn TRIP steel by paint-baking heat treatment, Materials Science and Engineering: A 766 (2019) 138401.

[74] A. Chabok, E. van der Aa, J.T.M. de Hosson, Y.T. Pei, Mechanical behavior and failure mechanism of resistance spot welded DP1000 dual phase steel, Materials & Design 124 (2017) 171–182.

[75] Q. Jia, L. Liu, W. Guo, Y. Peng, G. Zou, Z. Tian et al., Microstructure and tensile-shear properties of resistance spot-welded medium Mn steel, Metals 8 (2018) 48.

[76] Y. Lu, A. Peer, T. Abke, M. Kimchi, W. Zhang, Subcritical heat affected zone softening in hot-stamped boron steel during resistance spot welding, Materials & Design 155 (2018) 170–184.

[77] E. Biro, J.R. McDermid, J.D. Embury, Y. Zhou, Softening kinetics in the subcritical heat-affected zone of dual-phase steel welds, Metallurgical and Materials Transactions A 41 (2010) 2348–2356.

[78] V.H. Baltazar Hernandez, S.K. Panda, M.L. Kuntz, Y. Zhou, Nanoindentation and microstructure analysis of resistance spot welded dual phase steel, Materials Letters 64 (2010) 207–210.

[79] V.H. Baltazar Hernandez, S.S. Nayak, Y. Zhou, Tempering of martensite in dual-phase steels and its effects on softening behavior, Metallurgical and Materials Transactions A 42 (2011) 3115–3129.

[80] M. Pouranvari, Effect of resistance spot welding parameters on the HAZ softening of DP980 ferrite-martensite dual phase steel welds, World Applied Sciences Journal 15 (2011) 1454–1458.

[81] F. Nikoosohbat, S. Kheirandish, M. Goodarzi, M. Pouranvari, S.P.H. Marashi, Microstructure and failure behaviour of resistance spot welded DP980 dual phase steel, Materials Science and Technology 26 (2013) 738–744.

[82] J.J. Guzman-Aguilera, C.J. Martinez-Gonzalez, V.H. Baltazar Hernandez, S. Basak, S.K. Panda, M.H. Razmpoosh et al., Influence of SC-HAZ microstructure on the mechanical behavior of Si-TRIP steel welds, Materials Science and Engineering: A 718 (2018) 216–227.

[83] M. Tamizi, M. Pouranvari, M. Movahedi, The role of HAZ softening on cross-tension mechanical performance of martensitic advanced high strength steel resistance spot welds, Metallurgical and Materials Transactions A 52 (2021) 655–667.

[84] W.L. Chuko, J.E. Gould, Development of appropriate resistance spot welding practice for transformation-hardened steels, Welding Journal 81 (2002) 1–7.

[85] H. Aghajani, M. Pouranvari, Influence of in situ thermal processing strategies on the weldability of martensitic stainless steel resistance spot welds: effect of second pulse current on the weld microstructure and mechanical properties, Metallurgical and Materials Transactions A 50 (2019) 5191–5209.

[86] M. Mimer, L.E. Svensson, R. Johansson, Process adjustments to improve fracture behaviour in resistance spot welds of EHSS and UHSS, Welding in the World 48 (2004) 14–18.

[87] A.R. Jahandideh, M. Hamedi, S.A. Mansourzadeh, A. Rahi, An experimental study on effects of post-heating parameters on resistance spot welding of SAPH440 steel, Science and Technology of Welding and Joining 16 (2011) 669–675.

[88] S. Sajjadi-Nikoo, M. Pouranvari, A. Abedi, A.A. Ghaderi, In situ postweld heat treatment of transformation induced plasticity steel resistance spot welds, Science and Technology of Welding and Joining 23 (2018) 71–78.

[89] I.A. Soomro, S.R. Pedapati, M. Awang, Optimization of postweld tempering pulse parameters for maximum load bearing and failure energy absorption in dual phase (DP590) steel resistance spot welds, Materials Science and Engineering: A 803 (2021) 140713.

[90] F. Nikoosohbat, S. Kheirandish, M. Goodarzi, M. Pouranvari, Effect of tempering on the microstructure and mechanical properties of resistance-spot-welded DP980 dual-phase steel, Materiali in tehnologije 49 (2015) 133–138.

[91] B. Zhao, Y. Wang, K. Ding, G. Wu, T. Wei, H. Pan et al., Enhanced cross-tension property of the resistance spot welded medium-Mn steel by in situ microstructure tailoring, International Journal of Steel Structures 21 (2021) 666–675.

[92] B. Zhao, Y. Wang, K. Ding, G. Wu, T. Wei, H. Pan et al., Role of intercritical annealing in enhancing the cross-tension property of resistance spot-welded medium Mn Steel, Journal of Materials Engineering and Performance 30 (2021) 1259–1269.

[93] V.H. Baltazar Hernandez, Y. Okita, Y. Zhou, Second pulse current in resistance spot welded TRIP steel-effects on the microstructure and mechanical behavior, impulse 91 (2012) 278–285.

[94] C. Sawanishi, T. Ogura, K. Taniguchi, R. Ikeda, K. Oi, K. Yasuda et al., Mechanical properties and microstructures of resistance spot welded DP980 steel joints using pulsed current pattern, Science and Technology of Welding and Joining 19 (2013) 52–59.

[95] A. Chabok, E. van der Aa, I. Basu, J. de Hosson, Y. Pei, Effect of pulse scheme on the microstructural evolution, residual stress state and mechanical performance of resistance spot welded DP1000-GI steel, Science and Technology of Welding and Joining 23 (2018) 649–658.

[96] P. Eftekharimilani, E.M. van der Aa, M.J.M. Hermans, I.M. Richardson, Microstructural characterisation of double pulse resistance spot welded advanced high strength steel, Science and Technology of Welding and Joining 22 (2017) 545–554.

[97] X.D. Liu, Y.B. Xu, R.D.K. Misra, F. Peng, Y. Wang, Y.B. Du, Mechanical properties in double pulse resistance spot welding of Q&P 980 steel, Journal of Materials Processing Technology 263 (2019) 186–197.

[98] E.M. van der Aa, M. Amirthalingam, J. Winter, D.N. Hanlon, M.J.M. Hermans, M. Rijnders et al, Improved resistance spot weldability of 3rd generation AHSS for automotive applications, in 11th International Seminar on Numerical Analysis of Weldability, Graz, Austria, 2015.

[99] C. Cayron, ARPGE: a computer program to automatically reconstruct the parent grains from electron backscatter diffraction data, Journal of applied crystallography 40 (2007) 1183–1188.

Part B

Paper I

M. Stadler, M. Gruber, R. Schnitzer, C. Hofer

Microstructural characterization of a double pulse resistance spot welded 1200 MPa TBF steel

Welding in the World 64 (2020) 335-343

Welding in the World (2020) 64:335–343
https://doi.org/10.1007/s40194-019-00835-9

RESEARCH PAPER

Microstructural characterization of a double pulse resistance spot welded 1200 MPa TBF steel

Manfred Stadler[1] · **Martin Gruber**[2] · **Ronald Schnitzer**[1] · **Christina Hofer**[1]

Received: 12 September 2019 / Accepted: 27 November 2019 / Published online: 8 December 2019

Abstract

In the automotive industry resistance, spot welding is the dominant technology in sheet metal joining of advanced high strength steels (AHSS). In order to improve the mechanical performance of AHSS welds, in-process tempering via a second pulse is a possible approach. In this work, two different double pulse welding schemes were applied to a 1200 MPa transformation-induced plasticity (TRIP)-aided bainitic ferrite (TBF) steel. The different microstructures in the welds were characterized via light optical and scanning electron microscopy. Additionally, hardness mappings with several hundred indents were performed. It is shown that the second pulse, following a low first pulse which is high enough to produce a weld nugget that fulfills the quality criterion of a minimum spot weld diameter of $4^*\sqrt{t}$, leads to partial reaustenitization and consequently to a ferritic/martensitic microstructure after final quenching. Hardness mappings revealed that this inner FZ is harder than the surrounding FZ consisting of tempered martensite. In contrast, if the highest current without splashing is chosen for the first pulse, the same second pulse does not reaustenitize the FZ but only temper the martensite.

Keywords Resistance spot welding · Double pulse · AHSS · TRIP-aided bainitic ferrite · TBF

1 Introduction

In order to reduce the car body weight and subsequently minimize the amount of emissions, further development of advanced high strength steels (AHSS) for automotive applications is required. Steel grades from the third generation of AHSS combine high strength and ductility at lower costs than grades of the second generation [1]. Transformation-induced plasticity (TRIP)-aided bainitic ferrite (TBF) steels are promising representatives of this generation. Their superior mechanical properties are achieved by a multiphase microstructure containing bainite and a sufficient amount of retained austenite stabilized by carbon enrichment during an isothermal holding step [2–4].

Due to the combination of high operation speed and its suitability for automation, resistance spot welding (RSW) is the dominant technology in sheet metal joining in the automotive industry [5]. The body in white of modern cars contains thousands of spot welds. Therefore, the mechanical performance and failure mode of the welds play an important role in terms of crashworthiness and consequently passenger safety. However, the relatively high content of alloying elements in AHSS compared to mild steels and the rapid cooling during RSW lead to a hard and brittle martensitic microstructure of the weld, and therefore the weldability of these steels is restricted [5–7]. Generally, AHSS resistance spot welds can be divided into the zones schematically illustrated in Fig. 1. The fusion zone (FZ) melts completely, is usually fully martensitic, and has a cast-like structure. In contrary, the heat-affected zone (HAZ) does not melt but is influenced by the heat input. It can be subdivided into the zones described in the following. The upper critical heat-affected zone (UCHAZ) consists of the $UCHAZ_I$, also called coarse grain zone, and the $UCHAZ_{II}$, also called fine grain zone. In the UCHAZ, the material is heated over the A_3 temperature and therefore fully austenitized. Consequently, the microstructure is martensitic after quenching. The temperature in the intercritical heat-affected zone (ICHAZ) rises to a level between A_1 and A_3, and its microstructure after quenching consists of ferrite and martensite. The peak temperature in the subcritical heat-

---

✉ Manfred Stadler
manfred.stadler@unileoben.ac.at

[1] Department of Materials Science, Montanuniversität Leoben, Franz-Josef-Strasse 18, 8700 Leoben, Austria

[2] voestalpine Stahl GmbH, voestalpine-Strasse 3, 4020 Linz, Austria

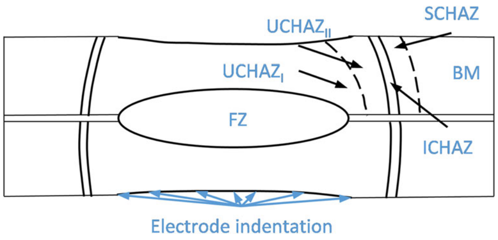

Fig. 1 Schematic illustration of the emerging zones in a RSW from the inside out: Fusion zone (FZ), coarse grain upper critical heat-affected zone (UCHAZ$_I$), fine grain upper critical heat-affected zone (UCHAZ$_{II}$), intercritical heat-affected zone (ICHAZ), subcritical heat-affected zone (SCHAZ), and the base metal (BM)

affected zone (SCHAZ) is lower than the A_1 temperature. Tempering of the microstructure occurs in this area and leads to softening [5, 8–10].

A possible approach to improve the performance of AHSS spot welds is in-process tempering via a second pulse. There are basically two different concepts of double pulsing. The first concept aims to transform the cast-like structure. In the past, several authors recommended a short cooling time between the pulses, leading to recrystallization of the outer FZ and consequently to the transformation of the cast-like structure. Eftekharimilani et al. [11] illustrated that the shape of the prior austenite grains (PAGs) changes from an elongated to an equiaxed shape at the edge of the FZ. Furthermore, it is reported that segregations at the edge of the FZ are reduced after a second pulse, and therefore the risk of intergranular failure is reduced [12]. Chabok et al. [13] stated that the second pulse lowers the residual stress at the edge of the FZ and furthermore leads to a severe softening of the SCHAZ. Moreover, the recrystallization causes an increase of high-angle grain boundaries in the UCHAZ [13]. With this concept, cracking behavior and ultimate strength during cross tension tests were improved significantly [11–17]. The other concept aims to soften the hard and therefore brittle martensitic FZ. Therefore, the cooling time is extended to a level that the temperature of the FZ reaches martensite finish (M_f) temperature. The second pulse, usually lower than the first one, tempers the martensite and therefore increases its ductility. In the past, this approach was successfully used to improve the mechanical performance of welds in TRIP steel [18, 19].

Although double pulse RSW of AHSS is well-documented in the literature [11–17, 20], the characterization of the occurring zones in a double pulse welded TBF steel with a tensile strength of 1200 MPa is still missing. The present work shows methods to characterize and distinguish the different zones in a temper pulse welded TBF steel and aims at understanding the ongoing tempering effects during the second pulse. Two different welding schemes were compared, and the differences regarding the microstructure are illustrated using light optical microscopy and scanning electron microscopy. Moreover, hardness mappings with several hundred indents per weldment were performed to investigate the influence of the second pulse on the hardness and to correlate it to the observed microstructure.

1.1 Experimental

A 1200 MPa TBF steel with a nominal composition of 0.2C/1.5Si/2.5Mn (wt%) was investigated. The steel sheets with a thickness of 1.34 mm were electrolytically galvanized, having a coating thickness of 6.6–8.6 μm per side as specified in VDA 239–100 [21]. RSW was performed using a Nimak MFDC-1000 Hz pedestal-type welding machine, equipped with a AutoSpatz regulator, delivering constant current and F1–16–20-6 electrodes with a force of 4.5 kN as recommended in VDEh SEP1220–2 [22]. In this paper, two different double pulse welding sequences were applied which are illustrated in Fig. 2. For the sequence illustrated in Fig. 2 (a), the first pulse is just high enough to produce a weld nugget that fulfills the quality criterion of a minimum spot weld diameter of $4*\sqrt{t}$, where t is the sheet thickness. Although this criterion is not completely reliable for AHSS welds, it was chosen in the present study as it is well-known as a quality criterion for spot welds. The sample welded with this minimum current (I_{min}) is hereinafter referred to as sample I_{min}. For the first

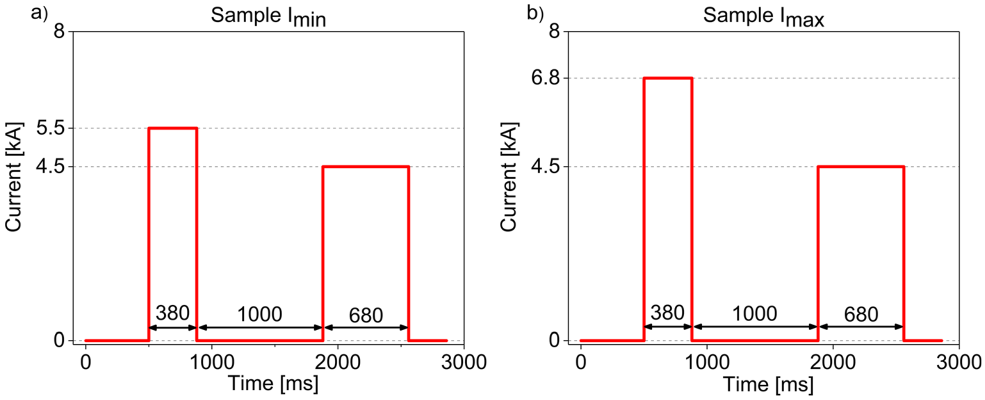

Fig. 2 Welding sequences for (a) sample I_{min} and (b) sample I_{max}

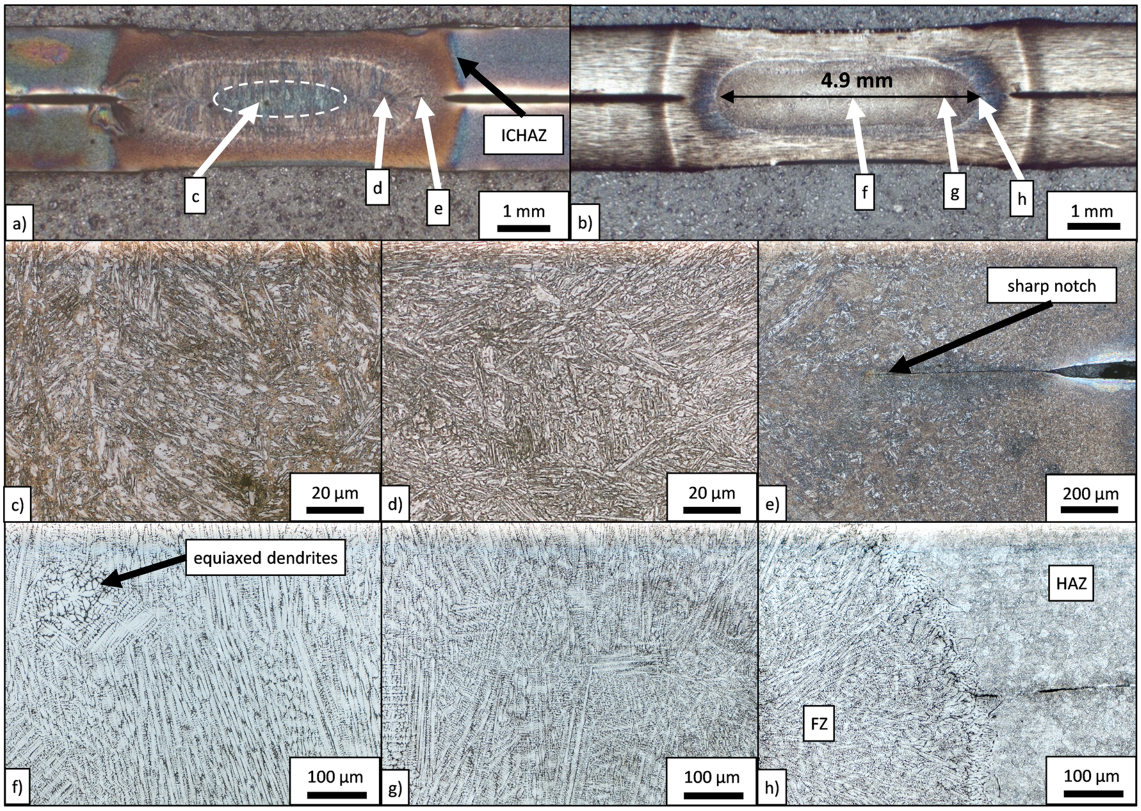

Fig. 3 Overview of sample I_{min} after etching with (a) Nital and (b) picric acid. Detailed images of (c) the inner FZ, (d) the outer FZ, and (e) the transition between FZ and HAZ after Nital etching. Detailed images of (f) the inner FZ, (g) the outer FZ, and (h) the transition from FZ to HAZ after etching with picric acid

pulse of the sequence illustrated in Fig. 2 (b), the highest current without splashing (I_{max}) was chosen as described in VDEh SEP1220–2 [22]. The sample welded with this sequence is hereinafter referred to as sample I_{max}. In the preliminary investigation, a temper pulse of about two-thirds of I_{max}, approximately 4.5 kA, turned out to be ideal for samples welded at the splashing limit. This current of 4.5 kA was chosen for the second pulse of both sequences. For each sequence, a squeeze time of 500 ms was followed by a 380 ms welding time, a cooling time of 1000 ms, a 680 ms lasting second pulse, and a hold time of 300 ms. The extraordinary long cooling time of 1000 ms was chosen to be sure that the temperature prior to the second pulse is safely below A_1 and to clearly differentiate the present concept from the recrystallization pulse concept.

For microstructural characterization, cross sections were ground, polished, and finally etched with 3% Nital solution for a few seconds for light optical microscopy (LOM) investigations and for less than 1 s for investigations via scanning electron microscopy (SEM). To visualize the dendrites and the prior austenite grains, a mixture of cold saturated picric acid, Natriumdodecylbenzolsulfonat, and hydrochloric acid was used. LOM images were taken with a Zeiss M1M Imager equipped with a AxioCam MRc5 camera, both from Zeiss. SEM investigations were performed on Zeiss EVO 50 using secondary electron contrast.

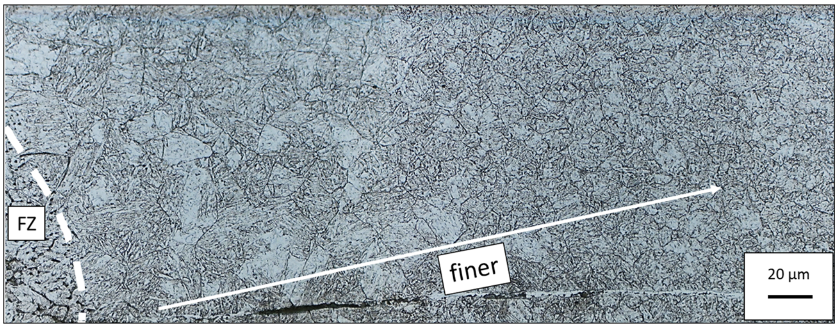

Fig. 4 LOM image of the UCHAZ of sample I_{min} after etching with picric acid. PAGs are visible, and their size decreases with increasing distance to the FZ

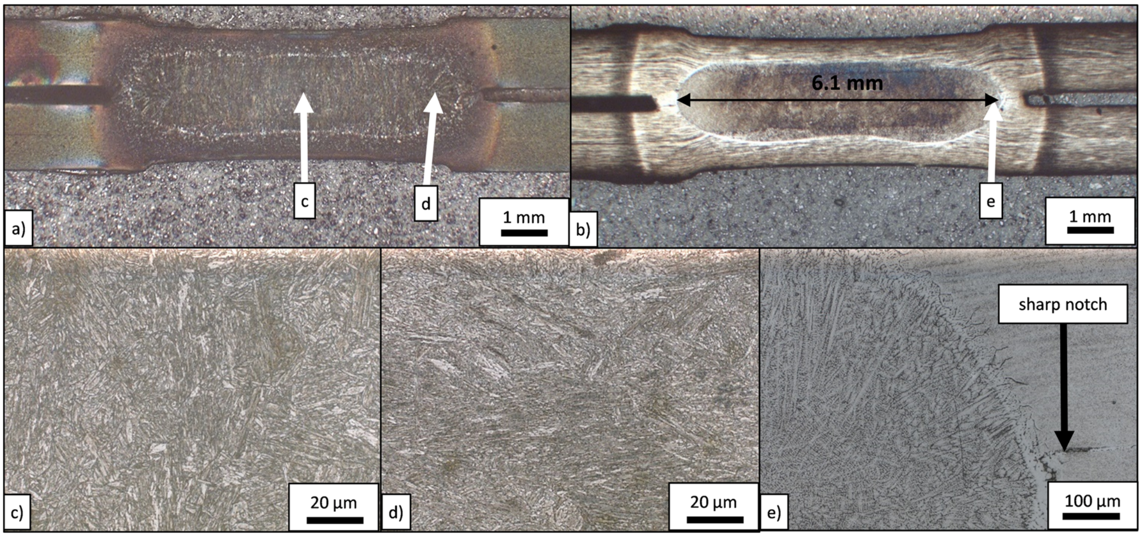

Fig. 5 Overview of sample I_{max} after etching with (a) Nital and (b) picric acid. Detailed images of (c) the center of the FZ, (d) the edge of the FZ after Nital etching, and (e) the transition from FZ to HAZ after etching with picric acid

For Vickers hardness mappings, a Qness Q60A+ hardness tester was used. The distance between the indents was 150 µm, and the load was 300 g.

2 Results

2.1 Microstructural characterization via LOM

In order to characterize the microstructure of sample I_{min}, LOM images were taken. Figure 3 (a) shows an overall image of the weld after Nital etching and Fig. 3 (b) after etching with picric acid. Nital attacks the FZ nonuniformly and separates it into an inner and an outer part. Furthermore, this etching method offers an easy way to distinguish the martensitic UCHAZ from the ICHAZ (marked by an arrow in Fig. 3 (a)), since the ferritic areas are stronger attacked due to their lower carbon content [23]. Comparing Fig. 3 (c) and Fig. 3 (d), it can be seen that the microstructure of the inner FZ indeed differs from the outer one. The inner zone seems coarser and more heterogeneous, while the outer zone is homogeneous. Figure 3 (e) illustrates that Nital is not the most suitable etching method for distinguishing the FZ from the HAZ as they are both martensitic. The notch between the sheets is sharp, as indicated by an arrow in Fig. 3 (e)), which is typical for RSW [5]. It is reported that picric acid attacks elements like phosphorus [24]. Since phosphorus tends to segregate between the dendrites [25], it is an appropriate method to visualize solidification structure of the FZ. The size of the FZ is approximately 4.9 mm. Figure 3 (f) and Fig. 3 (g) show the orientation of the dendrites alongside the heat dissipation. In the case of the inner zone (Fig. 3 (f)), the water-cooled electrodes represent the dominant heat sinks. As the inner FZ solidifies last, therefore the temperature gradient is relatively small compared to the outer FZ; also equiaxed dendrites appear. At the edge of the FZ, depicted in Fig. 3 (h), the orientation of the dendrites changes, since the heat mainly dissipates toward the BM. This etching clearly visualizes the transition from the FZ to the HAZ, since phosphorus in the FZ is mainly segregated between the dendrites, while it preferentially segregates at the grain boundaries in the UCHAZ.

The main metallographic application of picric acid is the visualization of the PAGs in a martensitic microstructure [26]. Figure 4 shows the PAGs in the UCHAZ of sample I_{min}. The PAG size of the area in close proximity to the FZ is about 20 µm and larger. With a greater distance to the FZ, the PAG size decreases, and therefore the $UCHAZ_I$ merges into the $UCHAZ_{II}$. This transition takes place within approximately 100–200 µm.

LOM images of sample I_{max} were taken as well. Figure 5 (a) shows an overall image of the weld after Nital etching and Fig. 5 (b) after etching with picric acid. Compared to sample

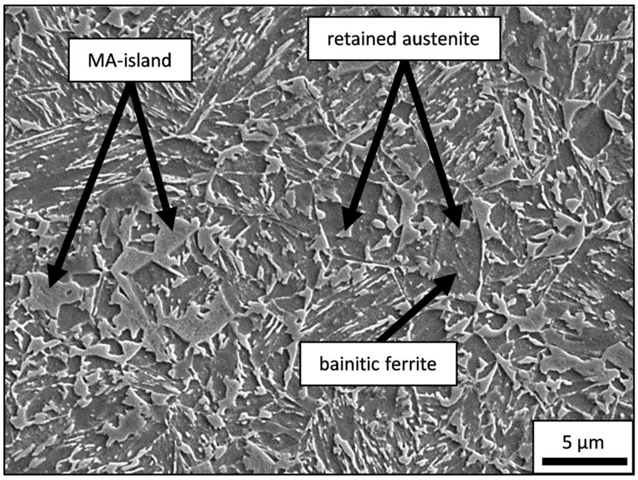

Fig. 6 SEM image of the BM of the investigated TBF steel

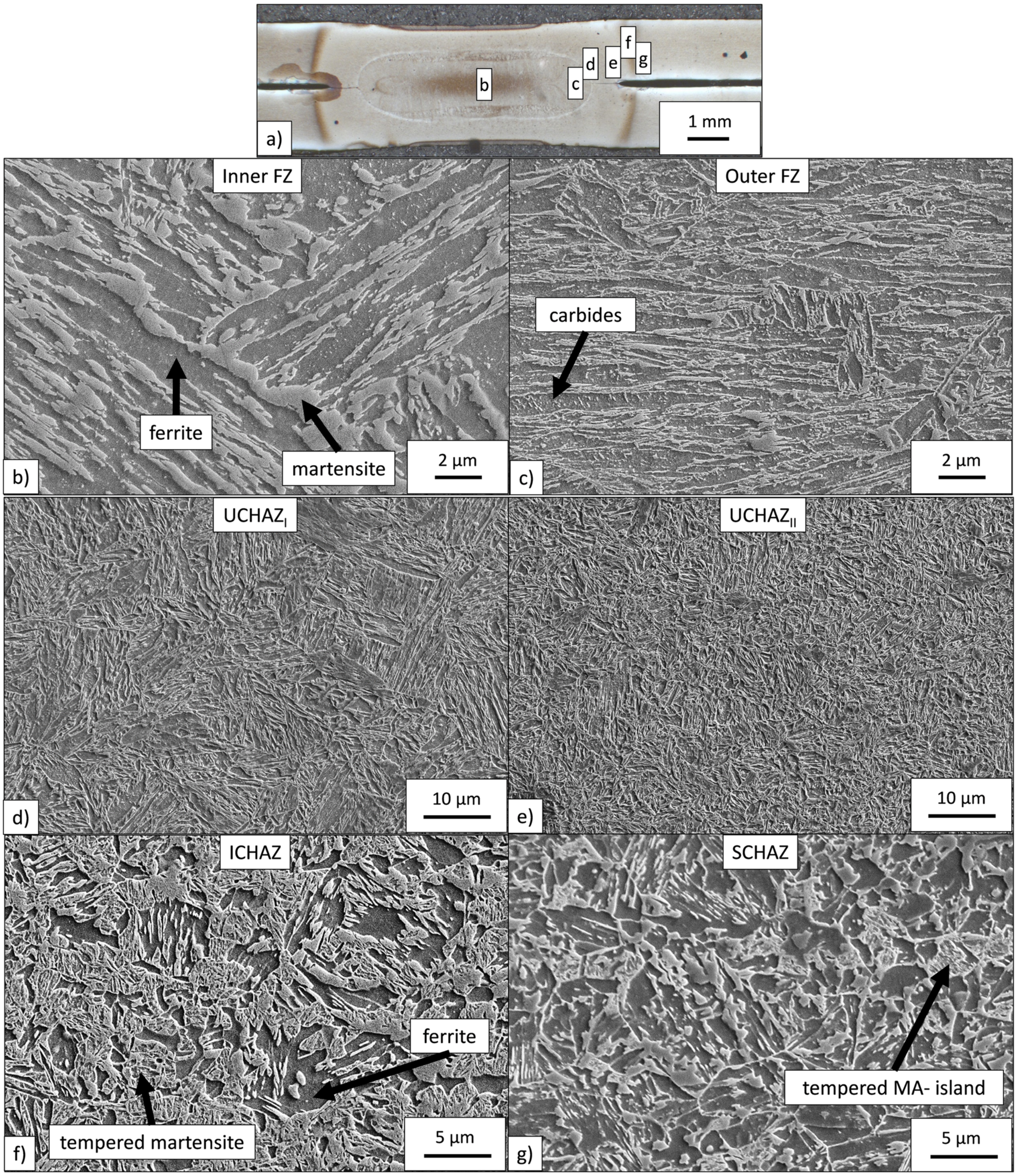

Fig. 7 (a) Overview LOM image of sample I_{min} after Nital etching. SEM image of (b) the inner FZ showing a ferritic/martensitic microstructure, (c) the outer FZ consisting of tempered martensite with small carbides, (d) the UCHAZ$_{I}$ containing coarse grained martensite, and (e) the UCHAZ$_{II}$ containing fine grained martensite. The martensite in (f) the ICHAZ and the MA islands in (g) the SCHAZ show a tempered structure

I_{min}, the gap between the sheets is larger, but the resulting notch is still sharp, as indicated by an arrow in Fig. 5 (e)). The larger heat input during the first pulse also results in a larger FZ (6.1 mm) and a deeper indentation depth. Figure 5 (c) and Fig. 5 (d) indicate that the microstructure in the center and at the edge of the FZ is martensitic and, in contrast to sample I_{min}, not divided into two different parts. The edge of the FZ after etching with picric acid is depicted in Fig. 5 (e). While the interface between FZ and HAZ can be well-recognized, the PAG boundaries were not revealed in this sample.

2.2 Microstructural characterization via SEM

For higher-resolution imaging of the microstructure, SEM was performed. From the SEM image of the BM in Fig. 6, it is apparent that the BM of a TBF steel consists of a multiphase microstructure. Due to the low carbon content, the bainitic ferrite is strongly attacked by the etchant Nital and therefore appears deeper. The small, round islands within the bainitic matrix are retained austenite. The larger, angular regions show a slight substructure at higher magnification and are a combination of austenite and martensite, the so-called MA-islands [27].

The occurring zones of sample I_{min} are characterized in the following. Figure 7 (a) gives an overview and indicates where the images were taken. The microstructure of the inner FZ, which is illustrated in Fig. 7 (b), consists of ferrite and untempered martensite and is much coarser compared to the outer FZ shown in Fig. 7 (c). The martensite in the outer FZ exhibits small, regularly oriented carbides which indicate pronounced tempering. These carbides are missing in the inner FZ. The $UCHAZ_I$ and $UCHAZ_{II}$ depicted in Fig. 7 (d) and Fig. 7 (e) mainly differ regarding the much coarser martensitic microstructure in the $UCHAZ_I$. Tempering effects in the form of small carbides are less pronounced. As can be seen in Fig. 7 (f), the ICHAZ consists of a ferritic and martensitic microstructure. However, the martensitic areas show a pronounced inner structure characteristic of tempered martensite. The microstructure of the SCHAZ, which is shown in Fig. 7 (g), is similar to the BM, consisting of bainitic ferrite, MA islands, and retained austenite. However, some of the MA islands show a distinct inner structure compared to the flat MA islands of the BM. This inner structure is attributed to temper effects typical for the SCHAZ of a martensite containing AHSS [28].

SEM micrographs of sample I_{max} were taken as well. The microstructure of the center of the FZ of this sample, which is shown in Fig. 8, consists of tempered martensite and is comparable to the outer FZ of sample I_{min} (Fig. 7 (c)) rather than to the inner FZ (Fig. 7 (b)). The edge of the FZ, UCHAZ, and SCHAZ of sample I_{max} was also investigated but did not differ significantly from the zones in sample I_{min} and are therefore not depicted.

The martensitic areas in the ICHAZ of sample I_{max} depicted in Fig. 9 do not show pronounced signs of tempering. Only a small amount of them have an inner substructure, while the majority is smooth.

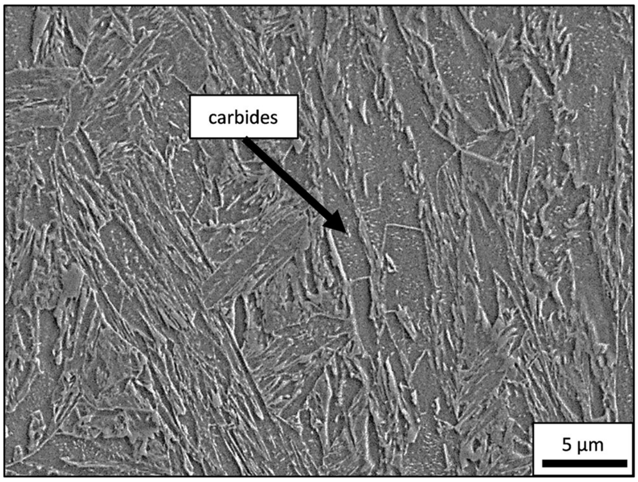

Fig. 8 SEM image of the center of the FZ of sample I_{max} showing tempered martensite

2.3 Hardness mapping

In order to investigate the influence of tempering on the hardness profile of the weldment, hardness mappings were recorded. As illustrated in Fig. 10 (a), the different microstructures of the inner and the outer FZ are also reflected in the hardness mappings of sample I_{min}. The hardness of the inner FZ is about 420 HV and therefore 50 to 60 HV harder than the outer FZ. The hardness level of the UCHAZ rises from 420 to 480 HV with increasing distance to the FZ and drops to 420 HV in the ICHAZ. With a hardness of approximately 350 HV, the SCHAZ is about 70 HV softer than the BM. The hardness mapping of sample I_{max} is depicted in Fig. 10 (b). In contrast to sample I_{min}, the hardness of the FZ of sample I_{max} increases from the inside out, from about 360 to 420 HV. The hardest area is the UCHAZ with more than 500 HV, and therefore it is much harder than the UCHAZ of sample I_{min}.

3 Discussion

An inner FZ is formed in sample I_{min}, as can be seen in Fig. 3. This sample was welded with a lower current at the first pulse. The metallographic constituents of this inner fusion zone were identified via SEM. Figure 7 (b) illustrates that its microstructure consists of two phases, which are attacked differently by Nital. According to Angeli et al. [23], the chemical potential of the individual phases in low alloyed steels depends mainly on their carbon content. Thus it can be inferred that the stronger attacked areas correspond to ferrite, while the less attacked phase is associated with carbon rich martensite. Since the martensitic areas of this dual-phase microstructure show no signs of tempering, they are most likely transformed during the final quenching. Hence, the temperature of the inner FZ must have been between A_1 and A_3 prior to the final quenching, causing partial reaustenitization during the second pulse. In contrast, the microstructure of the outer FZ, depicted in Fig. 7 (c), consists of tempered martensite as proofed by the occurring carbides. Consequently, the peak temperature of this area must have been lower than A_1 during the second pulse since only one phase is present. Hernandez et al. [20] also observed a strong correlation between the magnitude of the pulse and the evolving microstructure by varying the second pulse instead of the first pulse as in this work. They simulated the temperature of the FZ during the second pulse and stated that a current of 5 kA results in a temperature below A_1, leading to softening, while the temperature after a second pulse of 7 kA was above A_3 resulting in reaustenitization. The hardness mapping of sample I_{min}, depicted in Fig. 10 (a), shows that the dual-phase microstructure of the inner FZ is 50 to 60 HV harder than the

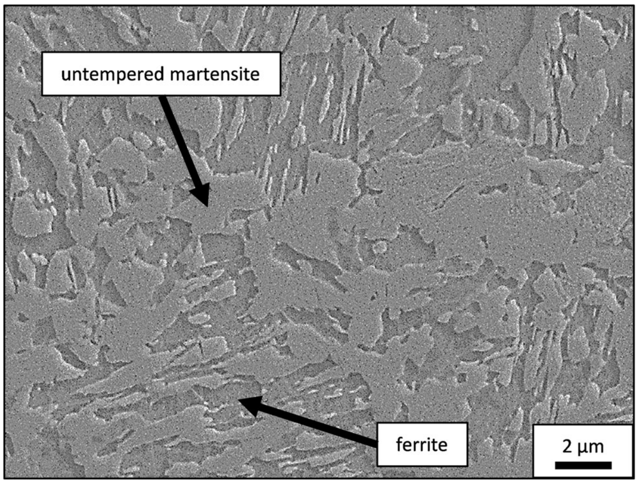

Fig. 9 SEM image of the ICHAZ of sample I_{max} consisting of ferrite and untempered martensite

tempered martensite of the outer one. On the contrary, as can be seen in Fig. 5 and Fig. 8, the entire FZ of sample I_{max} consists of tempered martensite. This indicates that the peak temperature during the second pulse must have been lower than the A_1 temperature since no phase transformation occurred. The hardness of the weldment rises from the inside out with a hardness peak in the $UCHAZ_{II}$ as illustrated in Fig. 10 (b). This is due to the decreasing peak temperature during the second pulse and consequently the less pronounced tempering effects with increasing distance to the center of the FZ. With a hardness of more than 500 HV, $UCHAZ_{II}$ of sample I_{max} is much harder than its sample I_{min} counterpart. This can be explained by the higher heat input during the first pulse in sample I_{max} resulting in a bigger weld nugget as can be seen comparing Fig. 3 (b) and Fig. 5 (b). Due to the larger distance between the center of the FZ and the $UCHAZ_{II}$ in sample I_{max}, the temperature does not rise to a level where effective tempering occurs during the second pulse. The comparison of the ICHAZ of both samples depicted in Fig. 7 (f) and Fig. 9, also illustrates this circumstance. The martensitic areas in the ICHAZ of sample I_{min} (Fig. 7 (f)) show a clear inner substructure due to tempering while these areas are smooth in the ICHAZ of sample I_{max}. This indicates that the temperature during the second pulse of sample I_{max} is lower in this area.

Generally, for RSW, the heat dissipates toward the cooled electrodes and the BM. For thin sheets, the cooling mechanism of small welding nuggets is dominated by heat loss toward the cooled electrodes [29]. This can be visualized by the dendrites in the FZ, since they show a preferred orientation along the maximal thermal gradient [11]. In the inner FZ (Fig. 3 (f)), the dendrites are mainly oriented in vertical direction, illustrating that the heat dissipates to the cooled electrodes, while the dendrites at the edge of the FZ are mainly oriented in horizontal direction, toward the BM (Fig. 3 (h) and Fig. 5 (e)). Comparing Fig. 3(b) and Fig. 5 (b), it can be seen that due to the lower heat input in sample I_{min}, the electrode indentation depth of this sample is much lower compared to sample I_{max}. Consequently, the distance between the cooled electrodes and the liquid weld pool is larger, which results in a lower cooling rate according to Pouranvari and Marashi [5]. This may lead to a higher temperature in sample I_{min} after the cooling time compared to sample I_{max} and consequently to a higher temperature during the second pulse in this sample. Moreover, for the heat generation and temperature evolution in the nugget, the current plays an important role [30]. Compared to sample I_{max}, due to the lower current during the first pulse, the nugget diameter of sample I_{min} is smaller after the first pulse. This means that during the second pulse, the ratio of the passing current to the size of the FZ is larger for sample I_{min}, and consequently, more heat is generated. This circumstance may also be responsible for the reaustenitization of the inner FZ of sample I_{min} during the second pulse. However, the prediction of the exact temperature distribution and nugget size evolution due to a given current is highly

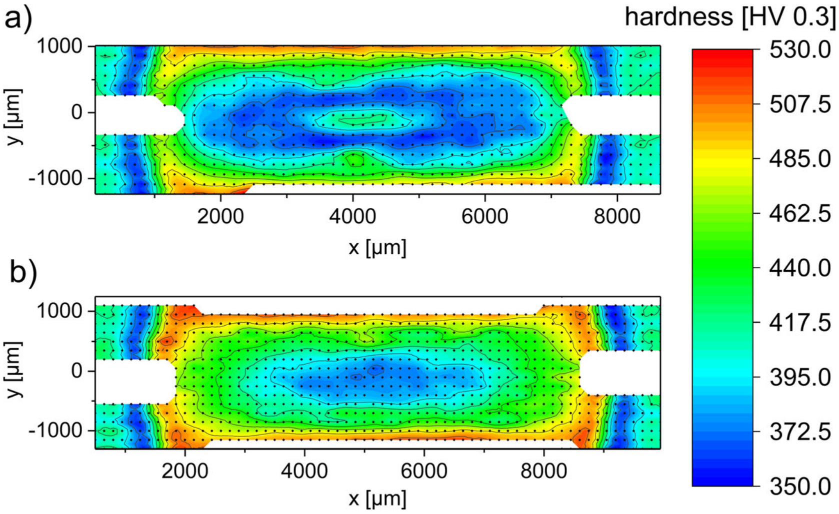

Fig. 10 Vickers hardness mapping of (a) sample I_{min} and (b) sample I_{max}

complex and depends on many aspects [31] and is beyond the scope of this paper.

Besides the visualization of dendrites, picric acid is widely used to illustrate the PAGs in martensitic steels [26], and therefore it is an appropriate etching method to characterize the UCHAZ of spot welds. For sample I_{min}, this etching achieved valuable results, as can be seen in Fig. 4, where a significant difference in PAG size as a function of the distance to the FZ can be seen. However, it is noteworthy that the PAG boundaries are not visible in sample I_{max}. Generally, tempering is an effective way to improve the etching result for AHSS [32]. During this heat treatment, elements like phosphorus segregate to the PAG boundaries, resulting in an attack during the subsequent etching. Since the PAG boundaries of sample I_{max} are not revealed, it can be concluded that the degree of tempering of the UCHAZ is lower compared to sample I_{min}. Consequently, picric acid-based etching is not only a good way to characterize the UCHAZ but also to estimate the degree of tempering in double pulse RSW.

4 Conclusion

In the present work, RSW of a 1200 MPa TBF steel was performed using two different double pulse welding schemes. The different zones were characterized by LOM, SEM, and hardness mappings, and the following conclusions can be drawn:

1) If the first pulse is low and the weld nugget therefore small, an inner FZ with a different microstructure than the residual FZ forms after the second pulse. This inner FZ shows no signs of tempering and consists of ferrite and untempered martensite as a result of a partial reaustenitization during the second pulse. The hardness map reveals that this inner FZ is harder than the outer FZ consisting of tempered martensite.
2) If the first pulse is high and the weld nugget is therefore large, the entire FZ is tempered during the second pulse. The hardness map reveals that due to the temperature gradient, the tempering effect decreases from the inside out. Observation of the microstructure in the SEM illustrated that the ICHAZ is not tempered significantly by the second pulse, since the distance from the FZ is large.
3) A higher energy input during the first pulse is associated with a deeper electrode indentation depth compared to a lower first pulse. This results in a faster cooling rate of the center of the FZ due to the shorter distance to the liquid melt pool. Furthermore, due to the larger weld nugget of sample I_{max}, the ratio of current to the size of the FZ during the second pulse is lower, and less heat is generated. This contributes to the inhibited reaustenitization and the microstructure of the inner FZ of sample I_{max} consequently consists of tempered martensite.
4) Etching with picric acid visualizes the PAGs in the strongly tempered UCHAZ of sample I_{min} but does not attack the PAG boundaries of sample I_{max}. This is because due to severe tempering, elements like phosphorus segregate to the grain boundaries extensively. Thus, this etching method is capable of estimating the degree of tempering of the UCHAZ comparatively between two double pulse welded samples.

Acknowledgements Open access funding provided by Montanuniversität Leoben.

Funding information Funding of the Austrian BMVIT (846933) in the framework of the program "Production of the future" and the "BMVIT Professorship for Industry" is gratefully acknowledged.

References

1. Matlock DK, Speer JG (2009) Third generation of AHSS: microstructure design concepts. In: Haldar A, Suwas S, Bhattacharjee D (eds) Microstructure and texture in steels. Springer London, London, pp 185–205
2. Hofer C, Leitner H, Winkelhofer F et al (2015) Structural characterization of "carbide-free" bainite in a Fe–0.2C–1.5Si–2.5Mn steel. Mater Charact 102:85–91
3. Hofer C, Winkelhofer F, Clemens H et al (2016) Morphology change of retained austenite during austempering of carbide-free bainitic steel. Mater Sci Eng A 664:236–246
4. Hofer C, Primig S, Clemens H et al (2017) Influence of heat treatment on microstructure stability and mechanical properties of a carbide-free bainitic steel. Adv Eng Mater 19(4):1600658
5. Pouranvari M, Marashi SPH (2013) Critical review of automotive steels spot welding: process, structure and properties. Sci Technol Weld Join 18(5):361–403
6. Den Uijl NJ, Smith S (eds) (2006) Resistance spot welding of advanced high strength steels for the automotive Industry. In: 4th International Seminar on Advances in Resistance Welding, Wels, Austria (pp. 30–60)
7. Pouranvari M, Marashi SPH (2013) Key factors influencing mechanical performance of dual phase steel resistance spot welds. Sci Technol Weld Join 15(2):149–155
8. Pouranvari M, Sobhani S, Goodarzi F (2018) Resistance spot welding of MS1200 martensitic advanced high strength steel: microstructure-properties relationship. J Manuf Process 31:867–874

9. Pouranvari M, Asgari HR, Mosavizadch SM et al (2013) Effect of weld nugget size on overload failure mode of resistance spot welds. Sci Technol Weld Join 12(3):217–225
10. Lu Y, Peer A, Abke T et al (2018) Subcritical heat affected zone softening in hot-stamped boron steel during resistance spot welding. Mater Des 155:170–184
11. Eftekharimilani P, van der Aa EM, Hermans MJM et al (2017) Microstructural characterisation of double pulse resistance spot welded advanced high strength steel. Sci Technol Weld Join 22(7):545–554
12. Eftekharimilani P, van der Aa EM, Hermans MJM et al (2017) The microstructural evolution and elemental distribution of a 3rd generation 1 GPa advanced high strength steel during double pulse resistance spot welding. Welding World 61(4):691–701
13. Chabok A, van der Aa EM, De Hosson JTM et al (2017) Mechanical behavior and failure mechanism of resistance spot welded DP1000 dual phase steel. Mater Des 124:171–182
14. Matsuchita M, Taniguchi K, Oi K (2013) Development of next generation resistance spot welding technologies contributing to auto body weight reduction. JFE Technical Report 18:111–117
15. Van der Aa EM, Amirthalingam M, Winter J, Hanlon DN, Hermans MJM, Rijnders M, Richardson IM (ed) (2015) improved resistance spot weldability of 3rd generation AHSS for automotive applications. In: 11th international seminar on numerical analysis of Weldability, Graz. Austria
16. Sawanishi C, Ogura T, Taniguchi K et al (2013) Mechanical properties and microstructures of resistance spot welded DP980 steel joints using pulsed current pattern. Sci Technol Weld Join 19(1): 52–59
17. Liu XD, Xu YB, Misra RDK et al (2019) Mechanical properties in double pulse resistance spot welding of Q&P 980 steel. J Mater Process Technol 263:186–197
18. Chuko WL, Gould JE (2002) Development of appropriate resistance spot welding practice for transformation-hardened steels. Weld J 81(1):1–8
19. Shi G, Westgate SA (2005) Techniques for improving the weldability of TRIP steel using resistance spot welding. In: paper for 1st international conference of the high strength steel, (pp. 1-13)
20. Hernandez VB, Okita Y, Zhou Y (2012) Second pulse current in resistance spot welded TRIP steel: Effects on the microstructure and mechanical behavior. Impulse:91
21. Verband Der Automobilindustrie E. V. (2016) VDA 239–100: Flacherzeugnisse aus Stahl zur Kaltumformung
22. Stahl-Eisen-Prüfblätter (SEP) des Stahlinstituts VDEh SEP 1220–2: Testing and documentation guideline for the joinability of thin sheet of steel-Part 2: Resistance Spot Welding
23. Angeli J, Fureder E, Panholzer M et al (2006) Etching techniques for characterizing the phases of low-alloy dual-phase and TRIP steels. Practical Metallography 43(10):489–504
24. Christien F, Le Gall R, Saindrenan G (2003) Phosphorus grain boundary segregation in steel 17-4PH. Scr Mater 48:11–16
25. Amirthalingam M, van der Aa EM, Kwakernaak C et al (2015) Elemental segregation during resistance spot welding of boron containing advanced high strength steels. Weld World 59(5):743–755
26. Bechet S, Beaujard L (1955) New reagent for the micrographical demonstration of the austenite grain of hardened or hardened-tempered steels. Revue de Métallurgie 52:830–836
27. Hofer C, Bliznuk V, Verdiere A et al (2018) High-resolution characterization of the martensite-austenite constituent in a carbide-free bainitic steel. Mater Charact 144:182–190
28. Hernandez VH, Panda SK, Kuntz ML et al (2010) Nanoindentation and microstructure analysis of resistance spot welded dual phase steel. Mater Lett 64(2):207–210
29. Kim EW, Eagar TW (1988) Parametric analysis of resistance spot welding lobe curve. SAE Trans:107–118
30. Deutscher Verband Für Schweißen Und Verwandte Verfahren E.V. DVS 2902–4: Widerstandspunktschweißen von Stählen bis 3 mm Einzeldicke - Grundlagen, Vorbereitung und Durchführung
31. Williams NT, Parker JD (2004) Review of resistance spot welding of steel sheets part 1 Modelling and control of weld nugget formation. Int Mater Rev 49(2):45–75
32. Esterl R, Sonnleitner M, Stadler M et al (2018) Microstructural characterization of ultra-high strength martensitic steels. Practical Metallography 55(4):203–222

Paper II

M. Stadler, R. Schnitzer, M. Gruber, C. Hofer

Improving the mechanical performance of a resistance spot welded 1200 MPa TBF steel

International Journal of Materials Research 112 (2021) 262-270

International Journal of
MATERIALS RESEARCH

Zeitschrift für METALLKUNDE

Original Contributions

Manfred Stadler[a], Ronald Schnitzer[a], Martin Gruber[b], Christina Hofer[a]

[a] Department of Materials Science, Montanuniversität Leoben, Leoben, Austria
[b] voestalpine Stahl GmbH, Linz, Austria

Improving the mechanical performance of a resistance spot welded 1200 MPa TBF steel

In the present work different approaches to improve the mechanical properties of a resistance spot welded 1200 MPa transformation induced plasticity-aided bainitic ferrite steel are evaluated. An extension of the welding time results in coarsening of the microstructure of the outer fusion zone and the maximum force derived by the cross tension strength test did not improve significantly. A temper pulse after a long cooling time leads to pronounced softening of the fusion zone, as determined by hardness mapping, which resulted in enhanced weld properties. A recrystallization pulse modifies the shape of the prior austenite grains at the outer fusion zone, which was visualized with electron backscatter diffraction. This also resulted in a significant improvement of maximum force. For all approaches the failure mode improved, which can be attributed to an increased fraction of high angle grain boundaries at the edge of the fusion zone.

Keywords: Resistance spot welding; Double pulsing; Advanced high strength steels; AHSS; TRIP-aided bainitic ferrite

1. Introduction

Third generation advanced high strength steels (AHSS) combine high strength with good formability and are potential candidates for use in body components in the automotive industry due to their superior crash behavior [1, 2]. Promising representatives are the transformation-induced plasticity (TRIP)-aided bainitic ferrite (TBF) steels. Their microstructure mainly consists of carbide-free bainite and a certain amount of retained austenite in order to enable the TRIP-effect. The austenite is stabilized by carbon enrichment during an isothermal heat treatment [2, 3].

Resistance spot welding (RSW) is the dominant technology for sheet metal joining in the automotive industry [4]. Due to the relatively high alloying content of third generation AHSS and the rapid cooling during RSW, the welds are often fully martensitic and therefore hard and brittle. This, combined with the reported tendency of alloying elements such as manganese, silicon and phosphorus to segregate to grain boundaries during solidification, enhances intergranular failure [5]. These circumstances lead to insufficient mechanical properties during the cross tension strength (CTS) test and deteriorate the crash behavior. Therefore, the weldability of third generation AHSS is restricted [4, 6, 7].

In recent years, numerous studies [8–13] focused on the improvement of the mechanical properties of high strength steel spot welds. A simple way to improve the mechanical performance is to increase the load bearing area, namely the fusion zone (FZ), by increasing the heat input [4]. Due to Joule's law of $Q_w = I^2 \times R \times t$, the heat generation Q_w depends on the applied welding current I, the temperature-dependent and therefore dynamic resistance R and the welding time t. For a given current, the heat input can consequently be increased by extending the welding time. For low carbon steels, the FZ size increases with extended welding times, especially at lower current levels, which leads to an enhanced weld strength [14]. It has been reported that the maximum force during the shear tensile test and the failure mode improved significantly for these steel grades due to longer welding times [15]. An enlargement of the FZ due to an extended welding time and a concomitant improvement of the mechanical properties was also reported for a micro-alloyed steel [16] and for high strength steels [17]. Again, the enlargement of the FZ due to longer welding times was more effective at lower currents since the maximum size is limited by its decreasing dynamic resistance and expulsion [4].

Generally, the mechanical properties of high strength steel welds can be improved by a post-processing heat treatment [18]. Double pulsing is a feasible approach to carry out the heat treatment in-process. Two concepts are suggested in literature. Both rely on a second pulse subsequent to a cooling time, that heat-treats the cast-like, often hard and brittle, FZ.

The first concept relies on quenching the FZ below the martensite finish temperature prior to a second pulse that aims to temper and consequently soften the martensitic FZ, resulting in enhanced toughness. It has been reported that the mechanical performance of TRIP steels can be improved significantly with this approach [19–22]. Especially, the elimination of the unwanted interfacial failure (IF) mode has been observed [23]. The cooling time between the pulses has to be long enough to ensure sufficient cooling of the FZ and the second pulse has to be lower than the first pulse to avoid re-austenitization of the FZ and extensive softening of the upper-critical heat affected zone (UCHAZ) [24].

In contrast, the second concept relies on recrystallizing the microstructure of the outer FZ with the second pulse. According to simulated thermal histories for third generation AHSS welds, the edge of the FZ cools down rapidly and even solidifies during extremely short cooling times between the pulses [10, 25]. Therefore, this concept is characterized by an extremely short cooling time to keep the temperature and therefore the dynamic resistance during the second pulse at a high level. A high-current second pulse is required to ensure sufficient heat input to achieve recrystallization of the outer FZ while the inner FZ re-melts. Therefore, the inner zone is referred to as the secondary FZ and the initial FZ is termed the primary FZ [10]. According to literature [10, 22], the second pulse destroys the cast-like structure at the edge of the FZ and leads to more equiaxed prior austenite grains (PAGs). Eftekharimilani et al. [10] stated that this equiaxed shape is decisive in terms of the improved mechanical properties and that the recrystallization is accompanied by refinement and reduction of the block width which is reported to affect the mechanical performance in a positive way. Moreover, a second pulse is reported to lead to a refinement of the martensitic packets in the center of the FZ which is assumed to improve the peak load and failure mode during the CTS test [21]. It is also reported that elements such as phosphorus are more evenly distributed, especially after a high current second pulse, which reduces the risk of intergranular failure and improves the mechanical properties [10, 11]. Moreover, improved mechanical performance of a recrystallization pulse welded DP1000 dual-phase steel was attributed to the lowered residual strains at the edge of the FZ and the severe softening of the sub-critical heat affected zone (SCHAZ) [8]. Also, the fraction of high angle grain boundaries in the UCHAZ increased, leading to crack deflection and consequently to enhanced toughness [8].

Up to now, these concepts have never been comparatively studied on a third generation AHSS in order to reveal the microstructural evolution and the influence on the mechanical properties. Hence, in the present work, the described approaches were applied to a TBF steel with a tensile strength of 1200 MPa. The aim of this study was to investigate the effect of the different double pulse welding sequences on the martensitic features of the FZ, the hardness distribution and consequently the mechanical properties and compare them to conventional and extended single pulse welds for this novel third generation AHSS grade.

2. Materials and methods

A TBF steel with a chemical composition of 0.2C/1.5Si/2.5Mn (wt.%) and a tensile strength of 1200 MPa was investigated. A detailed microstructural characterization of this material [3, 26, 27] as well as the individual zones in the HAZ after resistance spot welding [24] were carried out in previous works. The nominal sheet thickness was 1.34 mm and the sheets were electrolytically galvanized with a coating thickness of 6.6–8.6 µm per side as specified

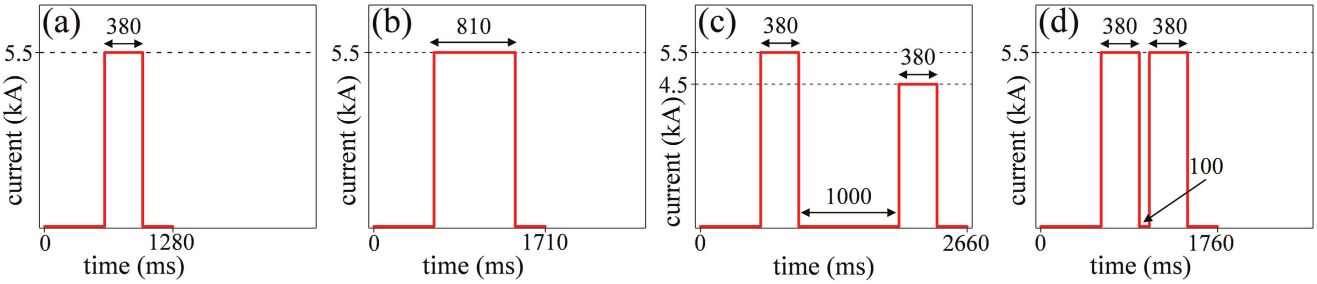

Fig. 1. Welding sequences of the (a) conventional single pulse, (b) extended single pulse, (c) temper pulse, and (d) recrystallization pulse.

in VDA 239-100 [28]. RSW was carried out on a Nimak MFDC-1000 Hz pedestal type welding machine, equipped with an AutoSpatz regulator that delivered a constant current. F1-16-20-6 electrodes with a force of 4.5 kN were used, as recommended in VDEh SEP1220-2 [29]. The present study compares samples welded with four different welding sequences, as illustrated in Fig. 1. Prior to the first pulse, a squeeze time of 600 ms was chosen and the hold time after the final pulse was 300 ms. The conventional single pulse is illustrated in Fig. 1a. It consists of a 380 ms lasting pulse with a current of 5.5 kA, which is the current just high enough to produce a FZ that fulfills the quality criterion of a minimum diameter of $4*\sqrt{t}$, where t is the sheet thickness. This is the absolute lower limit of current, which is well below the splashing limit of about 6.8 kA for the single pulse weld. This current was chosen for the first pulse of every sequence. The welding time was prolonged to 810 ms for the extended single pulse weld (Fig. 1b). Figure 1c represents a double pulse weld, where a 380 ms lasting temper pulse with a current of 4.5 kA was added after a cooling time of 1000 ms. Figure 1d illustrates a double pulse weld with a recrystallization pulse of the same time and current as the first pulse after a cooling time of 100 ms.

For light optical microscope (LOM) analyses, cross-sections were ground, polished and finally etched for two minutes with a mixture of 100 ml of cold saturated picric acid, 1 g sodium dodecylbenzenesulfonate and two drops of hydrochloric acid at room temperature. LOM images were taken with an M1M Imager equipped with an AxioCam MRc5 camera, both from Zeiss.

Electron backscatter diffraction (EBSD) measurements were obtained on a scanning electron microscope,

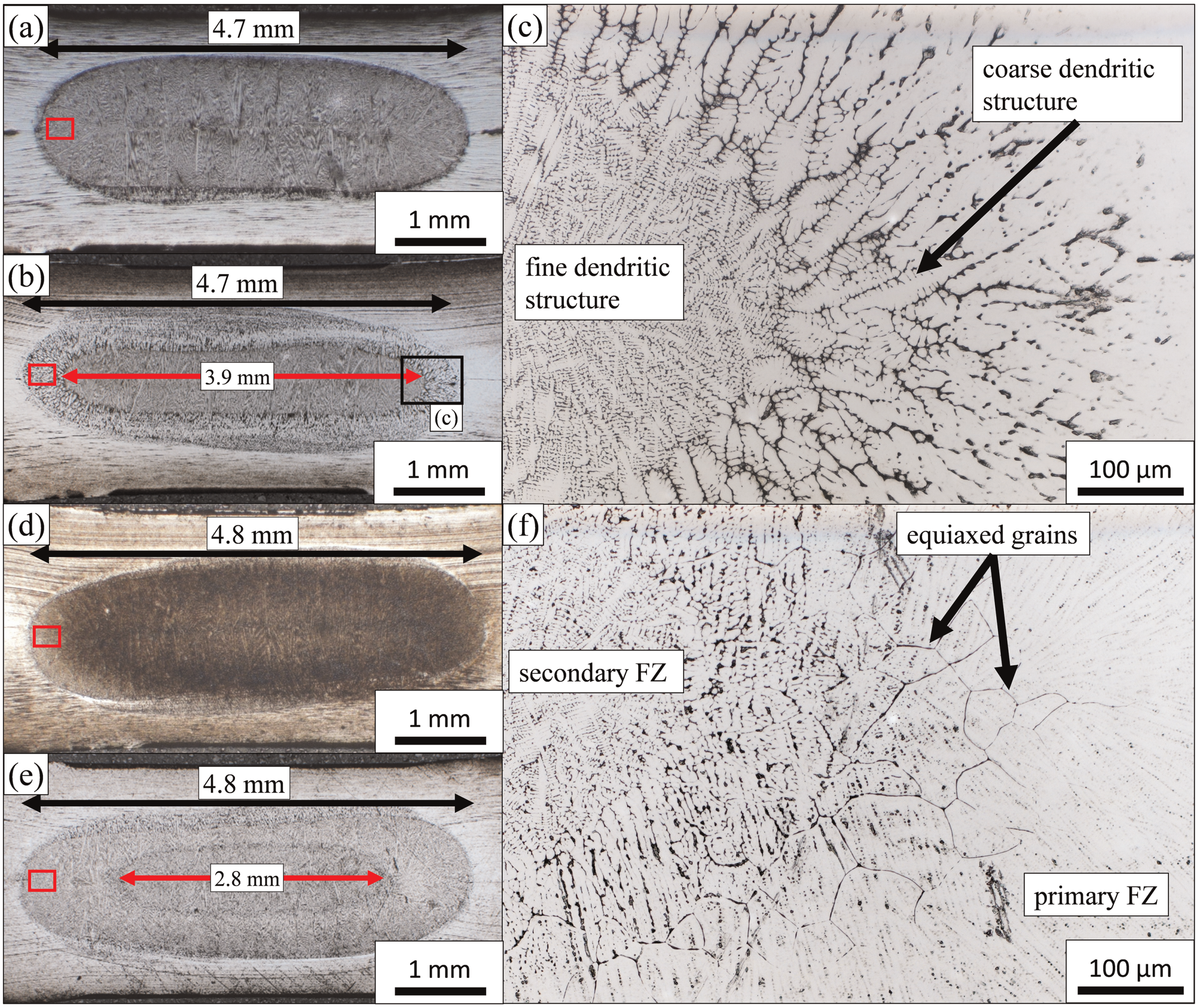

Fig. 2. LOM micrographs of cross-sections welded with the (a) conventional single pulse, (b,c) extended single pulse, (d) temper pulse, and (e,f) recrystallization pulse. The red boxes in (a), (b), (d) and (e) mark the areas where the EBSD measurements were conducted.

VERSA 3D from Thermo Fisher Scientific, equipped with an EDAX Hikari XP EBSD system operating at 20 kV. The working distance was 15 mm and the step size 250 nm. The sample preparation additionally included a final polishing step with an OPU suspension for several minutes to obtain a deformation-free surface. For data evaluation, the software package OIM Analysis 7 from EDAX was used. Grain confidence standardization and grain dilation clean-ups were carried out and data points with a confidence index below 0.1 were disregarded. To reconstruct the PAG boundaries, the ARPGE software package was used [30].

Hardness mappings were carried out with a Qness Q60A+ fully automatic micro hardness tester. The distance between the indents was 150 µm, the load 300 g and the dwell time 10 s.

The mechanical properties of the welds were determined by standard CTS tests performed with a cross-head speed of 10 mm min^{-1} on 150 × 50 mm^2 samples. The mechanical performance was evaluated by means of the maximum force, $F_{\max}$, and the pullout ratio, measured with a caliper after failure. The results represent the average of ten tests.

3. Results

3.1. Light optical microscopy

The influence of the different welding sequences on the microstructure was assessed based on LOM images of the cross-sections etched with picric acid, which are depicted in Fig. 2. The FZ of the conventional single pulse weld (Fig. 2a) shows a typical solidification structure with the dendrites oriented alongside the maximum heat dissipation. The shape of the FZ is rather elliptical with a width of 4.7 mm, indicated by the black arrow. This is in good agreement with the calculated minimum FZ size according to the quality criterion of $4*\sqrt{t}$. However, due to the fact that the cross-sections do not always run perfectly through the center of the weld because of inaccuracies during the sample

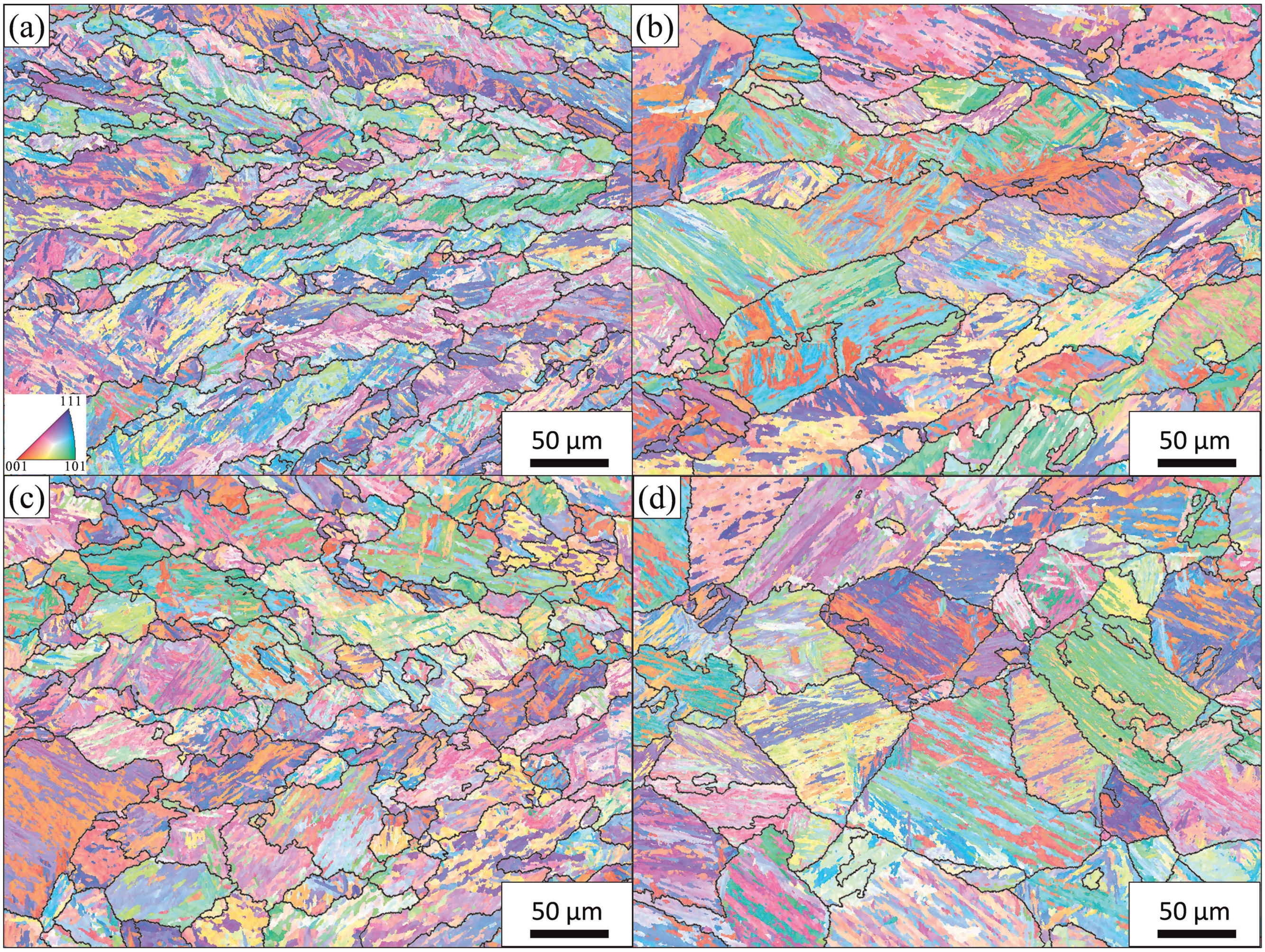

Fig. 3. IPF maps of the outer FZ of the (a) conventional single pulse, (b) extended single pulse, (c) temper pulse, and (d) recrystallization pulse weld. The regions where the scans were taken are marked with red boxes in Fig. 2. The reconstructed PAGs are highlighted with bold black lines.

preparation, especially during cutting, the size of the FZ was additionally determined on tested samples which led to the same results. By extending the welding time to 810 ms the overall size of the FZ does not increase significantly, as shown by the black arrow in Fig. 2b, but can be subdivided into two zones. The inner zone, indicated by the red arrow, consists of fine dendrites and is surrounded by a zone with coarser dendrites, as can be derived from the detailed image in Fig. 2c. The width of this coarse zone is a few hundred micrometers. Moreover, the shape of the nugget is not as well defined compared to the conventional single pulse weld. By adding a temper pulse, the size of the FZ again does not increase remarkably, as shown by the black arrow in Fig. 2d, and the shape of the FZ is elliptical. The FZ of the sample welded with a recrystallization pulse is also not enlarged significantly and can be subdivided into two zones (Fig. 2e). The inner zone represents the secondary weld nugget (red arrow) and the primary FZ is indicated by the black arrow. The outer part of the primary FZ undergoes an in-process recrystallization heat treatment during the second pulse. The width of the recrystallized zone is approximately 1 mm on both sides. At the transition zone between the primary and the secondary FZ the etchant reveals the grain boundaries of equiaxed grains, as illustrated in Fig. 2f.

3.2. Electron backscatter diffraction

In order to evaluate the effect of the various welding sequences on the microstructural features of the martensite, EBSD measurements were conducted at the edge of the FZ, as indicated by the red boxes in Fig. 2a, b, d and e. The inverse pole figure (IPF) maps are illustrated in Fig. 3, where the reconstructed PAG boundaries are highlighted with bold black lines. The PAGs of the single pulse weld exhibit a typical cast-like structure with elongated grains

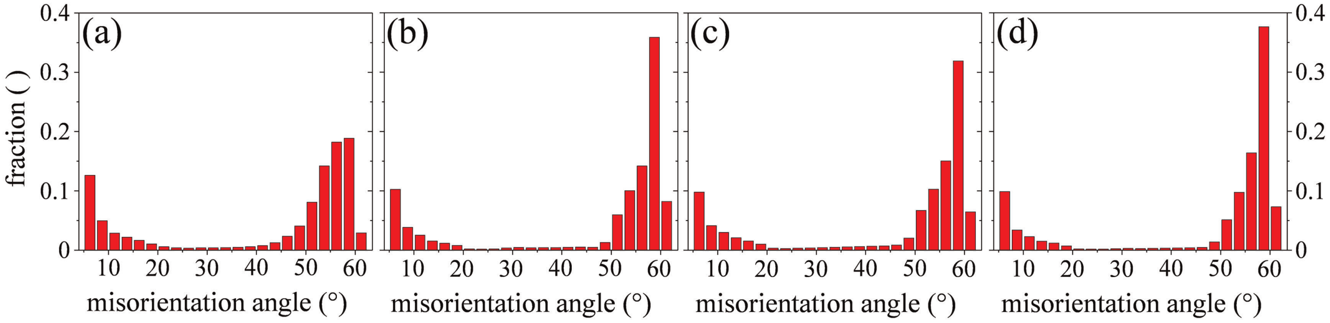

Fig. 4. The misorientation distribution corresponding to the IPF maps depicted in Fig. 3 for the (a) conventional single pulse, (b) extended single pulse, (c) temper pulse, and (d) recrystallization pulse weld.

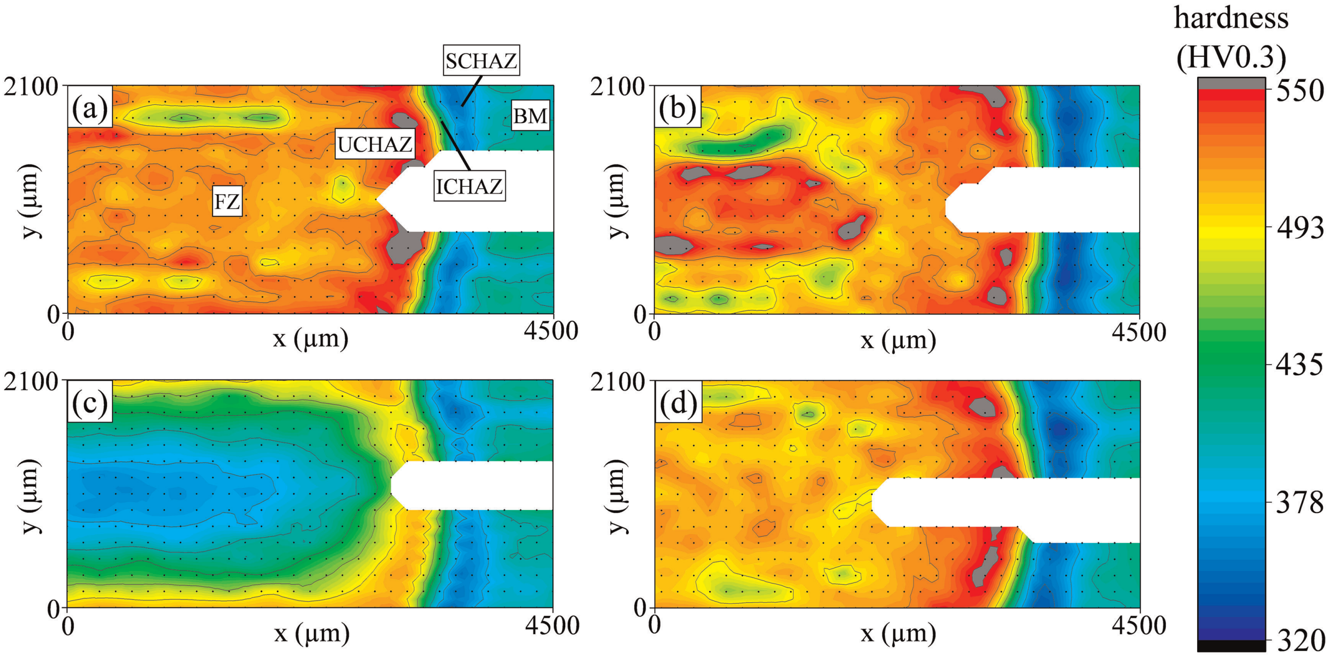

Fig. 5. Hardness mappings of the (a) conventional single pulse, (b) extended single pulse, (c) temper pulse, and (d) recrystallization pulse weld.

that are oriented alongside the maximum heat dissipation, as Fig. 3a illustrates. The corresponding misorientation distribution of the martensitic microstructure is depicted in Fig. 4a. An extended welding time leads to a distinctive coarsening of the PAGs, while the directional solidification structure is maintained, as can be seen in Fig. 3b. The fraction of high angle grain boundaries, especially with a misorientation near 60°, increases significantly while the fraction of low angle grain boundaries decreases, as illustrated in Fig. 4b. Figure 3c shows that the elongation of the PAGs diminishes. The misorientation distribution, depicted in Fig. 4c, looks similar to the distribution of the extended pulse weld (Fig. 4b) even though the peak near 60° is not as pronounced. The PAGs of the outer FZ of the recrystallization pulse weld, illustrated in Fig. 3d, seem to be coarser compared to the single pulse weld (Fig. 3a) and the cast-like structure with the elongated grains completely disappeared. Figure 4d reveals that a high fraction of 0.37 has a grain boundary misorientation angle of near 60°.

3.3. Hardness mappings

Hardness maps of the FZ and HAZ for all welding sequences are depicted in Fig. 5. The emerging zones are illustrated by means of the single pulse weld in Fig. 5a. A detailed definition and characterization of the zones in a resistance spot weld TBF steel can be found in a preliminary investigation [24]. The hardness increase of the conventional single pulse weld is strongly pronounced (Fig. 5a). The initial hardness of the base metal (BM) of 400 HV rises to over 500 HV in the FZ and reaches a maximum of 550 HV in the UCHAZ. The inter-critical heat affected zone (ICHAZ) shows a similar hardness to the BM. Because of tempering of the BM, the hardness in the SCHAZ drops to 370 HV. An extended welding time leads to an even harder inner part of the FZ (550 HV) surrounded by a slightly softer layer, as depicted in Fig. 5b. The SCHAZ is widened and at 320 HV the hardness drop is more pronounced. An implemented temper pulse softens the FZ and parts of the UCHAZ extensively, as shown in Fig. 5c. The hardness of the inner part of the FZ is approximately 370 HV and rises from the inside out reaching a maximum of 500 HV in the outer part of the UCHAZ. Softening of the SCHAZ is similar to the conventional single pulse. A recrystallization pulse again softens the SCHAZ but does not alter the hardness of the other zones significantly, as shown in Fig. 5d.

3.4. Cross tension strength tests

In order to evaluate the influence of the various welding sequences on the mechanical performance of the welds, CTS tests were carried out. The mechanical performance of the samples is hereinafter represented by the maximum force, $F_{\max}$, and the failure mode which is quantified by means of the pullout ratio in percent. A fraction of pullout of 0% represents an interfacial failure (IF) and a fraction of pullout of 100% represents a pullout failure (PF). Values between these limits represent a partially interfacial failue (PIF). As Fig. 6a shows, the single pulse welds bear an average load of 4.0 kN and the failure can be classified as PIF with a pullout ratio of 30%. By extending the welding time to 810 ms the average force slightly increases to 4.7 kN with an average pullout ratio of 73%. With 8.3 kN the temper pulse samples bear significantly higher loads than the single pulse samples. The pullout ratio is 55%. For the recrystallization pulse the maximum force is 7.1 kN with a pullout ratio of 72%. Representative load–displacement curves for each welding sequence are depicted in Fig. 6b. The curve for the single pulse (black) and the temper pulse weld (blue) drops abruptly to zero after reaching the maximum force, while it gradually drops for the extended pulse (red) and the recrystallization pulse weld (green).

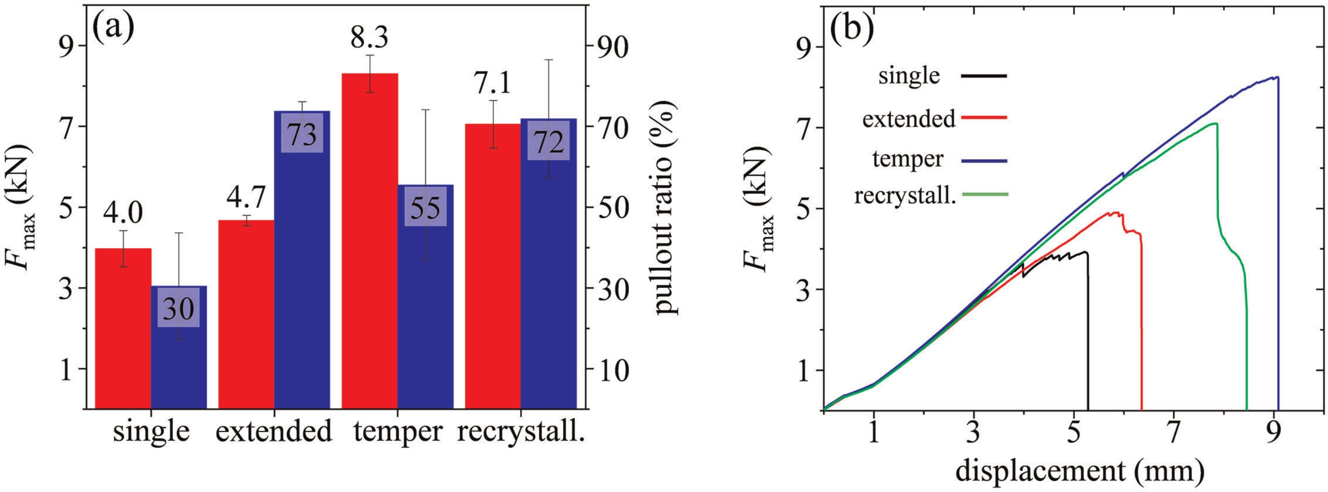

Fig. 6. (a) Average maximum force and pullout ratio during CTS tests (n = 10), and (b) representative load displacement curves of the samples welded with different sequences.

4. Discussion

The aim of the present work was to compare different approaches to improve the mechanical performance of a resistance spot welded 1 200 MPa TBF steel. The mechanical performance of the single pulse weld is poor, as the average F_{max} of 4.0 kN and the PIF failure mode with a low average pullout ratio of 30 % (Fig. 6) indicate. Generally, a larger weld nugget provides a broader load bearing area, which results in a higher F_{max} at a given strength. Since the selected current is well below the splashing limit of 6.8 kA, it would be possible to increase the single pulse current to get a larger nugget, but the aim of this work was to compare the mechanical properties at the absolute lower limit of the welding current. Literature suggests that the FZ size can also be enlarged with an extended welding time, especially at lower current levels, while this effect diminishes at higher currents due to the risk of expulsion [14–16]. In addition to the increase of the bearable load during mechanical testing, the shift of the failure mode from IF to PF was reported for several steel grades due to an enlarged FZ [14–17]. Consequently, the first approach was to increase the heat input by extending the welding time and potentially enlarge the FZ. While F_{max} during the CTS test only increases slightly to 4.7 kN for the TBF steel under investigation, the failure mode due to the extended welding time improves significantly to a pullout ratio of 73 %, as can be seen in Fig. 6a. This improved failure mode can also be derived from the load–displacement curve in Fig. 6b because it gradually drops to zero, which indicates that the crack arrests. However, as Fig. 2b indicates, the FZ is not enlarged due to the extended welding time. Consequently, the improvement of the mechanical performance has to be attributed to another phenomenon. As Fig. 2b illustrates, the appearance of the outer FZ differs from the conventional single pulse weld (Fig. 2a). The magnified image in Fig. 2c shows that there is an outer FZ of a few hundred microns that consists of a much coarser dendritic microstructure than the inner FZ. Since nugget growth in the lateral direction seems to be finished after a conventional single pulse, this coarse zone must evolve during the additional 430 ms due to a slower solidification rate resulting from the interplay of heat generation on the one hand and heat extraction from the cooled electrodes on the other hand, as suggested by Krajcarz et al. [31]. The inner FZ stays liquid and solidifies rapidly during the final cooling step. Consequently, the inner FZ is finer and noticeably harder than the more slowly solidified outer FZ, as Fig. 5b shows. The EBSD results in Fig. 3b confirm that the PAGs of this zone are much coarser compared to the PAGs of the conventional single pulse weld in Fig. 3a, while the cast-like structure is still present. Furthermore, the extension of the welding pulse, and therefore a greater heat input, leads to a significant increase of the high grain boundaries near 60°, as the comparison of Fig. 4b and Fig. 4a reveals. The increase in the toughness of the weld of a multi-phase pipeline steel was attributed to the increased number of high angle grain boundaries due to an increased and optimized heat input by You et al. [32]. Moreover, Chabok et al. [8] investigated the crack path through the recrystallized zone of a double pulse resistance spot welded DP1000 steel and observed that the crack is predominantly deflected at high angle grain boundaries with a misorientation of over 50°. Consequently, the high number of high angle grain boundaries may be responsible for crack deflection at the outer FZ leading to a more favorable failure mode for the samples welded with an extended single pulse. Additionally, the softening of the SCHAZ is more pronounced compared to the conventional single pulse weld (Fig. 5a), a circumstance that was reported to be a key reason for the improvement of the mechanical properties of a double pulse welded high strength dual-phase steel [8].

In general, the poor mechanical properties of third generation AHSS spot welds can mainly be attributed to the combination of a cast-like structure and the hardness increase in the FZ due to the relatively high alloying content [4]. Hence, the goal of both double pulsing approaches is to eliminate one of those factors. A tempering heat treatment of the welds is generally a capable way to improve the mechanical performance [18]. In this work an in-process tempering heat treatment was achieved by means of a second pulse subsequent to a long cooling time. As Fig. 5c illustrates, the hardness of the FZ decreases to a hardness similar to the BM of about 400 HV at the edge of the FZ because of the second pulse. In contrast, the softening of UCHAZ is not as pronounced and this zone is therefore more rigid than the tempered FZ. As the bearable load strongly increases to 8.3 kN with an average pullout ratio of 55 % (Fig. 6), this combination of a soft and therefore tough FZ and a still hard and therefore strong UCHAZ seems to be ideal in terms of the mechanical performance, as suggested in a previous work [24]. However, the parameters have to be chosen very carefully. On the one hand, the second pulse has to be strong enough to enable tempering. On the other hand, the heat input of the second pulse must not be too high so that re-austenitization of the FZ and unwanted excessive tempering of the UCHAZ are avoided [24]. The tempering leads to an increase in the fraction of high angle grain boundaries (Fig. 4c), which is presumed to promote crack deflection, as discussed above. The drawback of this approach is the more than doubled process time compared to the conventional single pulse weld.

The concept of the recrystallization pulse relies on a short cooling time after the first pulse, where solidification of the FZ takes place. By an immediately following second pulse of the same current, the inner part of the FZ re-melts and the outer part recrystallizes during the second pulse. The LOM image of the cross-section (Fig. 2e) shows that the FZ can indeed be subdivided into the secondary FZ that re-melted during the second pulse and the surrounding part of the primary FZ that underwent the desired heat treatment. The etching reveals a non-dendritic grain structure at the transition zone between secondary and primary FZ, as illustrated in Fig. 2e. Moreover, as the highlighted PAG boundaries in Fig. 3d show, the recrystallization leads to equiaxed PAGs close to the pre-crack. The equiaxed shape of the PAGs is assumed to be one of the main reasons for enhanced mechanical properties of double pulse welded AHSS steel sheets as it impedes the fracture path through the nugget centerline [10, 22]. This was also observed in the framework of the present research. Moreover, the recrystallization modifies the arrangement of the grain boundaries, resulting in a significant increase of high angle grain boundaries near 60°, as shown in Fig. 4d. The hardness mapping (Fig. 5d) illustrates that the softening of the SCHAZ is more pronounced compared to the single pulse weld, which is seen as beneficial for the mechanical properties [8], as mentioned above. However, a softening of the recrystallized zone, as reported in literature [8, 9], was not observed. Figure 3d indicates that the recrystallization pulse also leads to a coarsening of the microstructure at the edge of the FZ, which is attributed to grain growth due to the high temperature during the second pulse. This seems to be contrary to the results of Sajjadi-Nikoo et al. [21] and Eftekharimilani et al. [11], which both reported grain refinement as a result of double pulsing. This different grain growth behavior can be attributed to the lower second pulse currents they applied in their studies. In addition, Sajjadi-Nikoo et al. [21], applied a longer cooling time between the pulses, which resulted in lower heat input and therefore inhibited grain growth compared to the present work. At a higher second pulse current, Eftekharimilani et al. [11] also observed grain growth due to the higher temperature. Besides the modification of the morphology of the PAGs and the softening of the SCHAZ, the homogenization of phosphorus due to the second pulse is considered as another main benefit. A correlation between improved mechanical properties and a homogenization of phosphorus, detected via electron probe microscopy analyses (EPMA), has been established for third generation AHSS welds [11, 13]. Within the framework of this study, EPMA measurements were conducted as well, without observing noteworthy differences in the phosphorus distribution. Due to the recrystallization pulse the mechanical performance during the CTS test is improved significantly, as shown in Fig. 6. The maximum force reaches 7.1 kN with a pullout ratio of 72 %. Consequently, the mechanical performance is distinctively enhanced compared to the single pulse welds, with the advantage of a much shorter process time compared to the temper pulse sequence.

5. Conclusions

In the present work three different approaches to improve the mechanical performance, according to CTS testing, of a resistance spot welded 1 200 MPa TBF steel were evaluated and compared with a conventional single pulse weld. The following conclusions can be drawn:

1. The conventional single pulse weld possesses poor mechanical properties during the CTS test, with an $F_{\max}$ of 4.0 kN and an unfavorable failure mode with a pullout ratio of 30 %. Its outer FZ consists of elongated PAGs that are oriented alongside the maximum heat dissipation.
2. An extended welding time does not enlarge the FZ but leads to a distinctive coarsening of the PAGs of the outer FZ and to an increase in the fraction of the high angle grain boundaries near 60°. The mechanical performance regarding the maximum force during the CTS test only improves slightly to 4.7 kN, but the failure mode, quantified by the pullout ratio, improves to 73 % which is mainly attributed to the increased fraction of high angle grain boundaries.
3. Double pulsing with a low current temper pulse following an extended cooling time of 1 000 ms between the pulses leads to pronounced softening of the FZ and parts of the UCHAZ due to tempering which results in a high $F_{\max}$ of 8.1 kN. A refinement of the microstructure and an increase in the fraction of high angle grain boundaries near 60° at the edge of the FZ can be observed which leads to an average pullout ratio of 55 %.
4. Double pulsing with a recrystallization pulse of the same current as the first pulse following a very short cooling time of 100 ms successfully recrystallizes the edge of the FZ. The martensitic microstructure is much coarser but the PAGs are equiaxed and the fraction of high angle grain boundaries near 60° increases significantly. The resulting crack deflection results in an improved mechanical performance during the CTS test to a maximum force of 7.1 kN with an average pullout ratio of 71 %.

Funding of the Austrian BMK (846933) in the framework of the program “Production of the future” and the “BMK Professorship for Industry” is gratefully acknowledged.

References

[1] D.K. Matlock, J.G. Speer, in: A. Haldar, S. Suwas, D. Bhattacharjee (Eds.), Microstructure and Texture in Steels, Springer London, London (2009), 185. DOI:10.1007/978-1-84882-454-6_11
[2] N. Fonstein: Advanced High Strength Sheet Steels, Springer International Publishing, New York (2015). DOI:10.1007/978-3-319-19165-2
[3] C. Hofer, H. Leitner, F. Winkelhofer, H. Clemens, S. Primig: Mater. Charact. 102 (2015) 85. DOI:10.1016/j.matchar.2015.02.020
[4] M. Pouranvari, S.P.H. Marashi: Sci. Technol. Weld. Joining 18 (2013) 361. DOI:10.1179/1362171813Y.0000000120
[5] M. Amirthalingam, E.M. van der Aa, C. Kwakernaak, M.J.M. Hermans, I.M. Richardson: Weld. World 59 (2015) 743. DOI:10.1007/s40194-015-0250-3
[6] N.J. Den Uijl, S. Smith (Eds.), 4th International Seminar on Advances in Resistance Welding Resistance Spot Welding of Advanced High Strength Steels for the Automotive Industry Wels, Austria (2006) 30.
[7] M. Pouranvari, S.P.H. Marashi: Sci. Technol. Weld. Joining 15 (2013) 149. DOI:10.1179/136217109X12590746472535
[8] A. Chabok, E. van der Aa, J.T.M. de Hosson, Y.T. Pei: Mater. Des. 124 (2017) 171. DOI:10.1016/j.matdes.2017.03.070
[9] A. Chabok, E. van der Aa, I. Basu, J. de Hosson, Y. Pei: Sci. Technol. Weld. Joining 23 (2018) 649. DOI:10.1080/13621718.2018.1452875
[10] P. Eftekharimilani, E.M. van der Aa, M.J.M. Hermans, I.M. Richardson: Sci. Technol. Weld. Joining 22 (2017) 545. DOI:10.1080/13621718.2016.1274848
[11] P. Eftekharimilani, E.M. van der Aa, M.J.M. Hermans, I.M. Richardson: Weld. World. 61 (2017) 691. DOI:10.1007/s40194-017-0459-4
[12] X.D. Liu, Y.B. Xu, R.D.K. Misra, F. Peng, Y. Wang, Y.B. Du: J. Mater. 263 (2019) 186. DOI:10.1016/j.jmatprotec.2018.08.018
[13] C. Sawanishi, T. Ogura, K. Taniguchi, R. Ikeda, K. Oi, K. Yasuda, A. Hirose: Sci. Technol. Weld. Joining 19 (2013) 52. DOI:10.1179/1362171813Y.0000000165

[14] M. Pouranvari, H.R. Asgari, S.M. Mosavizadch, P.H. Marashi, M. Goodarzi: Sci. Technol. Weld. Joining 12 (2013) 217. DOI:10.1179/174329307X164409

[15] M. Pouranvari, S.P.H. Marashi: Mater. Sci. Technol. 26 (2010) 1137. DOI:10.1179/174328409X459301

[16] S. Aslanlar, A. Ogur, U. Ozsarac, E. Ilhan: Mater. Des. 29 (2008) 1427. DOI:10.1016/j.matdes.2007.09.004

[17] X. Sun, E.V. Stephens, M.A. Khaleel: Weld. J. -New York- 86 (2007) 18.

[18] T.B. Hilditch, J.G. Speer, D.K. Matlock: Mater. Des. 28 (2007) 2566. DOI:10.1016/j.matdes.2006.10.019

[19] G. Shi, S.A. Westgate (Eds.), paper for 1st nternational onference of the High Strength Steel (2005) 1.

[20] M. Mimer, L.E. Svensson, R. Johansson: Weld. World 48 (2004) 14. DOI:10.1007/BF03266421

[21] S. Sajjadi-Nikoo, M. Pouranvari, A. Abedi, A.A. Ghaderi: Sci. Technol. Weld. Joining 23 (2018) 71. DOI:10.1080/13621718.2017.1323174

[22] V.B. Hernandez, Y. Okita, Y. Zhou: impulse 91 (2012) 278.

[23] A.R. Jahandideh, M. Hamedi, S.A. Mansourzadeh, A. Rahi: Sci. Technol. Weld. Joining 16 (2011) 669. DOI:10.1179/1362171811Y.0000000053

[24] M. Stadler, M. Gruber, R. Schnitzer, C. Hofer: Weld. World 64 (2020) 335. DOI:10.1007/s40194-019-00835-9

[25] G. Park, K. Kim, S. Uhm, C. Lee: Mater. Sci. Eng. A 766 (2019) 138401. DOI:10.1016/j.msea.2019.138401

[26] C. Hofer, F. Winkelhofer, H. Clemens, S. Primig: Mater. Sci. Eng. A 664 (2016) 236. DOI:10.1016/j.msea.2016.04.005

[27] C. Hofer, S. Primig, H. Clemens, F. Winkelhofer, R. Schnitzer: Adv. Eng. Mater. 19 (2017) 1600658. DOI:10.1002/adem.201600658

[28] Verband Der Automobilindustrie E.V. (2016) VDA 239–100: Flacherzeugnisse aus Stahl zur Kaltumformung.

[29] Stahl-Eisen-Prüfblätter (SEP) des Stahlinstituts VDEh SEP 1220–2: Testing and documentation guideline for the joinability of thin sheet of steel-Part 2: Resistance Spot Welding.

[30] C. Cayron: J. Appl. Crystallogr. 40 (2007) 1183. DOI:10.1107/S0021889807048777

[31] F. Krajcarz, A.-F. Gourgues-Lorenzon, E. Lucas: Scr. Mater. 120 (2016) 98. DOI:10.1016/j.scriptamat.2016.04.011

[32] Y. You, C. Shang, N. Wenjin, S. Subramanian: Mater. Sci. Eng. A 558 (2012) 692. DOI:10.1016/j.msea.2012.08.077

(Received June 24, 2020; accepted January 2, 2021; online since March 22, 2021)

Correspondence address

Manfred Stadler
Department of Materials Science
Montanuniversität Leoben
Franz-Josef-Strasse 18
Leoben 8700
Austria
Tel.: 0043/38424024268
E-mail: manfred.stadler@unileoben.ac.at

Bibliography

DOI 10.1515/ijmr-2020-7962
Int. J. Mater. Res. 112 (2021) 4; page 262–270

ISSN 1862-5282 · e-ISSN 2195-8556

Paper III

M. Stadler, R. Schnitzer, M. Gruber, K. Steineder, C. Hofer

Influence of the cooling time on the microstructural evolution and mechanical performance of a double pulse resistance spot welded medium-Mn steel

Metals 11 (2021) 270

metals

Article

Influence of the Cooling Time on the Microstructural Evolution and Mechanical Performance of a Double Pulse Resistance Spot Welded Medium-Mn Steel

Manfred Stadler [1],*, Ronald Schnitzer [1], Martin Gruber [2], Katharina Steineder [2] and Christina Hofer [1]

[1] Department of Materials Science, Montanuniversität Leoben, Franz-Josef-Strasse 18, 8700 Leoben, Austria; ronald.schnitzer@unileoben.ac.at (R.S.); christina.hofer@unileoben.ac.at (C.H.)
[2] voestalpine Stahl GmbH, voestalpine-Strasse 3, 4020 Linz, Austria; martin.gruber@voestalpine.com (M.G.); katharina.steineder@voestalpine.com (K.S.)
* Correspondence: manfred.stadler@unileoben.ac.at; Tel.: +43-3842-402-4268

Abstract: In the present work, the influence of the cooling time on the mechanical performance, hardness, and microstructural features of a double pulse resistance spot welded medium-Mn steel are investigated. Curves of the electrical resistance throughout the welding revealed that the cooling time strongly influences the heat generation during the second pulse. A second pulse after a short cooling time re-melts the center, and heat treats the edge of the primary fusion zone. This desired in-process heat treatment leads to a modification of the cast-like martensitic structure by recrystallization illustrated by electron backscatter diffraction measurements and to a homogenization of manganese segregations, visualized by energy-dispersive X-ray spectroscopy, which results in an enhanced mechanical performance during the cross tension strength test. In contrast, during excessively long cooling times, the resistance drops to a level where the heat generation due to the second pulse is too low to sufficiently re-heat the edge of the primary FZ. As a consequence, the signs of recrystallization disappear, and the manganese segregations are still present at the edge of the fusion zone, which leads to a deterioration of the mechanical properties.

Keywords: advanced high strength steels; AHSS; medium-Mn steel; resistance spot welding; double pulsing; dynamic resistance curves

check for updates

Citation: Stadler, M.; Schnitzer, R.; Gruber, M.; Steineder, K.; Hofer, C. Influence of the Cooling Time on the Microstructural Evolution and Mechanical Performance of a Double Pulse Resistance Spot Welded Medium-Mn Steel. *Metals* **2021**, *11*, 270. https://doi.org/10.3390/met11020270

Academic Editors: C. Issac Garcia and Kornél Májlinger

Received: 14 December 2020
Accepted: 2 February 2021
Published: 5 February 2021

1. Introduction

As a representative of the third generation of advanced high strength steels (AHSS), medium-Mn steels, with an increased but still moderate amount of manganese of 4–10 wt% and a carbon content of 0.2 wt% or less, are considered suitable to fulfill the requirements for body components in the automotive industry [1–4]. First introduced in 1972 by Miller [5], research on this steel grade has been intensified in recent years [4,6–9]. Their superior mechanical properties are achieved by a ferritic microstructure with a high amount of retained austenite of usually more than 30%, which is stabilized by manganese enrichment at intercritical annealing [4,6,8,10]. A high fraction of retained austenite is essential to combine high strength and ductility by means of the transformation-induced plasticity (TRIP) effect [8,9].

Because of the high operating speed and the suitability for automation, resistance spot welding (RSW) is the dominant technology for sheet metal joining in the automotive industry [11], and therefore, research regarding the weldability of medium-Mn steels is decisive. However, only few related studies have been published so far [12–15]. Due to the rapid cooling combined with the relatively high alloying content of medium-Mn steels, they tend to form a hard and brittle martensitic fusion zone (FZ), which leads to a poor tensile-shear strength of the welds [12] and to insufficient mechanical properties during the cross-tension strength (CTS) test with low maximum force and an interfacial failure (IF) mode [13]. The failure mode changes to a pullout failure (PF) for dissimilar resistance spot weldments of a medium-Mn and dual phase steel, with the crack propagating through the brittle, martensitic coarse-grained heat-affected zone (CGHAZ) of the medium-Mn steel. This zone has a significantly lowered content of retained austenite compared to the base metal [13]. However, the brittleness of the CGHAZ could be reduced by nano-scale austenite reversion during a paint baking heat treatment, which led to enhanced mechanical properties of the welds [14]. Another work focused on the softening of the CGHAZ by means of various thermo-mechanically simulated in-situ tempering heat treatment cycles. Again the nano-scale austenite reversion led to an increase of the ductility of this zone and to the transition from a brittle to a ductile fracture [15].

A widely accepted approach to improve the mechanical performance of third generation AHSS welds is to add an additional pulse after the main pulse to carry out an in-process heat treatment of the welds, also known as double pulsing [16–22]. In previous works [22,23], the authors examined the microstructural evolution and the mechanical performance of the FZ and heat-affected zone (HAZ) of a double pulse welded 1.2 GPa TRIP-aided bainitic ferrite (TBF) steel. It was shown that a low current second pulse after a very long cooling time between the pulses tempers, and therefore, softens the weldment, while a high current second pulse after a short cooling time, hereinafter referred to as a recrystallization pulse, recrystallizes the edge of the FZ. Due to a shorter process time, research mainly focused on the concept of the recrystallization pulse in recent years [16–19,21], although both double pulsing concepts are capable of improving the mechanical performance of AHSS spot welds [23]. During the second pulse, the cast-like structure at the edge of the FZ recrystallizes, resulting in more equiaxed prior austenite grains (PAGs) and in a refinement of the martensitic blocks, which improves the toughness due to enhanced crack deflection [17]. Further, the second pulse homogenizes the segregations of phosphorus and also manganese in the FZ, and therefore, diminishes the risk of intergranular failure [18]. Chabok et al. [16] attributed the improved mechanical performance of a double pulse welded DP1000 dual-phase steel to the lowered residual strain at the edge of the FZ and the increased number of high angle grain boundaries in the upper critical heat-affected zone (UCHAZ), which is also assumed to increase the toughness.

Consequently, double pulsing might also represent a promising approach to overcome the poor weldability of medium-Mn steels. However, the influence of the significantly increased manganese content compared to other representatives of the third generation AHSS has to be taken into account, and there is especially a lack of publications in the literature dealing with the exact role of the cooling time between pulses, which makes it difficult to choose the optimal parameters. The main focus of this work is, therefore, on the role of the cooling time with regard to the heat generation during the second pulse, and its influence on the microstructural features and especially the manganese distribution at the edge of the FZ and the resulting mechanical properties of a resistance spot welded medium-Mn steel, which, to our knowledge, has never been published before.

For this purpose, single and double pulse welding experiments with increasing cooling time between the pulses were performed, and the heat generation during the second pulse was evaluated based on the dynamic resistance curves. The mechanical performance of the welds was assessed by CTS tests, and hardness mappings were conducted to comprehend the influence of double pulsing with different cooling time on the hardness distribution. Picric acid etching and electron backscatter diffraction (EBSD) measurements were used to visualize the influence of the welding parameters on the microstructure. Moreover, the manganese distribution was measured via energy-dispersive X-ray spectroscopy (EDX). Combining these methods, a correlation of the cooling time between the pulses, the microstructure, and the mechanical performance is drawn.

2. Materials and Methods

A medium-Mn steel with a nominal composition of 0.1 C/6.4 Mn/0.6 Si (wt%), an aluminum content of <400 ppm, and a phosphorus and sulfur content of combined less than 120 ppm was investigated. This steel possesses a minimum tensile strength of 780 MPa with a yield strength of about 650 MPa and an elongation of about 34%. The uncoated steel sheets had a thickness of 1.18 mm. RSW was performed on a Nimak MFDC-1000 Hz pedestal type welding machine (Nimak GmbH, Wissen, Germany) equipped with an AutoSpatz regulator (Matuschek, Alsdorf, Germany) that delivered a constant current. The resulting voltage was measured at the electrode and the resulting resistance as a function of time was calculated with the adjusted current. The F1-16-20-6 electrodes operated at a clamping force of 4.0 kN as recommended in VDEh SEP1220-2 [24]. The samples in the present work were welded with a current of 4.8 kA, which is the current high enough to produce a FZ that fulfills the quality criterion of a minimum diameter of $4^{*}\sqrt{t}$, where t is the sheet thickness. This current was used for the first pulse, as well as for the second pulse. A schematic illustration of the different welding sequences is presented in Figure 1. For all welds, prior to the first pulse, a squeeze time of 600 ms was applied, the pulse time was 280 ms, and the hold time after the final pulse was 200 ms. The variable cooling time between the pulses was 20, 50, 100, 200, and 500 ms.

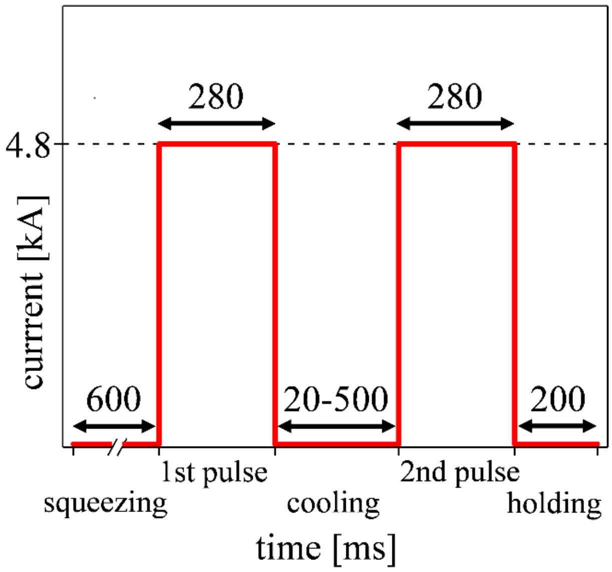

Figure 1. Schematic illustration of the welding sequence with variable cooling times.

The mechanical performance was evaluated via standard CTS tests [24] (sample size of 50 × 150 mm^2) and the results represent the average of five tests. The maximum force, F_{max}, and the pullout ratio, which is the areal fraction of the pulled-out plug to the former welded lens, were measured with a caliper after failure.

For microstructural characterization, light optical microscope (LOM) images were taken with an M1M Imager equipped with an AxioCam MRc5 camera, both from Zeiss (Oberkochen, Germany). For this purpose, cross-sections were ground, polished, and finally, etched with a mixture of cold saturated picric acid, dodecylbenzenesulfonate, and hydrochloric acid to reveal the solidification structure.

Hardness mappings were performed on a Q60A+ hardness tester from Qness (Golling, Austria). The distance between the indents was 150 µm, the load was 300 g, and the dwell time 10 s.

For the EBSD measurements, the sample preparation included final OPU suspension polishing for 10 min in order to get a deformation free surface. The measurements were performed on a scanning electron microscope (SEM) VERSA 3D from FEI (Hillsboro, OR, USA) equipped with an EDAX Hikari EBSD system operating at a working distance of 15 mm and an acceleration voltage of 20 kV. The step size of the EBSD mappings with an area of 500 × 500 μm^2 was 500 nm. The software package EDAX OIM Analysis 7 (EDAX Inc., Mahwah, NJ, USA) was used for data evaluation. The data sets were cleaned via grain dilation, and neighbor confidence index (CI) standardization clean-ups and data points with a CI of less than 0.1 were disregarded. ARPGE software package [25] was used to reconstruct the PAGs.

Energy-dispersive X-ray spectroscopy was performed at an acceleration voltage of 15 kV on a Tescan SEM of the type CLARA (Tescan, Brünn, Czech Republic) combined with the X-Max system and the Aztec software from Oxford Instruments (Abingdon, UK). Since the conventional EDX measurements only allow a qualitative statement, the numerical values of the manganese content were determined with a post-processing step by the software package but without claiming to achieve the extremely high accuracy of an EPMA system.

3. Results

3.1. *Cross-Tension Strength Tests*

The influence of the cooling time on the mechanical performance of the welds was determined with CTS tests and the results are depicted in Figure 2. The maximum force, F_{max}, and the pullout ratio hereinafter quantify the mechanical performance of the welds. A pullout ratio of 0% is referred to as an IF and a fraction of pullout of 100% represents a PF. A pullout ratio between these limits is a partial interfacial failure (PIF). The single pulse samples, referred to as "*sp*" in Figure 2, reach a F_{max} of 3.0 kN and the pullout ratio averages 26%. In contrast, the double pulse welds with relatively short cooling times of 20, 50, and 100 ms between the pulses bear significantly higher loads of 6.0, 6.3, and 5.8 kN and the pullout ratio after CTS testing is 27%, 45%, and 31%, respectively. However, it has to be stated that, for all welds, the standard deviation of the pullout ratio is relatively high. With longer cooling times of 200 and 500 ms, F_{max} decreases to 4.1 and 4.3 kN with a pullout ratio of 40% and 56%, respectively.

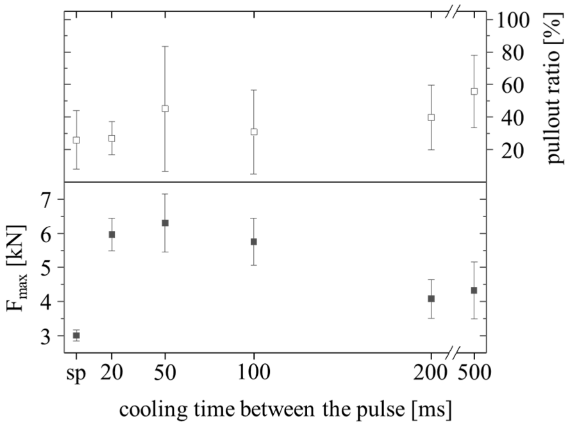

Figure 2. Average maximum force, F_{max}, and pullout ratio in CTS tests of single pulse welds (sp) compared to double pulse welds with different cooling times (n = 5).

3.2. *Light Optical Microscopy*

By means of the picric acid-etched cross-sections depicted in Figure 3, the influence of the cooling time on the evolution of the FZ during the second pulse was examined. The black arrows indicate the width of the primary and the red arrows indicate the width of the secondary FZ, which re-melts during the second pulse. The width of the FZ of the single pulse weld in Figure 3a is 4.1 mm, and therefore, slightly smaller than the nominal minimum FZ size of 4.35 mm calculated from the $4^*\sqrt{t}$ quality criterion. The black arrows in Figure 3b–f illustrate that the size of the primary FZ does not change significantly due to double pulsing. However, the size of the secondary FZ decreases with increasing cooling time. While 3.7 mm of the initial 4.2 mm are re-melted by the second pulse after a cooling time of 20 ms in Figure 3b, only 3.1 and 1.2 mm are re-melted after a cooling time of 50 and 100 ms, as shown in Figure 3c,d. After longer cooling times of 200 ms in Figure 3e and 500 ms in Figure 3f, there is no secondary FZ clearly visible.

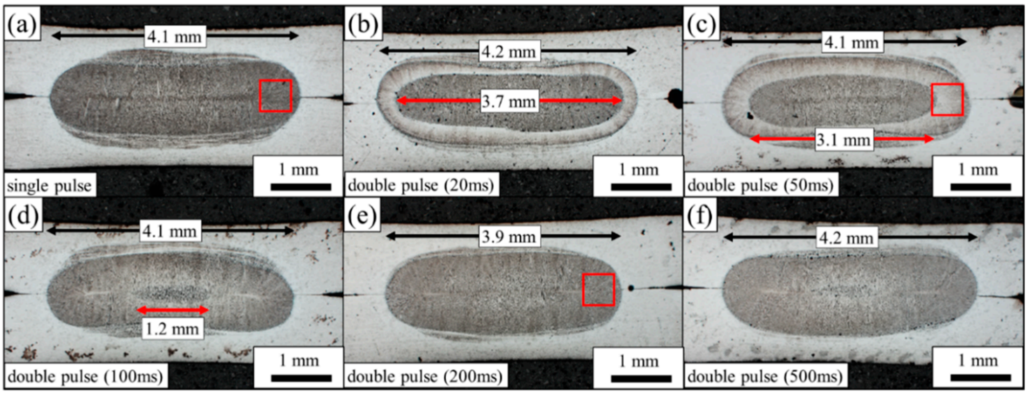

Figure 3. LOM images of the cross-sections of (**a**) single pulse weld and double pulse welds with a cooling time of (**b**) 20 ms, (**c**) 50 ms, (**d**) 100 ms, (**e**) 200 ms, and (**f**) 500 ms. The black arrows represent the width of the primary FZ and the red arrows the width of the secondary FZ, if present. The red boxes in (**a**,**c**,**e**) mark the areas where EBSD scans were taken.

3.3. Dynamic Resistance Curves

The heat generation, Q_w in joules, during resistance spot welding is based on Joule's law. Since the welding current and the welding time stay constant, the equation can be written as

$$\frac{Qw}{R(T)} = \underbrace{I^2 * t}_{const} \tag{1}$$

where I is the electrical current in amperes, $R(T)$ the temperature-dependent, and therefore, dynamic electrical resistance in ohms and t the welding time in seconds. While the electric current and the welding time are given by the operator, the dynamic resistance curve can be recorded to estimate the heat development during welding according to Equation (1). Online monitoring of the dynamic resistance is, therefore, a powerful tool in terms of process control [26–28]. In the course of the present work, the dynamic resistance curves were primarily recorded to evaluate the influence of the various cooling times on the temperature prior and the heat generation during the second pulse. The resistance curve of the single pulse weld is shown in Figure 4a. As suggested by Dickinson et al. [29], the first peak in the resistance curve represents the contact resistance, which is 250 µΩ in the case of the medium-Mn steel sheets under investigation. It breaks down within a few milliseconds to 150 µΩ, the so-called α-trough. Then the increasing temperature results in a continuous increase of the resistance, but with progressing time also in local melting, which lowers the resistance due to an increasing cross-sectional area available for the current flow. The so-called β-peak of 190 µΩ represents the point where the temperature stabilizes, and the nugget growth begins to dominate. After the β-peak, the resistance continuously decreases due to the increasing nugget size to a final resistance of 115 µΩ. The resistance curves of the second pulse after various cooling times are presented in Figure 4b–f. After a short cooling time of 20 and 50 ms, the resistance drops slightly to 100 and 90 µΩ and stays constant during the second pulse, as can be seen in Figure 4b,c. After a longer cooling time of 100 ms, the resistance is 70 µΩ at the beginning of the second pulse and rises continuously to 80 µΩ in Figure 4d. The resistance drop is even more pronounced after cooling times of 200 and 500 ms. It decreases to 40 and 30 µΩ at the beginning of the second pulse and reaches a final resistance of 70 and 60 µΩ, as can be seen in Figure 4e,f, respectively. The continuously decreasing resistance illustrates that the temperature at the beginning, and consequently the heat generation during the second pulse, decreases with longer cooling times between the pulses.

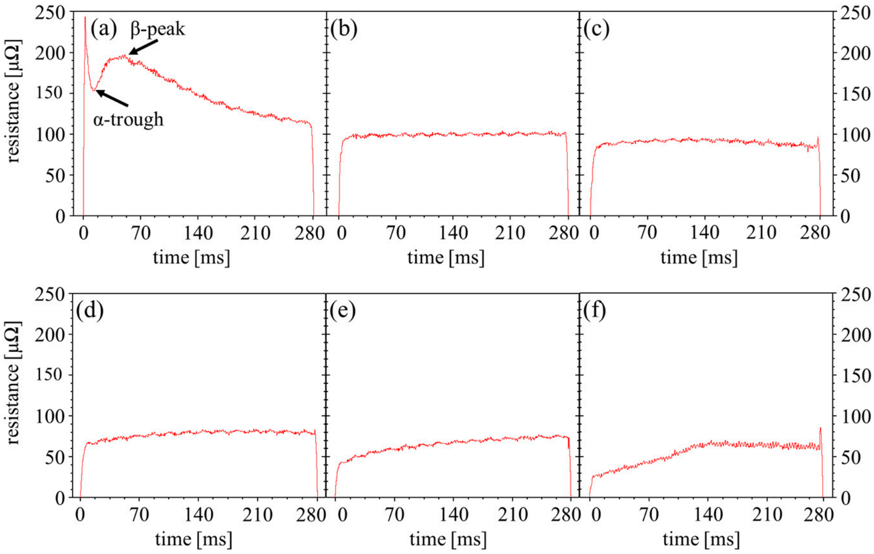

Figure 4. Dynamic resistance curves recorded during the (**a**) single pulse and the second pulse after a cooling time of (**b**) 20 ms, (**c**) 50 ms, (**d**) 100 ms, (**e**) 200 ms and (**f**) 500 ms.

3.4. Hardness Mapping

Hardness mappings with several hundred indents, as depicted in Figure 5, were conducted on representative samples to verify the effect of double pulsing on the hardness distribution of the medium-Mn steel welds. For the single pulse weld in Figure 5a the hardening of the FZ, with a hardness of 420–430 HV, is very pronounced compared to the hardness of about 280 HV of the BM. The hardness in the UCHAZ reaches up to 460 HV before dropping to 370 HV in the intercritical heat-affected zone (ICHAZ). Since the BM does not contain martensite, there is no softening of the subcritical heat-affected zone (SCHAZ). The double pulse welds with a cooling time of 50 ms in Figure 5b and 200 ms in Figure 5c show an almost identical hardness distribution, although a slight softening of about 10–20 HV can be observed in the outer regions of the FZ. Moreover, the ICHAZ after 200 ms cooling time in Figure 5c seems to be wider. The ICHAZ further broadens with a longer cooling time of 500 ms, as shown in Figure 5d. It is about twice as big as the width of the ICHAZ of the 50 ms double pulse weld in Figure 5b.

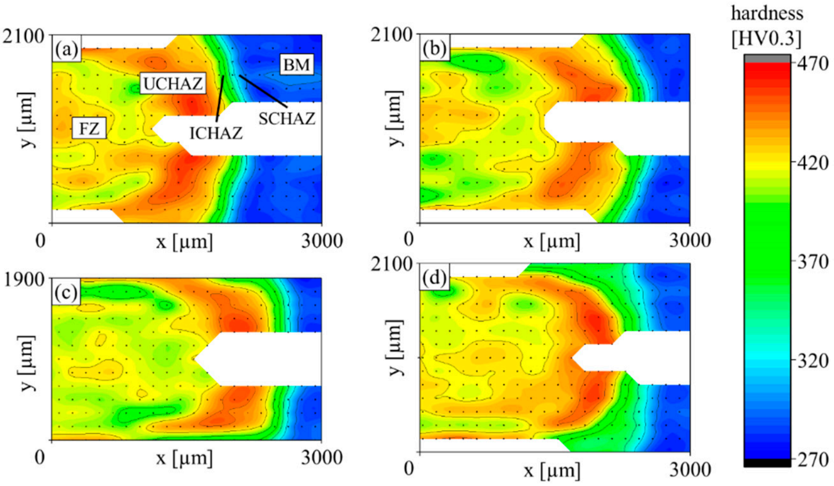

Figure 5. Hardness mappings of the (**a**) single pulse weld and double pulse weld with a cooling time of (**b**) 50 ms, (**c**) 200 ms, and (**d**) 500 ms.

3.5. Electron Backscatter Diffraction

To analyze the structure of the prior austenite grains (PAGs) at the edge of the FZ, EBSD scans of areas of 500 × 500 μm^2 of the single pulse weld and the double pulse welds with a cooling time of 50 and 200 ms were conducted, as marked by red boxes in Figure 3a,c,e. The corresponding IPF maps of the bcc phase, which represents the low carbon martensite, with the reconstructed PAGs being highlighted with bold black lines, are depicted in Figure 6. As can be seen in Figure 6a, the edge of the FZ after the single pulse consists of the typical cast-like structure with elongated PAGs oriented along the maximum heat dissipation. After a 50 ms lasting cooling time, the second pulse leads to a noticeable coarsening of the PAGs, and the elongation, especially of the PAGs in the center of the scan, diminishes in Figure 6b. By extending the cooling time to 200 ms, the PAGs are again more elongated and finer compared to the weld with a 50 ms cooling time and rather resemble the PAGs of the single pulse weld.

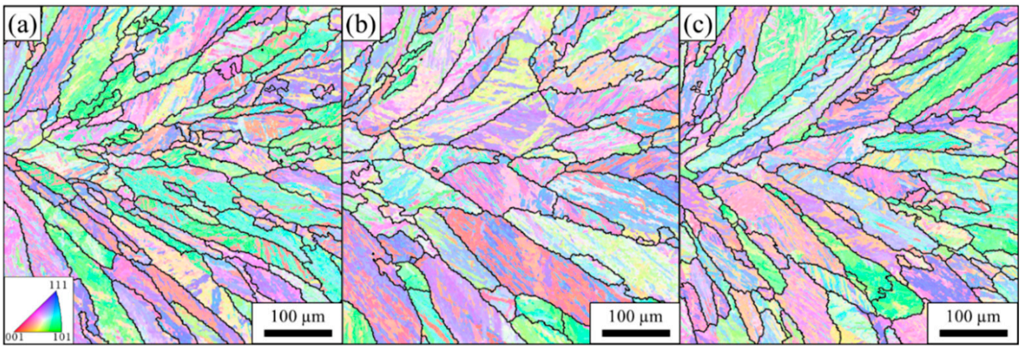

Figure 6. IPF maps of the bcc phase of the areas indicated by red boxes in Figure 3 for the (**a**) single pulse weld and the double pulse welds with a cooling time of (**b**) 50 ms and (**c**) 200 ms. The bold black lines represent the PAGs.

3.6. Energy-Dispersive X-Ray Spectroscopy

In order to visualize the distribution of manganese, EDX scans were conducted and manganese segregations, which are only a few micrometers wide, were detected. In the center of the FZ of the single pulse weld, the manganese segregations are oriented in vertical direction towards the electrodes and reach a manganese content of 9 to 11 wt%, as can be derived from the EDX mapping depicted in Figure 7. The areas between the segregations are consequently slightly depleted in manganese compared to the nominal content of 6.4 wt% and have an average content of 5 to 6 wt%.

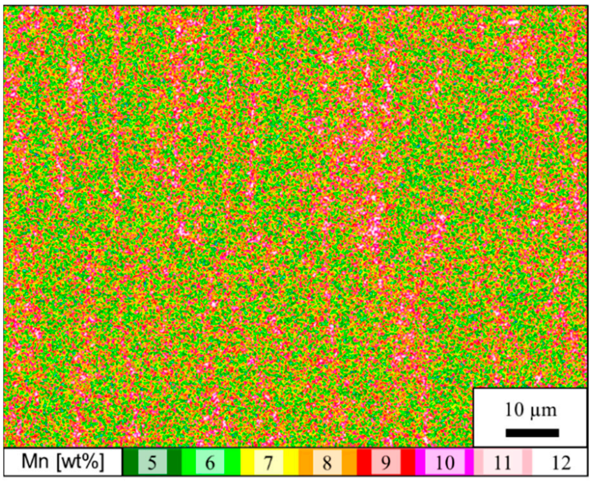

Figure 7. EDX mapping of the manganese distribution of the center of the FZ of the single pulse weld.

Because the edge of the FZ undergoes the in-process heat treatment due to the second pulse, the manganese distribution of this zone was also measured for the single pulse weld and the representative double pulse welds with cooling times of 50 and 200 ms and the results are depicted in Figure 8. At the edge of the FZ of the single pulse weld, the morphology of the segregations changes to a mainly horizontal, honeycomb-like arrangement, as shown in Figure 8a. The segregations are very fine and reach a maximum manganese content of about 9 wt% on average. The manganese distribution at the edge of the FZ of the double pulse weld with a cooling time of 50 ms is much more homogeneous, as indicated by Figure 8b. Even the few segregations in the lower third of the imaged area are not very pronounced and have a maximum manganese content of 7 to 8 wt%. Consequently, the manganese content of the remaining areas is higher and close to the nominal content. Double pulsing with a cooling time of 200 ms leads to an edge of the FZ with pronounced segregations of manganese, as illustrated by Figure 8c. They are mainly horizontally aligned and reach an average maximum manganese content of about 9 wt% with depleted areas in between.

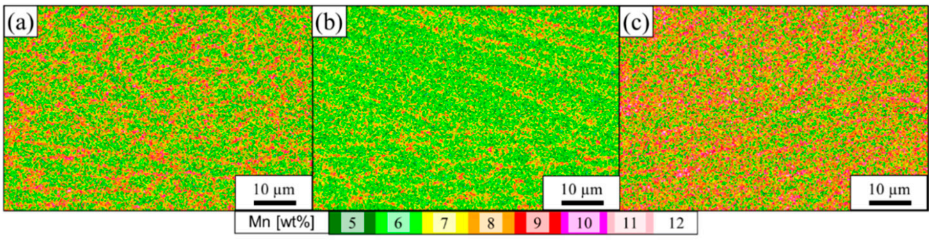

Figure 8. EDX mappings of the manganese distribution at the edge FZ of the (**a**) single pulse weld and the double pulse welds with a cooling time of (**b**) 50 ms and (**c**) 200 ms.

4. Discussions

The aim of the present work was to investigate the improvement of the mechanical performance and the characteristics of the microstructure due to double pulsing with different cooling times. The mechanical performance in terms of F_{max} (3.0 kN) and the pullout ratio (26%) of the single pulse welded medium-Mn steel, as shown in Figure 2, is unsatisfactory. Therefore, the results of the CTS tests in Figure 2 indicate that relatively short cooling times of 20, 50 or 100 ms lead an increased F_{max}. With 6.0, 6.3, and 5.8 kN, the maximum force is roughly doubled compared to the single pulse weld. With longer cooling times of 200 and 500 ms, F_{max} decreases again to 4.1 and 4.3 kN, respectively. Improved properties due to a very short cooling time are in agreement with the literature, where enhanced mechanical properties of AHSS spot welds were reported due to double pulsing with a cooling time of 40 ms [16,18,19]. Surprisingly, the pullout ratio appears not to correlate with the cooling time, scatters strongly, and is not significantly improved due to double pulsing.

The width of the secondary FZ is reported to depend on the heat input during the second pulse, which is mainly influenced by the applied current [18,19]. In the present work, it is shown that the heat input of the second pulse also strongly depends on the cooling time in between the pulses, even at the same current levels, due to the temperature dependence of the electrical resistance. As indicated by the images of the etched cross-sections in Figure 3, the width of the secondary FZ, and therefore, the heat input due to the second pulse, decrease successively with increasing cooling time. A secondary FZ is only visible for short cooling times of up to 100 ms, which results in the highest F_{max} and it disappears for longer cooling times. The presence of a secondary FZ is, therefore, a good indicator in terms of estimating the improvement of mechanical properties of the double pulse welds. The decrease of the heat input during the second pulse with increasing cooling times can also be derived from the resistance curves depicted in Figure 4. The resistance at the end of the single pulse in Figure 4a, which also represents the first pulse of each double pulse weld, is 115 µΩ. The resistance at the beginning of the second pulse depends on the temperature of the weld after the cooling time and affects the amount of heat generated during the second pulse, as can be derived from Equation (1). It successively decreases with increasing cooling time. With 100 and 90 μΩ, after short cooling times of 20 and 50 ms, the resistance, and therefore, the temperature at the beginning of the second pulse, are still high enough to cause partial re-melting of the primary FZ during the second pulse. After a longer cooling time of 200 ms, the resistance drops to 40 μΩ, which seems to be too low to generate sufficient heat during the second pulse to achieve the intended in-process heat treatment. The insufficient heat generation during the second pulse after a long cooling time is also evidenced by the hardness mappings. While the ICHAZ of the double pulse weld with a cooling time of 50 ms is narrow, the ICHAZ after a long cooling time, especially after 500 ms, is broad. This indicates that the intercritical temperature was reached at a closer distance to the FZ during the second pulse because less heat was generated.

While in dissimilar weldments the crack propagated through the CGHAZ of the medium-Mn steel [14,15], in the present work, the crack propagated through the edge of the FZ. Therefore, this zone was considered crucial and characterized in more detail. Generally, if the second pulse is correctly applied, it leads to the desired recrystallization of the edge of the primary FZ and to a more equiaxed PAG structure, which can be visualized using EBSD measurements [16,17,19,22]. Figure 6b shows that the edge of the primary FZ of the double pulse weld with a 50 ms cooling time consists of coarser and more equiaxed grains than the single pulse weld in Figure 6a. Especially the grains in the center of the image show signs of recrystallization due to the high temperature in this zone during the second pulse. The improved mechanical properties of these samples in Figure 2 are in good agreement with the literature, since more equiaxed PAGs are considered to promote crack deflecting, which results in enhanced toughness [16,17,22]. However, it has to be mentioned that the signs of recrystallization are not as pronounced as expected based on preliminary EBSD investigations on another AHSS grade [22]. This may be due to the lower carbon content in the medium-Mn steel, which is associated with a lower dislocation density of the martensite in the FZ and thus provides fewer nucleation sites for recrystallization. By extending the cooling time to 200 ms, the heat input during the second pulse decreases, as explained above, and the signs of recrystallization, therefore, completely disappear, as shown by Figure 6c. The reconstruction resembles the cast-like PAGs of the single pulse weld in Figure 6a, and the mechanical performance is inferior to the performance of the double pulse weld with the short cooling time. This is because recrystallization highly depends on temperature, which is not high enough to trigger it after a 200 ms cooling time.

It is reported that alloying elements like manganese tend to segregate to grain boundaries of third generation AHSS spot welds during solidification [18,30], which according to Eftekharimilani et al. [18], has a detrimental effect on the mechanical properties. The increased manganese content of the medium-Mn steels, compared to other third generation AHSS steel grades, results in high manganese segregations in the center of the FZ, as indicated in Figure 7. Their orientation changes according to the changed solidification direction from vertical in the center of the FZ in Figure 7 to a mainly horizontal, honeycomb-like alignment at the edge of the FZ, as shown in Figure 8a. Manganese segregations may act as local brittle points, according to Park et al. [13]. Consequently, they may contribute to the poor mechanical properties of the single pulse weld. The segregations at the edge of the FZ can be dissolved during the second pulse after a short cooling time of 50 ms, as can be seen in Figure 8b since the very high temperature enables manganese diffusion. Consequently, F_{max} improves significantly. In contrast, due to the lower heat input, the segregations at the edge of the primary FZ are still present for the double pulse weld with a cooling time of 200 ms, as shown in Figure 8c. At the same time, F_{max} decreases, which again illustrates the importance of a precisely chosen cooling time. These results coincide with those of Eftekharimilani et al. [18], who attributed the significantly improved mechanical properties of a third generation AHSS to the manganese homogenizations due to a properly chosen second pulse. However, in their work, the heat input, and therefore, the temperature during the second pulse were not controlled by the varying cooling time, but by the variation of the current of the second pulse. The manganese content of the investigated medium-Mn steel is more than twice as high as that of the steel grade discussed in the mentioned literature, and therefore, it is assumed that the manganese segregations play an even greater role in terms of the mechanical properties of medium-Mn steels.

The recrystallization of the edge of the FZ and especially the homogenization of manganese segregations during the second pulse are consequently considered as the main reasons for the enhanced properties of the double pulse welded medium-Mn steel welds with a short cooling time. Although both phenomena have the same origin, namely the high temperature, they should be considered separately in terms of their contribution to the improvement of the mechanical properties. Recrystallization does not lead to manganese homogenization per se or vice versa, but the high temperature does. Therefore, it is crucial to keep the cooling time short. However, it is surprising that the failure mode is not significantly improved by double pulsing and does not depend on the cooling time. Investigations regarding the relationship between the microstructure at the crack path and the mechanical performance are, therefore, decisive and the subject of further investigations.

5. Conclusions

In the present work, the influence of the cooling time on the mechanical performance, hardness distribution, and microstructural features of a double pulse resistance spot welded medium-Mn steel were investigated. After a short cooling time, the second pulse re-melts the center and heat treats the edge of the primary FZ. This desired in-process heat treatment leads to a modification of the cast-like martensitic structure and to a homogenization of manganese segregations, which results in enhanced mechanical performance of the welds. In contrast, during excessively long cooling times, the resistance drops to a level where the heat generation due to the second pulse is too low to sufficiently re-heat the edge of the primary FZ. No obvious recrystallization appears, the manganese segregations are still present, and thus the mechanical performance is not improved.

Author Contributions: Conceptualization, M.S., R.S. and C.H.; methodology, M.S.; software, M.G.; validation, R.S., K.S. and C.H.; investigation, M.S.; resources, M.G. and R.S.; data curation, M.S.; writing—original draft preparation, M.S.; writing—review and editing, R.S. and C.H.; visualization, M.S.; supervision, R.S. and C.H.; project administration, M.S.; funding acquisition, R.S. All authors have read and agreed to the published version of the manuscript.

Funding: This research was funded by Austrian BMK (846933) in the framework of the program “Production of the future” and the “BMK Professorship for Industry”.

Data Availability Statement: Not applicable.

Conflicts of Interest: The authors declare no conflict of interest.

References

1. Matlock, D.K.; Speer, J.G. Third generation of AHSS: Microstructure design concepts. In *Microstructure and Texture in Steels*; Haldar, A., Suwas, S., Bhattacharjee, D., Eds.; Springer: London, UK, 2009; pp. 185–205. ISBN 978-1-84882-454-6.
2. Fonstein, N. *Advanced High Strength Sheet Steels. Physical Metallurgy, Design, Processing and Properties*; Springer International Publishing: New York, NY, USA, 2015; ISBN 978-3-319-19164-5.
3. Aydin, H.; Essadiqi, E.; Jung, I.-H.; Yue, S. Development of 3rd generation AHSS with medium Mn content alloying compositions. *Mater. Sci. Eng. A* **2013**, *564*, 501–508. [CrossRef]
4. Lee, Y.-K.; Han, J. Current opinion in medium manganese steel. *Mater. Sci. Technol.* **2015**, *31*, 843–856. [CrossRef]
5. Miller, R.L. Ultrafine-grained microstructures and mechanical properties of alloy steels. *Metall. Mater. Trans. B* **1972**, *3*, 905–912. [CrossRef]
6. Lee, S.; de Cooman, B.C. On the selection of the optimal intercritical annealing temperature for medium Mn TRIP steel. *Metall. Mater. Trans. A* **2013**, *44*, 5018–5024. [CrossRef]
7. Steineder, K.; Krizan, D.; Schneider, R.; Béal, C.; Sommitsch, C. On the microstructural characteristics influencing the yielding behavior of ultra-fine grained medium-Mn steels. *Acta Mater.* **2017**, *139*, 39–50. [CrossRef]
8. Hu, J.; Du, L.-X.; Xu, W.; Zhai, J.-H.; Dong, Y.; Liu, Y.-J.; Misra, R.D.K. Ensuring combination of strength, ductility and toughness in medium-manganese steel through optimization of nano-scale metastable austenite. *Mater. Charact.* **2018**, *136*, 20–28. [CrossRef]

9. Cai, Z.H.; Ding, H.; Misra, R.D.K.; Ying, Z.Y. Austenite stability and deformation behavior in a cold-rolled transformation-induced plasticity steel with medium manganese content. *Acta Mater.* **2015**, *84*, 229–236. [CrossRef]
10. Merwin, M.J. Low-carbon manganese TRIP steels. *Mater. Sci. Forum* **2007**, *539–543*, 4327–4332. [CrossRef]
11. Pouranvari, M.; Marashi, S.P.H. Critical review of automotive steels spot welding: Process, structure and properties. *Sci. Technol. Weld. Join.* **2013**, *18*, 361–403. [CrossRef]
12. Jia, Q.; Liu, L.; Guo, W.; Peng, Y.; Zou, G.; Tian, Z.; Zhou, Y. Microstructure and tensile-shear properties of resistance spot-welded medium Mn steel. *Metals* **2018**, *8*, 48. [CrossRef]
13. Park, G.; Kim, K.; Uhm, S.; Lee, C. A comparison of cross-tension properties and fracture behavior between similar and dissimilar resistance spot-weldments in medium-Mn TRIP steel. *Mater. Sci. Eng. A* **2019**, *752*, 206–216. [CrossRef]
14. Park, G.; Kim, K.; Uhm, S.; Lee, C. Remarkable improvement in resistance spot weldability of medium-Mn TRIP steel by paint-baking heat treatment. *Mater. Sci. Eng. A* **2019**, *766*, 138401. [CrossRef]
15. Park, G.; Uhm, S.; Lee, C. Effects of in-situ post-weld heat treatment on the microstructure and mechanical properties of the coarse-grained heat-affected zone in a resistance spot weld in medium Mn TRIP steel. *Mater. Sci. Eng. A* **2020**, *788*, 139477. [CrossRef]
16. Chabok, A.; van der Aa, E.; de Hosson, J.T.M.; Pei, Y.T. Mechanical behavior and failure mechanism of resistance spot welded DP1000 dual phase steel. *Mater. Des.* **2017**, *124*, 171–182. [CrossRef]
17. Eftekharimilani, P.; van der Aa, E.M.; Hermans, M.J.M.; Richardson, I.M. Microstructural characterisation of double pulse resistance spot welded advanced high strength steel. *Sci. Technol. Weld. Join.* **2017**, *22*, 545–554. [CrossRef]
18. Eftekharimilani, P.; van der Aa, E.M.; Hermans, M.J.M.; Richardson, I.M. The microstructural evolution and elemental distribution of a 3rd generation 1 GPa advanced high strength steel during double pulse resistance spot welding. *Weld. World* **2017**, *61*, 691–701. [CrossRef]
19. Liu, X.D.; Xu, Y.B.; Misra, R.D.K.; Peng, F.; Wang, Y.; Du, Y.B. Mechanical properties in double pulse resistance spot welding of Q&P 980 steel. *J. Mater. Process. Technol.* **2019**, *263*, 186–197. [CrossRef]
20. Hernandez, V.B.; Okita, Y.; Zhou, Y. Second pulse current in resistance spot welded TRIP steel: Effects on the microstructure and mechanical behavior. *Impulse* **2012**, *91*, 278–285.
21. Sajjadi-Nikoo, S.; Pouranvari, M.; Abedi, A.; Ghaderi, A.A. In situ postweld heat treatment of transformation induced plasticity steel resistance spot welds. *Sci. Technol. Weld. Join.* **2018**, *23*, 71–78. [CrossRef]
22. Stadler, M.; Gruber, M.; Schnitzer, R.; Hofer, C. Improving the mechanical performance of a resistance spot welded 1200 MPa TBF steel. *Int. J. Mater. Res.* **2021**. accepted for publication.
23. Stadler, M.; Gruber, M.; Schnitzer, R.; Hofer, C. Microstructural characterization of a double pulse resistance spot welded 1200 MPa TBF steel. *Weld. World* **2020**, *64*, 335–343. [CrossRef]
24. STAHL-EISEN-Prüfblätter (SEP) des Stahlinstituts VDEh. *SEP 1220-2. Testing and Documentation Guideline for the Joinability of Thin Sheet of Steel-Part. 2: Resistance Spot Welding*; Verlag Stahleisen GmbH: Düsseldorf, Germany, 2011.
25. Cayron, C. ARPGE: A computer program to automatically reconstruct the parent grains from electron backscatter diffraction data. *J. Appl. Crystallogr.* **2007**, *40*, 1183–1188. [CrossRef] [PubMed]
26. Han, X.; DiGiovanni, C.; McDermid, J.; Biro, E.; Zhou, N.Y. Effect of internal oxidation on the weldability of CMnSi steels. *Weld. World* **2019**, *63*, 1633–1639. [CrossRef]
27. Ghatei Kalashami, A.; Han, X.; Goodwin, F.; Zhou, N.Y. The influence of modified annealing during the galvanizing process on the resistance spot welding of the CMn1.8Si advanced high strength steel. *Surf. Coat. Technol.* **2020**, *381*, 125181. [CrossRef]
28. Zhou, K.; Cai, L. Online nugget diameter control system for resistance spot welding. *Int. J. Adv. Manuf. Technol.* **2013**, *68*, 2571–2588. [CrossRef]
29. Dickinson, D.W.; Franklin, J.E.; Stanya, A. Characterization of spot welding behavior by dynamic electrical parameter monitoring. *Weld. J.* **1980**, *59*, 170–176.
30. Van der Aa, E.M.; Amirthalingam, M.; Winter, J.; Hanlon, D.N.; Hermans, M.J.M.; Rijnders, M.; Richardson, I.M. Improved resistance spot weldability of 3rd generation AHSS for automotive applications. In Proceedings of the 11th International Seminar on Numerical Analysis of Weldabiltity, Graz, Austria, 27–32 September 2015.

Paper IV

M. Stadler, R. Schnitzer, M. Gruber, K. Steineder, C. Hofer

Microstructure and local mechanical properties of the heat-affected zone of a resistance spot welded medium-Mn steel

Materials 14 (2021) 3362

materials

Article

Microstructure and Local Mechanical Properties of the Heat-Affected Zone of a Resistance Spot Welded Medium-Mn Steel

Manfred Stadler [1],*, Ronald Schnitzer [1], Martin Gruber [2], Katharina Steineder [2] and Christina Hofer [1]

[1] Department of Materials Science, Montanuniversität Leoben, Franz-Josef-Strasse 18, 8700 Leoben, Austria; ronald.schnitzer@unileoben.ac.at (R.S.); christina.hofer@unileoben.ac.at (C.H.)

[2] Voestalpine Stahl GmbH, Voestalpine-Strasse 3, 4020 Linz, Austria; martin.gruber@voestalpine.com (M.G.); katharina.steineder@voestalpine.com (K.S.)

* Correspondence: manfred.stadler@unileoben.ac.at; Tel.: +43-3842-402-4268

Abstract: The properties of the heat-affected zone (HAZ) are reported to have a great influence on the mechanical performance of resistance spot welded advanced high strength steels. Therefore, in the present work, the HAZ of a medium-Mn steel is characterized regarding its microstructure and its mechanical properties depending on the distance to the fusion zone (FZ). In order to obtain the local mechanical properties of the HAZ, samples were heat-treated in a joule-heating thermal simulator using different peak temperatures to physically simulate the microstructure of the HAZ. By comparing the microstructure and the hardness of these heat-treated samples and the HAZ, the local peak temperatures within the HAZ could be determined. Subsequently, tensile tests were conducted, and the austenite phase fraction was measured magnetically on the physically simulated HAZ samples in order to determine the local mechanical properties of the HAZ. As verified by energy-dispersive X-ray spectroscopy, peak temperatures above 1200 °C led to a uniform distribution of manganese, resulting in a predominantly martensitic microstructure with high strength and low total elongation after quenching. Below 1100 °C, the diffusion of manganese is restricted, and considerable fractions of austenite remain stable. The austenite fraction increases almost linearly with decreasing peak temperature, which leads to an increase of the total elongation and to a slight decrease in the strength, depending on the distance to the FZ. Temperatures below 700 °C exhibit hardly any effect on the initial microstructure and mechanical properties.

Keywords: third-generation advanced high strength steels (AHSS); medium-Mn steel; resistance spot welding (RSW); heat-affected zone (HAZ); local mechanical properties

check for updates

Citation: Stadler, M.; Schnitzer, R.; Gruber, M.; Steineder, K.; Hofer, C. Microstructure and Local Mechanical Properties of the Heat-Affected Zone of a Resistance Spot Welded Medium-Mn Steel. *Materials* **2021**, *14*, 3362. https://doi.org/10.3390/ma14123362

Academic Editor: Shinichi Tashiro

Received: 11 May 2021
Accepted: 15 June 2021
Published: 17 June 2021

1. Introduction

The demands of the automotive industry regarding lightweight construction and simultaneous increase of passenger safety require the application of advanced high-strength steels (AHSS). The research currently focuses on the third generation of these high-performance steels, which are characterized by high strength and acceptable ductility at a significantly lower cost compared to the second generation. This generation consists of quenching and partitioning (Q&P) [1], transformation-induced plasticity (TRIP)-aided bainitic ferrite (TBF) steels [2] and medium-Mn steels [3,4]. First introduced in 1972 by Miller [5], the medium-Mn concept was revived in 2007 by Merwin [6], and since then, research on these steels has intensified again. Their microstructure is composed of a ferritic matrix and a high fraction of austenite of about 30%, which, in contrast to Q&P and TBF steels, is not primarily stabilized by carbon enrichment, but mainly by manganese redistribution during an intercritical heat treatment [5,7]. To achieve this, a manganese content of 4–10% is alloyed. The annealing conditions such as temperature, time and heating and cooling rate play an important role in terms of the austenite quantity and stability [8]. In particular, the annealing temperature has to be chosen carefully to obtain metastable austenite that does not transform into martensite during the final cooling step. The stability of the austenite, which depends among other things on its chemical composition, its grain size and the surrounding matrix, is ultimately responsible for the TRIP effect [9]. Depending on the microstructure prior to the intercritical annealing, the shape of the austenite grains can either be globular or lath-like [10]. In this context, a lath-like austenite is reported to be more stable and offers enhanced mechanical properties [10].

Due to the desired establishment of medium-Mn steels for automotive applications, their workability has to be taken into account. In this context, the resistance spot weldability is of particular importance, as this process is the predominant joining technology in the automotive industry [11]. However, the increased alloying content in third-generation AHSS generally results in a pronounced hardening of the fusion zone (FZ), which reduces their weldability compared to mild steels [12]. Consequently, the modification of the microstructure of the FZ, for example, with a second pulse that acts as an in-process heat treatment, represents a well-documented approach to improve their mechanical performance [13–18]. This approach has already been successfully adopted to improve the properties of the medium-Mn steel investigated in the present work [19].

In addition to the FZ, the microstructure of the heat-affected zone (HAZ) also influences the mechanical performance of spot-welded AHSS sheets [12,13,20–22]. Generally, the HAZ of AHSS can be subdivided into the upper critical heat-affected zone (UCHAZ), where the temperature during welding exceeds the A_3 temperature; the intercritical heat-affected zone (ICHAZ), where the peak temperature is between A_3 and A_1; and the subcritical heat-affected zone (SCHAZ), where the peak temperature is below A_1 [23]. The UCHAZ of AHSS usually consists of a fully martensitic microstructure, whose grain size decreases with increasing distance to the FZ because of the decreasing peak temperature [12,13,23–25]. Therefore, the UCHAZ can be subdivided into a coarse-grained heat-affected zone (CGHAZ) and a fine-grained heat-affected zone (FGHAZ) [18,25]. Additionally, all of the bainite or martensite-containing AHSS exhibit a significantly softened SCHAZ as a result of tempering effects, which is reported to potentially act as a local necking point and therefore influences the mechanical properties of the welds in a negative way [13,23,26,27]. In these regards, the medium-Mn steels differ significantly from other AHSS. First of all, their SCHAZ cannot soften due to the absence of martensite in the base material (BM). Secondly, due to the stabilization by manganese, some retained austenite may still be present in parts of the UCHAZ [28–30]. This is the consequence of the slower diffusion of the substitutionally dissolved alloying element manganese compared to the interstitially dissolved carbon at elevated temperatures [31]. The higher temperature in the CGHAZ leads to a more uniform distribution of manganese, and therefore the fraction of austenite is significantly reduced compared to the FGHAZ [29,30].

The tensile properties of these zones are of great importance regarding the mechanical performance of the welds and have already been investigated in the literature for a number of AHSS [24,26,29,31]. As the CGHAZ offers high strength at low total elongation, it is usually very brittle, which may promote crack propagation through this zone [24,26]. Because of grain refinement, both strength and total elongation increase in the FGHAZ [24]. In contrast, the strength in the ICHAZ and SCHAZ is lower compared to the BM at a high total elongation [24]. Embrittlement of the fully martensitic CGHAZ and associated deterioration of the mechanical performance of the welds is also reported for a medium-Mn steel [29]. In the FGHAZ, both the strength and ductility increase due to fine martensite and the presence of austenite. Therefore, a targeted adjustment of this microstructure at the area where failure occurs is very promising. An approach to achieve remarkable improvement of the ductility of the CGHAZ by in situ post-weld heat treatment was already presented by Park et al. [31] and can be seen as a first step towards targeted HAZ design.

However, since the diffusivity of manganese is very sensitive to temperature, it can be assumed that the manganese distribution and thus the austenite stability varies strongly over the entire HAZ of medium-Mn steels, which may lead to position-dependent mechanical properties. Therefore, the present work aims to investigate the thermal stability of the austenite in the HAZ as a function of the distance to the FZ and determine its influence on the local mechanical properties. While all the available studies [24,26,29,31] rely on a finite element (FE) software, namely SORPAS (Lyngby, Denmark) by SWANTEC, to simulate the thermal cycle during resistance spot welding (RSW), a different approach is presented in this work, which allows the precise replication of the temperature profile and the investigation of the entire HAZ in a small step size based on the actual microstructure. To achieve this, samples were heat-treated on a thermal simulator in order to reproduce the microstructure of the HAZ. For this purpose, sheets were rapidly heated to various peak temperatures quickly quenched to physically simulate the thermal profile in the HAZ during the RSW process. By comparing the microstructure and the hardness of the physically simulated HAZ samples and the HAZ, the local peak temperatures within the HAZ during an RSW cycle could be determined. On the physically simulated HAZ samples, the mechanical properties and the retained austenite were ascertained. Knowledge of the local properties allows targeted HAZ engineering to improve the mechanical properties of the weld in the future.

2. Materials and Methods

The investigated medium-Mn steel has a nominal composition of 0.1 C/6.4 Mn/0.6 Si (wt%). The resistance spot welded steel sheets were uncoated and had a thickness of 1.18 mm. RSW was conducted on a MFDC-1000 Hz pedestal-type welding machine from Nimak (Wissen, Germany), which is equipped with an AutoSpatz regulator (Matuschek, Alsdorf, Germany) to deliver constant current. As recommended in VDEh SEP1220-2 [32], F1-16-20-6 electrodes that operated at a clamping force of 4.0 kN were used. The samples were welded for 280 ms at a current of 4.8 kA, representing the current, which is just high enough to produce a weld nugget with a diameter of $4 \times \sqrt{t}$, where t is the sheet thickness.

The different parts of the HAZ were physically simulated by heat-treating sheets of $150 \times 20 \times 1.2$ mm^3 on a self-constructed joule-heating thermal simulator. The sheets were heated to different peak temperatures ranging from 1300 to 500 °C in steps of 50 °C, at a rate of about 1300 K/s and then quenched as quickly as possible by means of a water spray. The cooling rate was safely above the critical cooling rate to form martensite. A thermocouple Type K (Ni-CrNi) is welded onto edges in the middle of the sample to facilitate the temperature control. The AC power transformer allows a regulation interval of 20 ms, while the temperature is measured each millisecond. The overall temperature field is homogeneously distributed along the full thickness and width of the sample along 50 mm of length.

The mechanical properties of the flat tensile samples ($n = 1$) with the geometry illustrated in Figure 1 were evaluated by tensile testing according to DIN EN ISO 6892-1 [33] on a BETA 400/150-150 testing machine from Messphysik (Fürstenfeld, Austria). The samples were tested longitudinally to the rolling direction. The austenite phase fraction was determined via magnetic saturation measurement (voestalpine-Mechatronics). Hardness testing on the HAZ and the physically simulated HAZ samples was performed at a load of 300 g and a dwell time of 10 s on a Qness hardness tester Q60A+ (Golling, Austria). The hardness of the HAZ was determined from the average of three tests, along vertical lines at an angle of 10° to the sheet/sheet interface according to the isotherms. The vertical distance between the indents within one line was 200 µm. In order to meet the required minimum distances between the indent at a still high small step size of 75 µm, an alternating offset of 100 µm was selected between the respective lines. The hardness of the physically simulated HAZ samples represents an average of five tests.

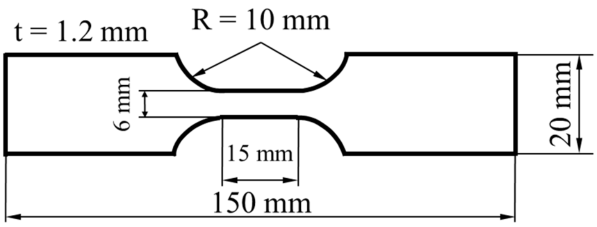

Figure 1. Dimensions of the flat tensile samples.

For the microstructural characterization, cross-sections were ground, polished and etched with a 3% Nital solution. An M1M Imager equipped with an AxioCam MRc5 camera, both from Zeiss (Oberkochen, Germany), was used for light optical microscopy (LOM). The microstructure of the HAZ was determined at eight positions with a distance of 150 µm. Secondary electron (SE) scanning electron microscopy (SEM) images were obtained on a VERSA 3D from FEI (Hillsboro, OR, USA). Electron backscattered diffraction (EBSD) measurements were performed with a step size of 25 nm at a working distance of 15 mm and at an acceleration voltage of 20 kV on the aforementioned SEM, which is equipped with an EDAX Hikari XP (Mahwah, NJ, USA) EBSD system. Since EBSD requires a deformation-free surface, the polished cross-sections were additionally ion milled for 15 min with an ArBlade5000 ion milling system from Hitachi (Chiyoda, Tokio, Japan). Data evaluation was done with the software package OIM Analysis 7 from EDAX (Mahwah, NJ, USA) without any clean-ups. The backscattered electron (BSE) SEM and the energy-dispersive X-ray diffraction (EDX) measurements were conducted on a TESCAN CLARA (Brünn, Czech Republik). EDX measurements were performed at an acceleration voltage of 15 kV, using an X-Max system and the Aztec software from Oxford Instruments (Abington, UK).

3. Results and Discussion

3.1. Microstructure of the Base Material

The microstructure of the BM consists of a ferritic (body-centered cubic, bcc) matrix with a considerable fraction of finely dispersed austenite (face-centered cubic, fcc), which is predominantly present in a lath-like arrangement, as shown in the EBSD phase map in Figure 2a, and has a hardness of 288 HV. The data points with a confidence index (CI) below 0.1 were disregarded and are shown in black. They represent either grain boundaries or austenite, which is too fine to be reliably indexed. The numbered circles mark the nine locations where EDX measurements were conducted to determine the manganese content. Due to the similar atomic number of iron and manganese, there is no pronounced chemical contrast using BSE, but the austenite appears slightly brighter due to the higher packing density [34], as can be seen in Figure 2b. Larger, globular austenitic regions contain a manganese content of 11.5 to 12.5 wt% (spots 1–3). However, since the grain size of the austenite is very small, the EDX spot always excites a certain amount of ferrite as well, which generally leads to an underestimation of the manganese content of the austenite. For this reason, more manganese is measured in large austenite islands (spot 4), while less is detected in thin laths (spot 5). The ferritic matrix (spots 6–9) is slightly depleted in manganese compared to the nominal composition of 6.4 wt%. Ferrite that is far from manganese-rich austenite, such as spots 6 and 7, has a higher manganese content than that located adjacent to austenite, such as spots 8 and 9. However, as stated above, the EDX spot excites a relatively large volume that likely contains some austenite, which leads to an overestimation of the manganese content of the ferrite. Due to the higher content of less noble manganese, the austenitic areas were more severely attacked by the Nital etchant compared to the ferritic matrix, as illustrated in the corresponding SE image in Figure 2c. The circular shading at positions 1–9 is caused by carbon contamination during the EDX measurements. At these points, the surface was protected from the etchant; hence, there is no etching attack.

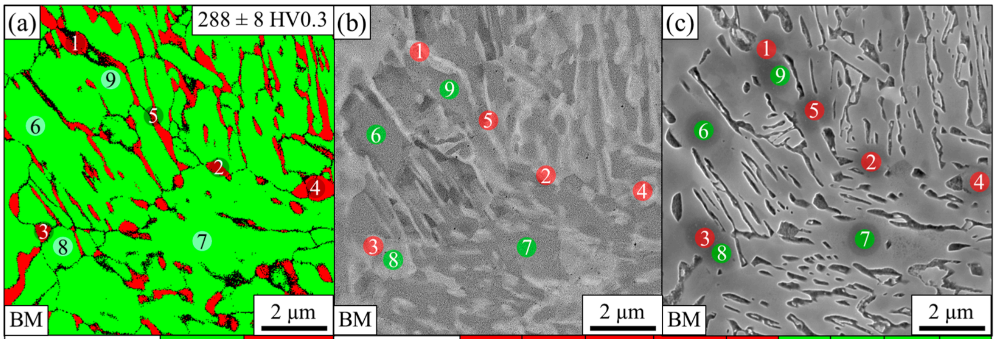

phase	bcc	fcc	EDX spot	1	2	3	4	5	6	7	8	9
total fraction	0.800	0.116	Mn (wt%)	11.5	11.8	12.5	13.4	9.7	6.1	6.5	5.5	5.1

Figure 2. (**a**) EBSD phase map of the base material, (**b**) corresponding BSE image and (**c**) corresponding SE image after Nital etching. The numbered circles (1–9) indicate the points where the manganese content was determined with EDX.

3.2. Characterization of the Heat-Affected Zone

The microstructure of the HAZ was determined at eight positions with a distance of 150 µm, as shown in the LOM image in Figure 3. Nital etching reveals a change in the microstructure between positions 3 and 4 as well as near position 7.

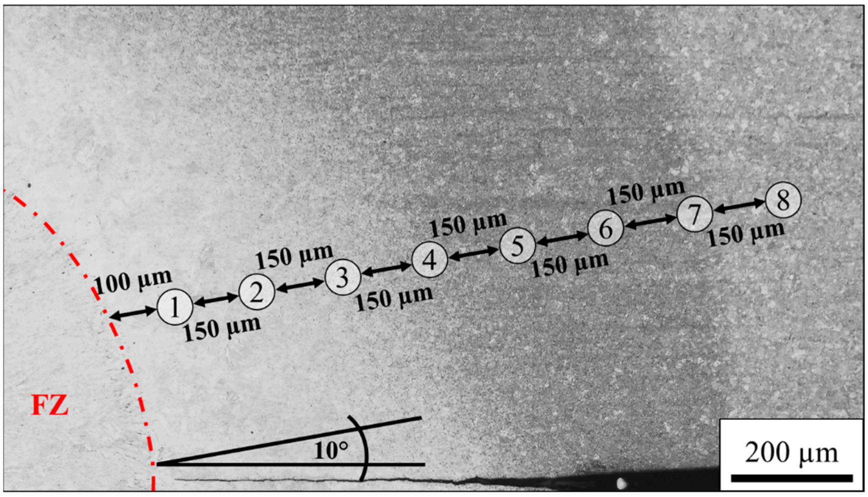

Figure 3. LOM image of the etched HAZ with the different positions numbered from 1–8.

As can be seen in the phase map in Figure 4a, no austenite was detected by EBSD at position 1, and the high hardness of 427 HV suggests that the bcc phase represents martensite instead of ferrite. The non-indexed black areas represent martensite block boundaries. The microstructure at position 2 is predominately martensitic with some small individual austenitic regions according to the EBSD phase map illustrated in Figure 4b. The hardness increases to 446 HV. As can be seen in Figure 4c, distinctive austenite grains are detected at position 3. The indexed austenite fraction is still low at 1.2%. However, thin films are below the resolution limit, and therefore it is reasonable to assume that the austenite fraction is underestimated as austenite most likely represents a significant amount of the unindexed points. The hardness further slightly increases to 455 HV. The continuous increase in hardness in this predominantly martensitic region can be explained by grain refinement of the martensite due to the lower austenitization temperature with increasing distance to the FZ. At position 4 (Figure 4d), a considerable amount of austenite of 5.3% with a CI > 0.1 is present. Some of it exhibits a lath-like morphology. The increased austenite fraction leads to a more selective etching attack, which explains the different appearance of this zone between positions 4–6 in the LOM image in Figure 3. The EBSD phase map at position 5 in Figure 4e reveals an austenite phase fraction of 11.2%, which remains almost constant at position 6 (10.8%), as indicated by Figure 4f. The hardness at positions 4–6 is 445, 447 and 437 HV, respectively. Near position 7, the microstructure changes again, as illustrated in Figure 3. This correlates to the ICHAZ, where the material is partly austenitized. Therefore, the microstructure consists of ferrite, martensite and austenite. At position 7, shown in Figure 4g, the austenite fraction increases to 13.2%, and the low hardness of 306 HV illustrates that the bcc phase predominantly represents ferrite instead of martensite. However, the slightly increased hardness compared to the BM indicates that some martensite may be present, which cannot be distinguished from ferrite by EBSD phase maps due to the same crystal structure. A distinction via the image quality as applied in other third-generation AHSS [35,36] is not possible because the low carbon content in the medium-Mn steel results in low distortion of the martensitic lattice. For positions beyond, the A_1 temperature is no longer exceeded. Therefore, the bcc phase consistently represents the soft ferrite. With a fraction of 15.3%, as illustrated in Figure 4h, the austenite fraction reaches a maximum at position 8 and the hardness of 293 HV hardly differs from that of the BM.

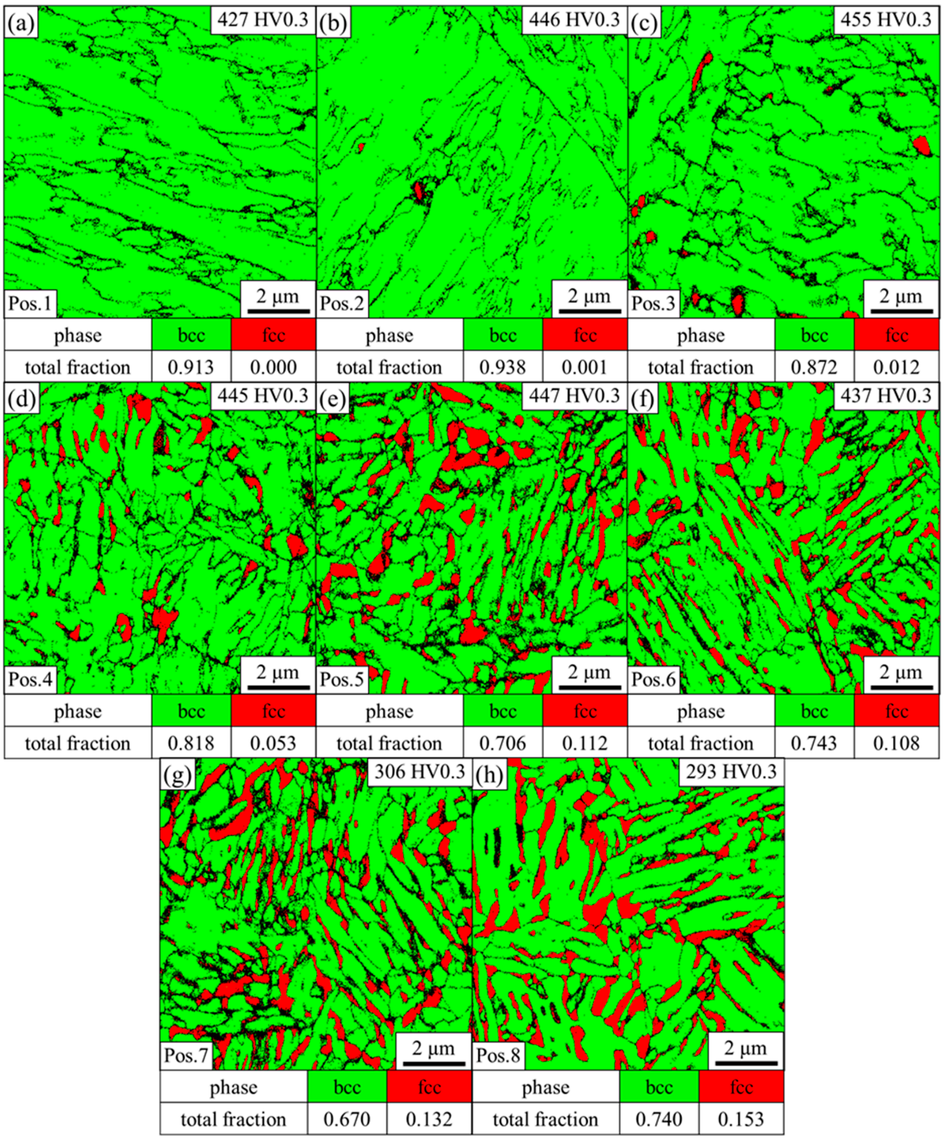

Figure 4. EBSD phase map of the HAZ taken at (**a**) position 1, (**b**) position 2, (**c**) position 3, (**d**) position 4, (**e**) position 5, (**f**) position 6, (**g**) position 7 and (**h**) position 8, as indicated in Figure 3.

The increasing fraction of austenite with increasing distance to the FZ is also reflected in BSE images and EDX measurements in Figure 5. As can be seen in Figure 5a,b, the BSE contrast at positions 1 and 2 is very low and mainly caused by the orientation contrast of the martensitic laths. Neither EDX measurements at bright areas (red points), nor at dark areas (green points), indicate pronounced manganese enrichment or depletion, which can be explained by the enabled diffusion of manganese at high temperatures. The BSE contrast at position 3 in Figure 5c is enhanced compared to positions 1 and 2. Analysis of two particularly bright areas (points 1 and 2) reveal a manganese content of 13.1 and 10.8 wt%, respectively. The high manganese content suggests that these areas most likely represent austenite. At position 4 (Figure 5d), manganese is not completely homogenized, and lath-like features resembling the morphology of austenite in the BM can be seen in BSE contrast. Particularly large bright areas have a manganese content of 12.8 and 13.1%, respectively, and therefore represent austenite, while the dark areas are depleted in manganese and correspond to martensite. Position 5 only shows low temperatures, and therefore the characteristic lath-like morphology of the austenite is almost completely retained, resulting in a high contrast in the BSE image in Figure 5e. The bright areas have a manganese content of 11.3 and 11.4%, respectively, while the dark areas are slightly depleted in manganese with 5.1 and 5.3%, respectively.

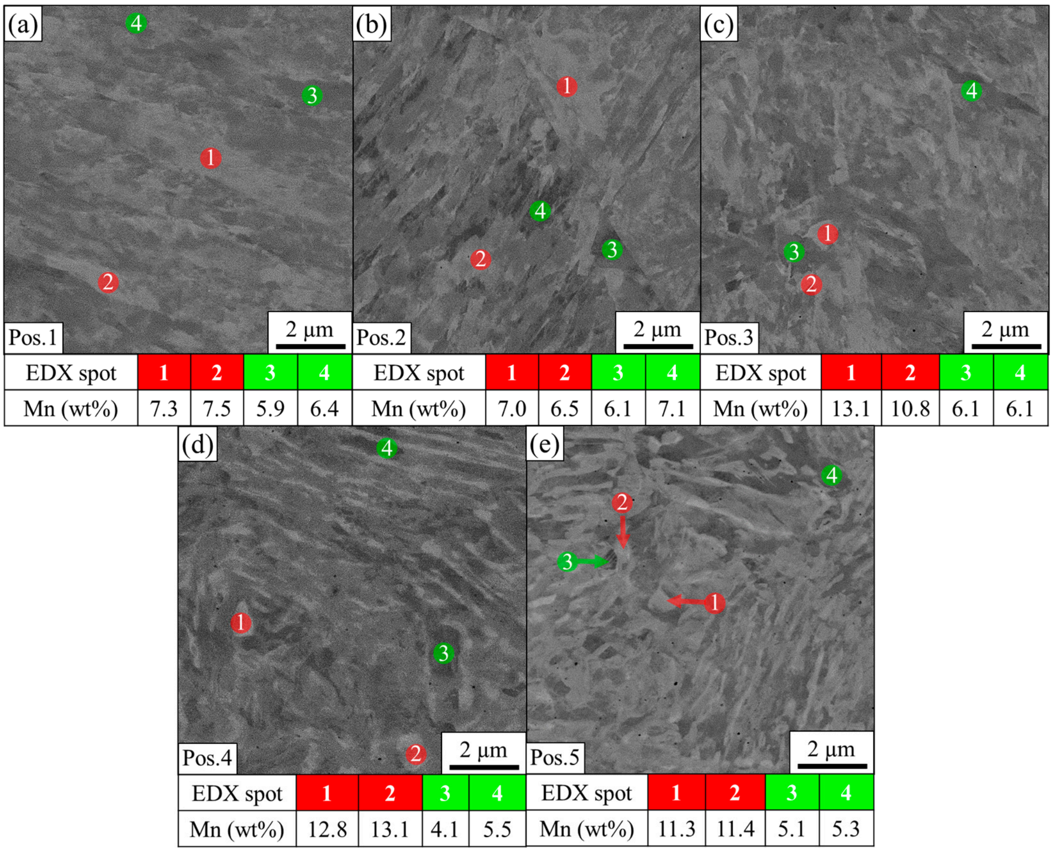

EDX spot	1	2	3	4
Mn (wt%)	7.3	7.5	5.9	6.4

EDX spot	1	2	3	4
Mn (wt%)	7.0	6.5	6.1	7.1

EDX spot	1	2	3	4
Mn (wt%)	13.1	10.8	6.1	6.1

EDX spot	1	2	3	4
Mn (wt%)	12.8	13.1	4.1	5.5

EDX spot	1	2	3	4
Mn (wt%)	11.3	11.4	5.1	5.3

Figure 5. BSE images of the HAZ taken at (**a**) position 1, (**b**) position 2, (**c**) position 3, (**d**) position 4, and (**e**) position 5, as shown in Figure 3. The numbered circles (1–4) indicate the points where the manganese content was determined with EDX for each position.

3.3. Characterization of the Samples of the Physically Simulated Heat-Affected Zone

To simulate the temperature profile in the HAZ during RSW, sheets were heated to different peak temperatures as quickly as possible and then rapidly quenched. In order to correlate the microstructure of the physically simulated HAZ samples to the HAZ, their microstructure was investigated by means of EBSD as well. As can be seen in Figure 6a,b, peak temperatures of 1300 °C and 1200 °C lead to a fully martensitic microstructure after quenching with a hardness of 415 and 434 HV, respectively. At a peak temperature of 1100 °C, a low fraction of 1.2% austenite with a CI > 0.1 is present, as shown in Figure 6c, and the hardness slightly increases to 446 HV. The austenite fraction increases to 3.4% at a peak temperature of 1000 °C with a hardness of 443 HV (Figure 6d). The EBSD phase map at 900 °C (Figure 6e) reveals an austenite fraction of 10.3%, which predominantly exhibits a lath-like morphology. With 444 HV, the hardness stays almost constant. At 15.2%, the austenite fraction detected by EBSD reaches a maximum at a peak temperature of 800 °C, as illustrated in Figure 6f. Since the hardness only moderately decreases to 426 HV, the bcc phase presumably predominantly represents martensite. As can be seen in Figure 6g, a peak temperature of 700 °C results in a low hardness of 282 HV with an austenite fraction of 13.8%.

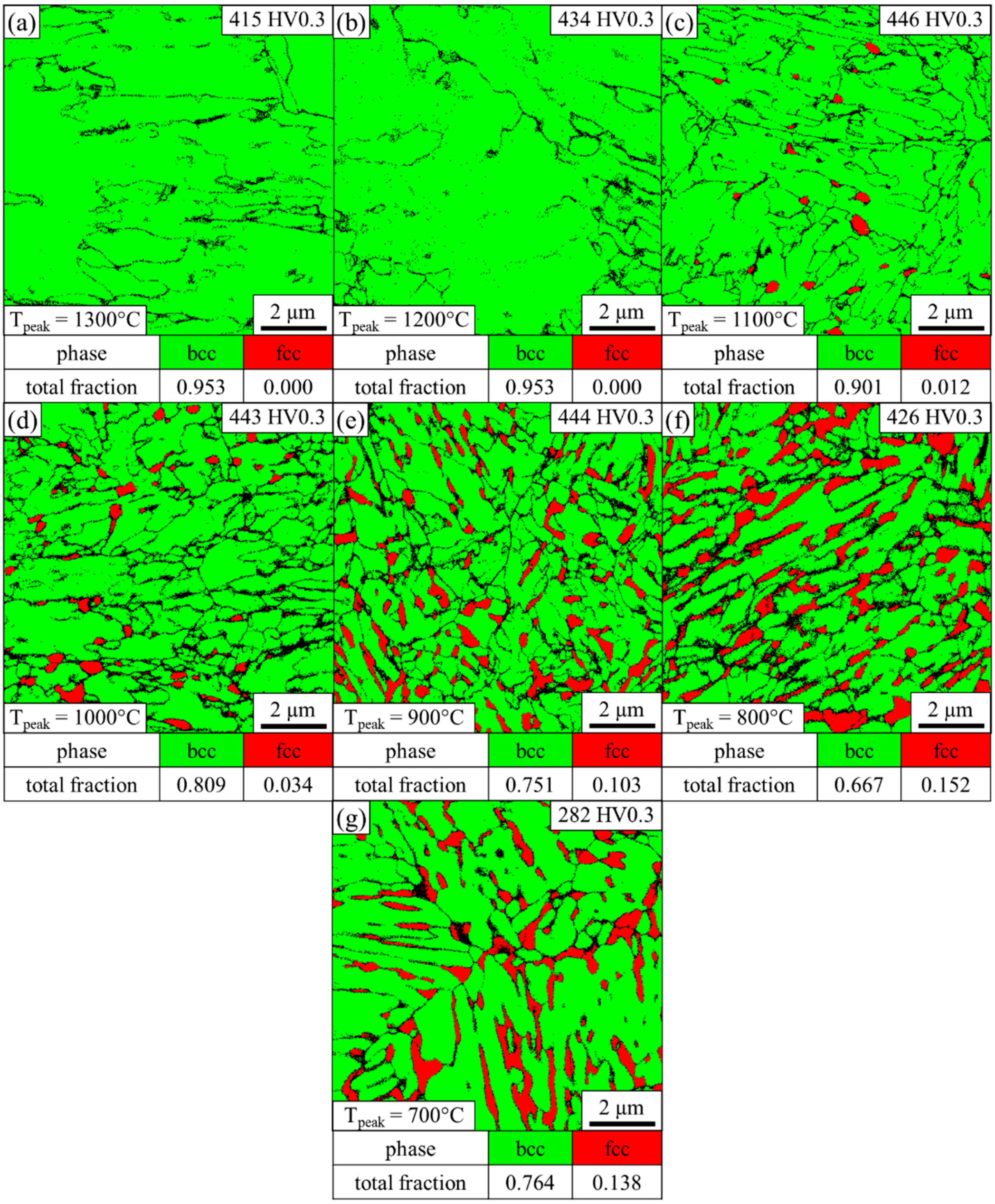

Figure 6. EBSD phase map of the physically simulated HAZ samples heated to a peak temperature of (**a**) 1300 °C, (**b**) 1200 °C, (**c**) 1100 °C, (**d**) 1000 °C, (**e**) 900 °C, (**f**) 800 °C and (**g**) 700 °C and subsequently quenched as quickly as possible.

3.4. Correlation of the Physically Simulated HAZ Samples to the Heat-Affected Zone

In order to determine the local peak temperatures that were present in the HAZ during welding, the microstructure and the hardness of the physically simulated HAZ samples were compared to the HAZ. The EBSD phase maps of the physically simulated HAZ samples show that the microstructure at the peak temperatures of 1300 °C and 1200 °C is fully martensitic. A minor fraction of 1.2% austenite is detected at a peak temperature of 1100 °C, which corresponds to position 3 in the HAZ. As illustrated in Figure 4c, position 3 represents the closest point to the FZ where individual austenitic grains and a comparable fraction of austenite were detected by EBSD. The ICHAZ represents another characteristic point of reference, since it is accompanied by a sharp drop in hardness due to the change of a martensitic to a ferritic matrix. From the optical micrograph in Figure 3 and the sudden decrease in hardness from 437 HV at position 6 (Figure 4f) to 306 HV at position 7 (Figure 4g), it can be inferred that the ICHAZ is close to position 7. In the physically simulated HAZ samples, the hardness abruptly drops from 426 HV at a peak temperature of 800 °C (Figure 6f) to 282 HV at a peak temperature of 700 °C (Figure 6g). Thus, it can be concluded that the ICHAZ has a temperature between 700 and 800 °C during the RSW cycle. The remaining points were fitted under the assumption of a roughly linear decrease of the peak temperature with increasing distance to the FZ, as can be derived from the results of Park et al. [30]. As shown by Figure 7, the resultant hardness profile of the HAZ (blue squares) and the physically simulated HAZ samples (red circles) show good agreement. Further, the austenite phase fraction and morphology in the EBSD phase maps of the HAZ in Figure 4 and the physically simulated HAZ samples in Figure 6 also correspond well. In summary, the temperature profile of the HAZ could be reproduced and therefore enable the determination of the austenite fraction and the local mechanical properties of the HAZ by means of the physically simulated HAZ samples.

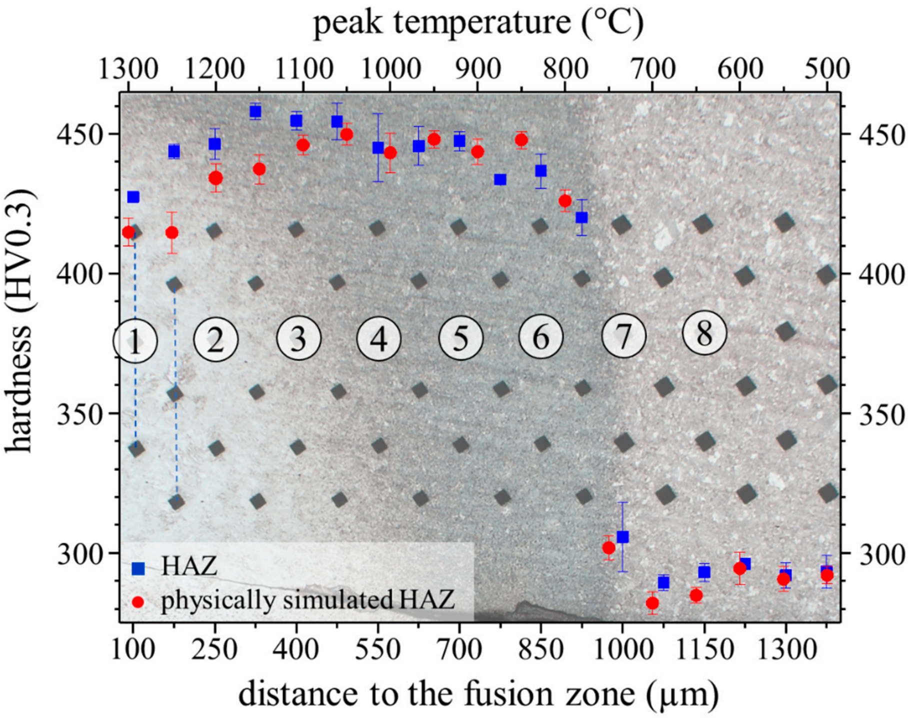

Figure 7. Correlation of the peak temperature of physically simulated HAZ samples to the HAZ, which is shown in the background, by means of the EBSD phase maps and the hardness profiles. The numbered circles (1–8) represent the different positions of the HAZ where the microstructural characterization was done, as already described by Figure 3. The blue squares represent the hardness of the HAZ as a function of the distance to the FZ (lower axis). The red circles represent the hardness of the physically simulated HAZ as a function of the peak temperature (upper axis).

3.5. Austenite Fraction and Local Mechanical Properties

Although EBSD phase maps allow a qualitative comparison of the austenite fraction, as demonstrated in the previous sections, the extremely fine microstructure results in a systematic underestimation of the austenite fraction by EBSD. Therefore, it was quantified on the physically simulated HAZ samples using magnetic saturation measurements. The magnetic determination of the austenite fraction of the BM revealed a fraction of 27.2%, which illustrates on the one hand the considerable underestimation by EBSD (11.6%) and on the other hand shows that the medium-Mn steel investigated in the present work has a significantly higher austenite fraction than medium-Mn steels in comparable studies [28,29]. The yield strength (YS) of the BM is 639 MPa, the tensile strength (TS) is 864 MPa and the total elongation (A_{15}) is 33.6%, as determined via tensile testing of a flat tensile sample. Since the peak temperatures of the physically simulated HAZ samples were correlated to the thermal profile of the HAZ, as described in the previous section, the austenite fraction and the local mechanical properties of the HAZ can be determined and are summarized in Figure 8. The results show that the austenite fraction is close to zero above a peak temperature of 1150 °C. With this predominantly martensitic phase, both YS and TS increase continuously with greater distance to the FZ. This is due to decreasing grain size at lower peak temperatures, and a maximum of 1102 MPa and 1371 MPa is reached near position 3. A_{15} remains at a more or less constant level between 11.6% and 13.1%. The austenite fraction increases almost linearly from 1.7% at position 3 to 26.9% at position 6. The increasing fraction of austenite leads to a moderate increase in A_{15} from 11.6% to 15.8% in this zone. YS and TS are determined by the interplay of the strength-increasing mechanism of grain refinement and the strength-decreasing effect of the reduced martensite phase fraction. Both decrease continuously and reach a value of 928 MPa and 1269 MPa, respectively, in the very outer UCHAZ.

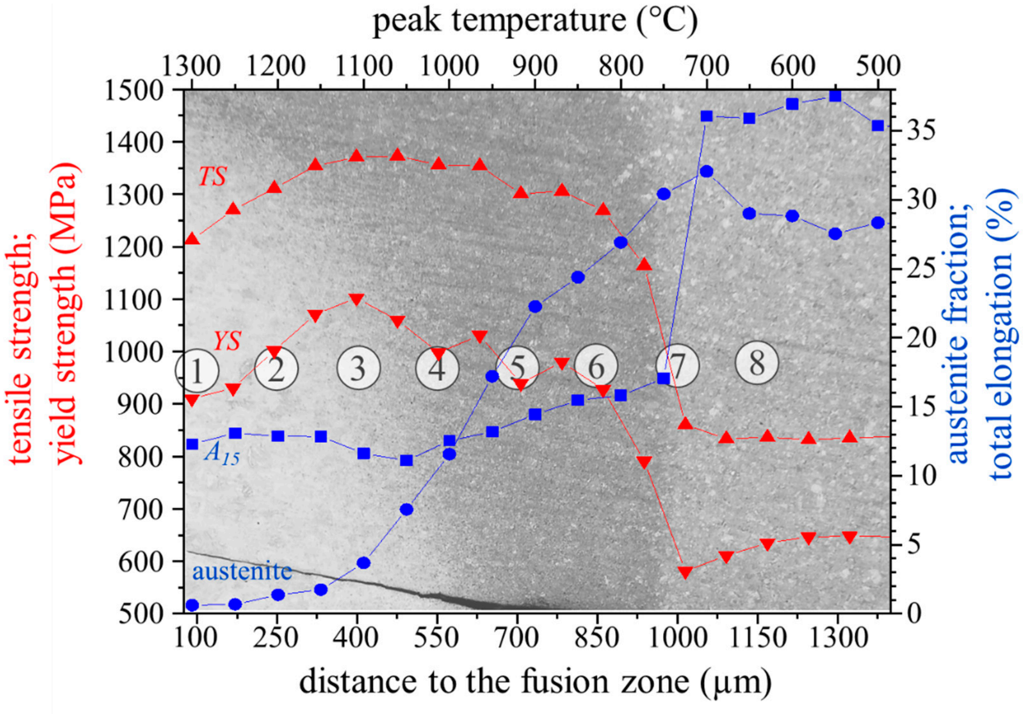

Figure 8. Austenite fraction (blue circles), tensile strength TS (upwards directed red triangle), yield strength YS (downwards directed red triangle) and total elongation A_{15} (blue squares) of the simulated HAZ. The microstructure of the HAZ after Nital etching is shown in the background. The numbered circles (1–8) represent the different positions of the HAZ where the microstructural characterization was done, as already described by Figure 3.

In the very narrow ICHAZ, which has a peak temperature of approximately 750 °C, the ferrite is only partly transformed into austenite during heating, and the final microstructure after quenching consequently consists of a mixture of austenite, ferrite and some martensite. This leads to a significant reduction in YS and TS to 791 MPa and 1164 MPa, respectively, with a simultaneous still slight increase of A_{15} to 17.1%. At a peak temperature of 700 °C, no martensite is present, and therefore both YS and TS decrease tremendously to 581 MPa and 861 MPa, respectively, and A_{15} increases sharply to 36.1%. With 32.1%, the austenite fraction reaches a maximum at this position and is noticeably higher compared to the BM. This may be because at this temperature, small amounts of ferrite are still transformed into austenite during heating. In this temperature regime, manganese enrichment may take place, which stabilizes the newly formed austenite. Therefore, no transformation into martensite during the final quenching takes place, and more retained austenite is stable. Lower temperatures do not influence the microstructure, and therefore the austenite fraction and the mechanical performance are equal to those of BM.

To sum up, the austenite retention and local mechanical properties of the HAZ strongly depend on the distance to the FZ, which illustrates the importance of investigating it with a small step size. It is shown that the outer FGHAZ with a high phase fraction of austenite does not display the highest strength, due to the grain refinement of the martensite as suggested in the literature [29], but the zone near position 3 does, where little austenite is present. With increasing distance to the FZ, the strength of the UCHAZ is determined by the interplay of the strength-increasing mechanism of grain refinement and the strength-decreasing effect of the reduced martensite phase fraction, while elongation continuously increases. Nevertheless, it must be mentioned that the mechanical properties of the physically simulated HAZ samples may not exactly represent the local mechanical properties of the HAZ, because, for example, differences in thermal history including holding time may affect the yield stress and plastic flow behavior.

4. Summary

In the present work, the microstructure and local mechanical properties of the HAZ of a resistance spot welded medium-Mn steel were investigated. The presented approach provides a way to obtain the temperature profile of the HAZ with a small step size and without relying on complex FE simulations and the most accurate data input data derived from time- and money-consuming investigations. For this purpose, the entire HAZ was characterized by means of SEM, EBSD and hardness measurements and compared to samples heat-treated on a thermal simulator. The temperature profile of the HAZ could be reproduced, and therefore the determination of the austenite phase fraction and the local mechanical properties of the HAZ was possible. Based on these findings, it can be concluded that the austenite in medium-Mn steels exhibits high thermal stability, which leads to highly position-dependent mechanical properties. It is shown that peak temperatures above 1200 °C lead to a uniform distribution of manganese, resulting in a predominantly martensitic microstructure with high strength and low total elongation after quenching. Below 1100 °C, the diffusion of manganese is inhibited, and a considerable fraction of austenite remains stable. The austenite fraction increases almost linearly with decreasing temperature, which leads to an increase in the total elongation and a slight decrease in the strength with a greater distance to the FZ. Temperatures below 700 °C exhibit hardly any effect on the microstructure and mechanical properties. The microstructural and mechanical characterization conducted in this work, combined with the simulated temperature profile, is intended to be the basis for future efforts to specifically manipulate the microstructure of the HAZ, for example, by means of a post-weld heat treatment, in order to potentially improve the mechanical performance of the entire weld.

Author Contributions: Conceptualization, M.S., R.S. and C.H.; methodology, M.S.; software, M.G.; validation, R.S., K.S. and C.H.; investigation, M.S.; resources, M.G., K.S. and R.S.; data curation, M.S.; writing—original draft preparation, M.S.; writing—review and editing, R.S., K.S. and C.H.; visualization, M.S.; supervision, R.S. and C.H.; project administration, M.S.; funding acquisition, R.S. All authors have read and agreed to the published version of the manuscript.

Funding: This research was funded by Austrian BMK (846933) in the framework of the program "Production of the future" and the "BMK Professorship for Industry".

Institutional Review Board Statement: Not applicable.

Informed Consent Statement: Not applicable.

Data Availability Statement: Not applicable.

Conflicts of Interest: The authors declare no conflict of interest.

References

1. Ebner, S.; Suppan, C.; Schnitzer, R.; Hofer, C. Microstructure and mechanical properties of a low C steel subjected to bainitic or quenching and partitioning heat treatments. *Mater. Sci. Eng. A* **2018**, *735*, 1–9. [CrossRef]
2. Hofer, C.; Leitner, H.; Winkelhofer, F.; Clemens, H.; Primig, S. Structural characterization of carbide-free bainite in a Fe–0.2C–1.5Si–2.5Mn steel. *Mater. Charact.* **2015**, *102*, 85–91. [CrossRef]
3. Fonstein, N. *Advanced High Strength Sheet Steels. Physical Metallurgy, Design, Processing and Properties*; Springer International Publishing: New York, NY, USA, 2015; ISBN 978-3-319-19164-5.
4. Matlock, D.K.; Speer, J.G. Third generation of AHSS: Microstructure design concepts. In *Microstructure and Texture in Steels*; Haldar, A., Suwas, S., Bhattacharjee, D., Eds.; Springer: London, UK, 2009; pp. 185–205, ISBN 978-1-84882-454-6.
5. Miller, R.L. Ultrafine-grained microstructures and mechanical properties of alloy steels. *Metall. Mater. Trans. B* **1972**, *3*, 905–912. [CrossRef]
6. Merwin, M.J. Low-carbon manganese TRIP steels. *Mater. Sci. Forum* **2007**, *539–543*, 4327–4332. [CrossRef]
7. Lee, S.; de Cooman, B.C. On the selection of the optimal intercritical annealing temperature for medium Mn TRIP steel. *Mater. Trans. A* **2013**, *44*, 5018–5024. [CrossRef]
8. Lee, Y.-K.; Han, J. Current opinion in medium manganese steel. *Mater. Sci. Technol.* **2015**, *31*, 843–856. [CrossRef]
9. Lee, S.; Lee, S.-J.; Santhosh Kumar, S.; Lee, K.; de Cooman, B.C. Localized deformation in multiphase, ultra-fine-grained 6 pct Mn transformation-induced plasticity steel. *Mater. Trans. A* **2011**, *42*, 3638–3651. [CrossRef]
10. Steineder, K.; Krizan, D.; Schneider, R.; Béal, C.; Sommitsch, C. On the microstructural characteristics influencing the yielding behavior of ultra-fine grained medium-Mn steels. *Acta Mater.* **2017**, *139*, 39–50. [CrossRef]
11. Kimchi, M.; Phillips, D.H. Resistance spot welding: Fundamentals and applications for the automotive industry. *Synth. Lect. Mech. Eng.* **2017**, *1*, i-115. [CrossRef]
12. Pouranvari, M.; Marashi, S.P.H. Critical review of automotive steels spot welding: Process, structure and properties. *Sci. Technol. Weld. Join.* **2013**, *18*, 361–403. [CrossRef]
13. Chabok, A.; van der Aa, E.; de Hosson, J.T.M.; Pei, Y.T. Mechanical behavior and failure mechanism of resistance spot welded DP1000 dual phase steel. *Mater. Des.* **2017**, *124*, 171–182. [CrossRef]
14. Eftekharimilani, P.; van der Aa, E.M.; Hermans, M.J.M.; Richardson, I.M. Microstructural characterisation of double pulse resistance spot welded advanced high strength steel. *Sci. Technol. Weld. Join.* **2017**, *22*, 545–554. [CrossRef]
15. Baltazar Hernandez, V.H.; Okita, Y.; Zhou, Y. Second pulse current in resistance spot welded TRIP steel-effects on the microstructure and mechanical behavior. *Impulse* **2012**, *91*, 278–285.
16. Stadler, M.; Schnitzer, R.; Gruber, M.; Hofer, C. Improving the mechanical performance of a resistance spot welded 1200 MPa TBF steel. *Int. J. Mater. Res* **2021**, *112*, 262–270. [CrossRef]
17. Sajjadi-Nikoo, S.; Pouranvari, M.; Abedi, A.; Ghaderi, A.A. In situ postweld heat treatment of transformation induced plasticity steel resistance spot welds. *Sci. Technol. Weld. Join* **2018**, *23*, 71–78. [CrossRef]
18. Liu, X.D.; Xu, Y.B.; Misra, R.D.K.; Peng, F.; Wang, Y.; Du, Y.B. Mechanical properties in double pulse resistance spot welding of Q&P 980 steel. *J. Mater. Process. Technol.* **2019**, *263*, 186–197. [CrossRef]
19. Stadler, M.; Schnitzer, R.; Gruber, M.; Steineder, K.; Hofer, C. Influence of the cooling time on the microstructural evolution and mechanical performance of a double pulse resistance spot welded medium-Mn steel. *Metals* **2021**, *11*, 270. [CrossRef]
20. Dancette, S.; Fabrègue, D.; Massardier, V.; Merlin, J.; Dupuy, T.; Bouzekri, M. Experimental and modeling investigation of the failure resistance of advanced high strength steels spot welds. *Eng. Fract. Mech.* **2011**, *78*, 2259–2272. [CrossRef]
21. Pouranvari, M. Susceptibility to interfacial failure mode in similar and dissimilar resistance spot welds of DP600 dual phase steel and low carbon steel during cross-tension and tensile-shear loading conditions. *Mater. Sci. Eng. A* **2012**, *546*, 129–138. [CrossRef]
22. Tamizi, M.; Pouranvari, M.; Movahedi, M. The role of HAZ softening on cross-tension mechanical performance of martensitic advanced high strength steel resistance spot welds. *Metall. Mater. Trans. A* **2021**, *88*, 1. [CrossRef]

23. Pouranvari, M.; Sobhani, S.; Goodarzi, F. Resistance spot welding of MS1200 martensitic advanced high strength steel: Microstructure-properties relationship. *J. Manuf. Process.* **2018**, *31*, 867–874. [CrossRef]
24. Rezayat, H.; Ghassemi-Armaki, H.; Bhat, S.P.; Sriram, S.; Babu, S.S. Constitutive properties and plastic instabilities in the heat-affected zones of advanced high-strength steel spot welds. *J. Mater. Sci.* **2019**, *54*, 5825–5843. [CrossRef]
25. Stadler, M.; Gruber, M.; Schnitzer, R.; Hofer, C. Microstructural characterization of a double pulse resistance spot welded 1200 MPa TBF steel. *Weld World* **2020**, *64*, 335–343. [CrossRef]
26. Dancette, S.; Massardier-Jourdan, V.; Fabrègue, D.; Merlin, J.; Dupuy, T.; Bouzekri, M. HAZ microstructures and local mechanical properties of high strength steels resistance spot welds. *ISIJ Int.* **2011**, *51*, 99–107. [CrossRef]
27. Pouranvari, M. Effect of resistance spot welding parameters on the HAZ softening of DP980 ferrite-martensite dual phase steel welds. *World Appl. Sci. J.* **2011**, *15*, 1454–1458.
28. Jia, Q.; Liu, L.; Guo, W.; Peng, Y.; Zou, G.; Tian, Z.; Zhou, Y. Microstructure and tensile-shear properties of resistance spot-welded medium Mn steel. *Metals* **2018**, *8*, 48. [CrossRef]
29. Park, G.; Kim, K.; Uhm, S.; Lee, C. A comparison of cross-tension properties and fracture behavior between similar and dissimilar resistance spot-weldments in medium-Mn TRIP steel. *Mater. Sci. Eng. A* **2019**, *752*, 206–216. [CrossRef]
30. Park, G.; Kim, K.; Uhm, S.; Lee, C. Remarkable improvement in resistance spot weldability of medium-Mn TRIP steel by paint-baking heat treatment. *Mater. Sci. Eng. A* **2019**, *766*, 138401. [CrossRef]
31. Park, G.; Uhm, S.; Lee, C. Effects of in-situ post-weld heat treatment on the microstructure and mechanical properties of the coarse-grained heat-affected zone in a resistance spot weld in medium Mn TRIP steel. *Mater. Sci. Eng. A* **2020**, *788*, 139477. [CrossRef]
32. STAHL-EISEN-Prüfblätter (SEP) des Stahlinstituts VDEh. *SEP 1220-2: Testing and Documentation Guideline for the Joinability of Thin Sheet of Steel-Part 2: Resistance Spot Welding*; Verlag Stahleisen GmbH: Düsseldorf, Germany.
33. *DIN EN ISO 6892-1:2020-06, Metallische Werkstoffe—Zugversuch—Teil 1: Prüfverfahren bei Raumtemperatur (ISO_6892-1:2019)*; Beuth Verlag GmbH: Berlin, Germany.
34. Goldstein, J.I.; Newbury, D.E.; Michael, J.R.; Ritchie, N.W.M.; Scott, J.h.J.; Joy, D.C. *Scanning Electron Microscopy and X-ray Microanalysis*, 4th ed.; Springer: New York, NY, USA, 2017; ISBN 978-1-4939-6674-5.
35. Hofer, C.; Bliznuk, V.; Verdiere, A.; Petrov, R.; Winkelhofer, F.; Clemens, H.; Primig, S. Correlative microscopy of a carbide-free bainitic steel. *Micron* **2016**, *81*, 1–7. [CrossRef] [PubMed]
36. Hofer, C.; Bliznuk, V.; Verdiere, A.; Petrov, R.; Winkelhofer, F.; Clemens, H.; Primig, S. High-resolution characterization of the martensite-austenite constituent in a carbide-free bainitic steel. *Mater. Charact.* **2018**, *144*, 182–190. [CrossRef]